





**RUPTURE STATUS INVESTIGATION OF PATIENT SPECIFIC CEREBRAL  
ANEURYSMS BY ANALYSING HEMODYNAMIC FACTORS  
USING COMPUTATIONAL FLUID DYNAMICS**



**M.Sc. THESIS**

**G. Merve NARİNSES**

**Department of Computational Science and Engineering**

**Computational Science and Engineering Programme**

**DECEMBER 2018**



**RUPTURE STATUS INVESTIGATION OF PATIENT SPECIFIC CEREBRAL  
ANEURYSMS BY ANALYSING HEMODYNAMIC FACTORS  
USING COMPUTATIONAL FLUID DYNAMICS**

**M.Sc. THESIS**

**G. Merve NARİNSES  
(702141023)**

**Department of Computational Science and Engineering**

**Computational Science and Engineering Programme**

**Thesis Advisor: Prof. Dr. M. Serdar ÇELEBİ**

**DECEMBER 2018**



**İSTANBUL TEKNİK ÜNİVERSİTESİ ★ BİLİŞİM ENSTİTÜSÜ**

**HESAPLAMALI AKIŞKANLAR DİNAMİĞİ KULLANARAK  
HEMODİNAMİK FAKTÖRLERİN ANALİZİ İLE HASTAYA ÖZGÜ BEYİN  
ANEVRİZMALARININ YIRTIлма DURUMU İNCELEMESİ**

**YÜKSEK LİSANS TEZİ**

**G. Merve NARİNSE**  
**(702141023)**

**Hesaplamalı Bilim ve Mühendislik Anabilim Dalı**

**Hesaplamalı Bilim ve Mühendislik Programı**

**Tez Danışmanı: Prof. Dr. M. Serdar ÇELEBİ**

**ARALIK 2018**





G. Merve NARİNSE, a M.Sc. student of ITU Informatics Institute 702141023 successfully defended the thesis entitled “RUPTURE STATUS INVESTIGATION OF PATIENT SPECIFIC CEREBRAL ANEURYSMS BY ANALYSING HEMODYNAMIC FACTORS USING COMPUTATIONAL FLUID DYNAMICS”, which she prepared after fulfilling the requirements specified in the associated legislations, before the jury whose signatures are below.

**Thesis Advisor :**     **Prof. Dr. M. Serdar ÇELEBİ** .....  
Istanbul Technical University

**Jury Members :**     **Prof. Dr. M. Serdar ÇELEBİ** .....  
Istanbul Technical University

**Prof. Dr. Mine ÇAĞLAR** .....  
Koç University

**Assoc. Prof. Dr. Ufuk Utku TURUNÇOĞLU** .....  
Istanbul Technical University

**Date of Submission :**   **16 November 2018**

**Date of Defense :**     **14 December 2018**





*To my family,*



## FOREWORD

First of all, I would like to present my thankfulness to my thesis advisor, Prof. Dr. M. Serdar Çelebi for his supports and guidance through all this process and M.Sc. study.

I would like to thank Prof. Dr. Juan R. Cebal who is the most-known researcher regarding to the CFD-based cerebral aneurysm studies and inspires me with his precious researches. I would like to present my eternal gratefulness to him for his advices for me.

I am very grateful to Prof. Dr. Reha Artan for introducing me partial differential equations with his profound knowledge, supports and great patience. As a biologist, I wouldn't achieve to learn PDEs without him.

Also, I would like to present my eternal thankfulness to Yağmur Gülkanat, for her endless supports, advices, helps and precious time.

I am very thankful to Vincent, who has always been like a father to me, for his supports, helps, patiences, motivations, from the very beginning when I first came to Belgium and still, I don't know how to explain my great thankfulness to him. He has always been a precious mentor through my neuroscience studies.

And lastly, I want to thank my mom, Bircan and my sister, Özge since they've always believed in me and showed great support and patience for me.

December 2018

G. Merve NARİNSES  
(M.Sc. Student)



## TABLE OF CONTENTS

	<u>Page</u>
<b>FOREWORD</b> .....	<b>ix</b>
<b>TABLE OF CONTENTS</b> .....	<b>xi</b>
<b>ABBREVIATIONS</b> .....	<b>xiii</b>
<b>LIST OF TABLES</b> .....	<b>xv</b>
<b>LIST OF FIGURES</b> .....	<b>xvii</b>
<b>SUMMARY</b> .....	<b>xxiii</b>
<b>ÖZET</b> .....	<b>xxvii</b>
<b>1. INTRODUCTION</b> .....	<b>1</b>
1.1 Literature Review .....	4
<b>2. BIOLOGICAL CHARACTERISTICS</b> .....	<b>15</b>
2.1 Purpose .....	15
2.2 The Characteristics of the Blood and Vessels.....	15
2.3 Cerebral Aneurysms .....	19
<b>3. MATHEMATICAL MODELING OF BLOOD FLOW</b> .....	<b>23</b>
3.1 Purpose .....	23
3.2 The Governing Equations .....	23
3.3 Rheology of Blood .....	25
3.4 Blood as a Turbulent Flow.....	29
3.5 Numerical Discretization.....	32
<b>4. MATERIALS AND METHODS</b> .....	<b>33</b>
4.1 Cerebral Aneurysm Data .....	33
4.2 Cerebral Aneurysm Data Preparation for CFD Processing .....	34
4.3 Numerical Methods for CFD Processing .....	37
4.4 Hemodynamic Indices for Post Processing Analyzes .....	39
4.4.1 Wall shear stress .....	40
4.4.2 Oscillatory shear index .....	40
4.4.3 Time averaged wall shear stress .....	41
4.4.4 Spatial wall shear stress gradient.....	42
4.4.5 Time averaged spatial wall shear stress gradient.....	42
<b>5. NUMERICAL RESULTS</b> .....	<b>43</b>
5.1 Grid Convergence Index Method and Results .....	43
5.2 Patient-Specific Model Case Setups and Boundary Conditions.....	49
5.3 Numerical Simulation Results for U-ICA .....	52
5.4 Numerical Simulation Results for R-ICA .....	72
<b>6. DISCUSSIONS AND CONCLUSIONS</b> .....	<b>93</b>
<b>REFERENCES</b> .....	<b>97</b>





## ABBREVIATIONS

<b>3D</b>	: Three Dimensional
<b>3D-CTA</b>	: Three Dimensional Computed Tomographic Angiography
<b>3DRA</b>	: Three Dimensional Rotational Angiography
<b>ACA</b>	: Anterior Cerebral Artery
<b>ACoA</b>	: Anterior Communicating Artery
<b>AICA</b>	: Anterior Inferior Cerebellar Artery
<b>Amazon</b>	: Amazon Elastic Compute Cloud
<b>EC2</b>	
<b>AR</b>	: Aspect Ratio
<b>AWS</b>	: Amazon Web Services
<b>BA</b>	: Basilar Artery
<b>bpm</b>	: Beats Per Minute
<b>CFD</b>	: Computational Fluid Dynamics
<b>CoW</b>	: Circle of Willis
<b>CTA</b>	: Computed Tomography Angiography
<b>CY</b>	: Carreau-Yasuda
<b>DICOM</b>	: Digital Imaging and Communications in Medicine
<b>DNS</b>	: Direct Numerical Simulation
<b>EL</b>	: Energy Loss
<b>FDM</b>	: Finite Difference Method
<b>FEM</b>	: Finite Element Method
<b>FSI</b>	: Fluid-Structure Interaction
<b>FVM</b>	: Finite Volume Method
<b>GCI</b>	: Grid Convergence Index
<b>ICA</b>	: Internal Carotid Artery
<b>ICI</b>	: Inflow Concentration Index
<b>KER</b>	: Kinetic Energy Ratio
<b>LES</b>	: Large Eddy Simulation
<b>MCA</b>	: Middle Cerebral Artery
<b>MIP</b>	: Maximum Intensity Projections
<b>MRI</b>	: Magnetic Resonance Imaging
<b>OSI</b>	: Oscillatory Shear Index
<b>OVI</b>	: Oscillatory Velocity Index
<b>PCA</b>	: Posterior Cerebral Artery
<b>PCoA</b>	: Posterior Communicating Artery
<b>PDEs</b>	: Partial Differential Equations
<b>PICA</b>	: Posterior Inferior Cerebellar Artery
<b>PISO</b>	: Pressure-Implicit with Splitting of Operators
<b>RANS</b>	: Reynolds Averaged Navier Stokes

<b>RBCs</b>	: Red Blood Cells
<b>R-ICA</b>	: Ruptured Internal Carotid Artery
<b>RRT</b>	: Relative Residence Time
<b>SAH</b>	: Subarachnoid Hemorrhage
<b>SCA</b>	: Superior Cerebellar Artery
<b>SCI</b>	: Shear Concentration Index
<b>SGS</b>	: Subgrid-Scale
<b>SR</b>	: Size Ratio
<b>STL</b>	: Stereolithography
<b>SWSSG</b>	: Spatial Wall Shear Stress Gradient
<b>TAWSS</b>	: Time Averaged Wall Shear Stress
<b>U-ICA</b>	: Unruptured Internal Carotid Artery
<b>VA</b>	: Vertebral Artery
<b>VMTK</b>	: The Vascular Modeling Toolkit
<b>WBCs</b>	: White Blood Cells
<b>WSS</b>	: Wall Shear Stress



## LIST OF TABLES

	<u>Page</u>
<b>Table 3.1</b> : Some non-Newtonian viscosity models for blood flow. The parameters are the time constant $\lambda$ , power constant $n$ , parameter used to fit experimental data $a$ , model constant $k$ and yield stress $\tau_0$ .	28
<b>Table 5.1</b> : Different maximum velocity values $f_i$ corresponding to different number of elements $N_i$ . The values are obtained from nearby outflow area.....	44
<b>Table 5.2</b> : GCI method parameters and corresponding values regarding to the nearby outflow area.....	46
<b>Table 5.3</b> : Different maximum velocity values $f_i$ corresponding to different number of elements $N_i$ . The values are obtained from nearby before aneurysm neck area.....	47
<b>Table 5.4</b> : GCI method parameters and corresponding values regarding to the area of before aneurysm neck. ....	48
<b>Table 5.5</b> : Parameters and corresponding values of Carreau-Yasuda viscosity model [87].....	50



## LIST OF FIGURES

	<u>Page</u>
<b>Figure 1.1</b> : Intracranial aneurysm risk factors and their relations [25].	2
<b>Figure 1.2</b> : The role of high and low WSS in aneurysm initiation, growth and rupture [19].	3
<b>Figure 1.3</b> : The flow velocity in the femoral artery of the dog during one cardiac cycle [45].	5
<b>Figure 1.4</b> : Velocity field, WSS distribution and streamline visualizations of two unruptured aneurysms, the arrows indicate the sites of maximum WSS, Shojima et al. [54].	6
<b>Figure 1.5</b> : Hemodynamic effects on the aneurysms by Cebal et al. [59].	8
<b>Figure 1.6</b> : Figure shows two independent hypotheses, (A) indicates hemodynamic-biologic pathways that cause intracranial aneurysm growth and rupture and (B) shows the relationship between them and intracranial aneurysm phenotypes proposed by Meng et al. [19].	9
<b>Figure 1.7</b> : The figure provided by Cebal et al. [36]: "Maximum intensity projections (MIP) of intracranial aneurysms from CTA and 3DRA."	10
<b>Figure 1.8</b> : In the figure (a) shows the velocity magnitude in the centre of the aneurysm; and (b) shows the WSS in one point of the aneurysm dome by Valencia et al. [68].	12
<b>Figure 1.9</b> : Energy loss (EL) calculation method by Qian et al. [31].	13
<b>Figure 2.1</b> : RBCs flowing within glass tubes for three different diameters [77]. This figure is a modification of [78].	17
<b>Figure 2.2</b> : Cellular elements of the blood (2006 Encyclopaedia Britannica, Inc.).	18
<b>Figure 2.3</b> : Layers of artery, vein and capillary [81].	19
<b>Figure 2.4</b> : Aneurysm types in terms of their shapes. Saccular aneurysm on the top (a) and fusiform aneurysm on the bottom (b) by Campo-Deano et al. [67].	20
<b>Figure 2.5</b> : (A) shows side-wall aneurysm with $P_1$ afferent vessel and $P_2$ efferent vessel while (B) shows terminal aneurysm with $P_1$ afferent vessel and $P_2, P_3$ efferent vessels by Munarriz et. al [21].	21

<b>Figure 2.6</b> :	The figure shows both aneurysm and atherosclerosis in the CoW. Locations in CoW could be summarized as follows: ACA (Anterior Cerebral Artery), ACoA (Anterior Communicating Artery), AICA (Anterior Inferior Cerebellar Artery), BA (Basilar Artery), ICA (Internal Carotid Artery), MCA (Middle Cerebral Artery), PCA (Posterior Cerebral Artery), PCoA (Posterior Communicating Artery), PICA (Posterior Inferior Cerebellar Artery), SCA (Superior Cerebellar Artery), VA (Vertebral Artery). Darker color in (A) indicates saccular aneurysms, while indicates atherosclerosis in (B) by Nixon et al. [83].	21
<b>Figure 2.7</b> :	The arteries and the corresponding aneurysms with their prevalences in the CoW by Brisman et al. [2].	22
<b>Figure 3.1</b> :	Rheology diagram of the flow behaviors [84].	26
<b>Figure 3.2</b> :	The turbulence regime sketches by Leonardo da Vinci (Nature).	29
<b>Figure 3.3</b> :	From laminar to turbulent flow [94].	30
<b>Figure 3.4</b> :	CFD methodology flowchart [94].	32
<b>Figure 4.1</b> :	Original geometry image represents $U - ICA$ model from the AneuriskWeb repository.	35
<b>Figure 4.2</b> :	Original geometry image represents $R - ICA$ model from the AneuriskWeb repository.	35
<b>Figure 4.3</b> :	The STL geometry images after clipping, adding flow extensions, closing the gaps and scaling applied to the original STL data.	36
<b>Figure 4.4</b> :	Mesh generations have been performed using Netgen [100].	38
<b>Figure 5.1</b> :	The cross section, nearby the outlet boundary (A). The line onto the cross section indicates where maximum velocity has been calculated along (B).	45
<b>Figure 5.2</b> :	Womersley Inlet profile used in GCI analysis.	45
<b>Figure 5.3</b> :	Velocity magnitude values on the line of the cross section nearby the outflow area for the 5 different grids in terms of cell numbers. Axis x indicates the length of the line and axis y indicates velocity magnitude.	45
<b>Figure 5.4</b> :	The arrow indicates the cross section, nearby before aneurysm neck area (A). The line onto the cross section indicates where maximum velocity has been calculated along (B).	47
<b>Figure 5.5</b> :	Velocity magnitude values on the line of the cross section nearby before aneurysm neck for the 3 different grids in terms of cell numbers. Axis x indicates the length of the line and axis y indicates velocity magnitude.	48
<b>Figure 5.6</b> :	Womersley velocity profile during five cardiac cycles. One cardiac cycle takes 0,743 seconds to complete and five cardiac cycles last 3,715 seconds.	50
<b>Figure 5.7</b> :	Patient-specific cerebral aneurysm model cases.	51
<b>Figure 5.8</b> :	WSS behavior has been observed during last cardiac cycle within $U - ICA$ geometry for the selected region before aneurysm neck which is indicated with white circle. CY indicates Carreau-Yasuda viscosity model and LES indicates Large Eddy Simulation.	53

<b>Figure 5.9 :</b> Pressure behavior has been observed during last cardiac cycle within $U - ICA$ geometry for the selected region before aneurysm neck which is indicated with white circle. CY indicates Carreau-Yasuda viscosity model and LES indicates Large Eddy Simulation. ....	54
<b>Figure 5.10:</b> Velocity behavior has been observed during last cardiac cycle within $U - ICA$ geometry for the whole slice before aneurysm neck. CY indicates shear-thinning Carreau-Yasuda viscosity model and LES indicates Large Eddy Simulation. ....	55
<b>Figure 5.11:</b> WSS behavior has been observed during last cardiac cycle within $U - ICA$ geometry for the region-1 on the aneurysm sac area which is indicated with white circle. CY indicates Carreau-Yasuda viscosity model and LES indicates Large Eddy Simulation. ....	56
<b>Figure 5.12:</b> WSS behavior has been observed during last cardiac cycle within $U - ICA$ geometry for the region-2 on the aneurysm sac area which is indicated with white circle. CY indicates Carreau-Yasuda viscosity model and LES indicates Large Eddy Simulation. ....	57
<b>Figure 5.13:</b> Pressure behavior has been observed during last cardiac cycle within $U - ICA$ geometry for the region-1 on the aneurysm sac area which is indicated with white circle. CY indicates Carreau-Yasuda viscosity model and LES indicates Large Eddy Simulation. ....	58
<b>Figure 5.14:</b> Pressure behavior has been observed during last cardiac cycle within $U - ICA$ geometry for the region-2 on the aneurysm sac area which is indicated with white circle. CY indicates Carreau-Yasuda viscosity model and LES indicates Large Eddy Simulation. ....	59
<b>Figure 5.15:</b> Velocity behavior has been observed during last cardiac cycle within $U - ICA$ geometry for the slice-1 on the aneurysm sac area. CY indicates shear-thinning Carreau-Yasuda viscosity model and LES indicates Large Eddy Simulation. ....	60
<b>Figure 5.16:</b> Velocity behavior has been observed during last cardiac cycle within $U - ICA$ geometry for the slice-2 on the aneurysm sac area. CY indicates shear-thinning Carreau-Yasuda viscosity model and LES indicates Large Eddy Simulation. ....	61
<b>Figure 5.17:</b> WSS behavior has been observed during last cardiac cycle within $U - ICA$ geometry for the selected region after aneurysm neck which is indicated with white circle. CY indicates Carreau-Yasuda viscosity model and LES indicates Large Eddy Simulation. ....	62
<b>Figure 5.18:</b> Pressure behavior has been observed during last cardiac cycle within $U - ICA$ geometry for the selected region after aneurysm neck which is indicated with white circle. CY indicates Carreau-Yasuda viscosity model and LES indicates Large Eddy Simulation. ....	63
<b>Figure 5.19:</b> Velocity behavior has been observed during last cardiac cycle within $U - ICA$ geometry for the whole slice after aneurysm neck. CY indicates shear-thinning Carreau-Yasuda viscosity model and LES indicates Large Eddy Simulation. ....	64

**Figure 5.20:** First row indicates velocity (m/s) streamlines for non-Newtonian Carreau-Yasuda (CY) model while second row indicates velocity streamlines for non-Newtonian Carreau-Yasuda (CY) with LES turbulence effects model for the last cardiac cycle within  $U - ICA$  geometry. The figures have been visualized at peak systole..... 65

**Figure 5.21:** First row indicates velocity (m/s) vector field for non-Newtonian Carreau-Yasuda (CY) model while second row indicates velocity vector field for non-Newtonian CY with LES turbulence effects model for the last cardiac cycle within  $U - ICA$  geometry. The figures have been visualized at peak systole..... 66

**Figure 5.22:** From left to right, WSS, TAWSS and OSI visualizations for the last cardiac cycle within  $U - ICA$  model. (A) indicates non-Newtonian shear-thinning Carreau-Yasuda flow model (CY) while (B) indicates CY with LES turbulence effects. WSS has been visualized at peak systolic time, TAWSS has been visualized as time-averaged. .... 67

**Figure 5.23:** SWSSG and TASWSSG visualizations for the last cardiac cycle within  $U - ICA$  model. (A) indicates non-Newtonian shear-thinning Carreau-Yasuda flow model (CY) while (B) indicates CY with LES turbulence effects. SWSSG has been visualized at peak systolic time, TASWSSG has been visualized as time-averaged. .... 69

**Figure 5.24:** The figure represents the values of hemodynamic factors and WSS visualizations for whole geometry and aneurysm sac area within  $U - ICA$  model. CY indicates Carreau-Yasuda and LES indicates Large Eddy Simulation. WSS has been visualized at peak systole..... 70

**Figure 5.25:** The white circles indicate where WSS behaviors have been observed before aneurysm neck area within  $R - ICA$  model (top). WSS plot indicates the comparison of CY model and CY with LES blood flow model for the indicated region (bottom). .... 73

**Figure 5.26:** Pressure and WSS have been observed for the same regions. White circles indicate where pressure behaviors have been observed (top). The plot indicates pressure values during the last cardiac cycle for the area before aneurysm neck within  $R - ICA$  for shear-thinning CY model and CY with LES turbulence blood flow model (bottom). .... 74

**Figure 5.27:** Velocity profile has been observed on the selected region (m/s) within  $R - ICA$  model during last cardiac cycle. One slice has been taken before aneurysm neck (top) and the plot indicates the velocity behavior for the whole slice within the  $R - ICA$  geometry for CY and CY with LES blood flow model (bottom). .... 75

**Figure 5.28:** The white circle indicates where WSS behavior has been observed on the aneurysm sac area for region-1 within  $R - ICA$  model (top). WSS plot indicates the comparison of CY model and CY with LES blood flow model for the indicated region (bottom). ... 76



<b>Figure 5.29:</b> The white circles indicate where WSS behaviors have been observed on the aneurysm sac area for region-2 within $R - ICA$ model (top). WSS plot indicates the comparison of CY model and CY with LES turbulence blood flow model for the indicated region (bottom).....	77
<b>Figure 5.30:</b> Pressure and WSS have been observed for the same regions. White circles indicate where pressure behaviors have been observed (top). The plot indicates pressure values during the last cardiac cycle in the aneurysm sac area for region-1 within $R - ICA$ geometry for shear-thinning CY model and CY with LES turbulence blood flow model (bottom).....	78
<b>Figure 5.31:</b> Pressure and WSS have been observed for the same regions. White circles indicate where pressure behaviors have been observed (top). The plot indicates pressure values during the last cardiac cycle in the aneurysm sac area for region-2 within $R - ICA$ geometry for shear-thinning CY model and CY with LES turbulence blood flow model (bottom).....	80
<b>Figure 5.32:</b> Velocity profile has been observed on the selected zone within $R - ICA$ model during last cardiac cycle. One slice has been taken from aneurysm sac area as slice-1 (top) and the plot indicates the velocity behavior for the whole slice within the $R - ICA$ geometry for CY and CY with LES blood flow model (bottom).....	81
<b>Figure 5.33:</b> Velocity profile has been observed on the selected zone within $R - ICA$ model during last cardiac cycle. One slice has been taken from aneurysm sac area as slice-2 (top) and the plot indicates the velocity behavior for the whole slice within the $R - ICA$ geometry for CY and CY with LES blood flow model (bottom).....	82
<b>Figure 5.34:</b> WSS behavior has been observed on the selected zone after aneurysm neck within $R - ICA$ model during last cardiac cycle (top) and the plot indicates the WSS behavior for the selected area within the $R - ICA$ geometry for CY and CY with LES blood flow model (bottom).....	83
<b>Figure 5.35:</b> Pressure behavior has been observed on the selected zone after aneurysm neck within $R - ICA$ model during last cardiac cycle (top) and the plot indicates the pressure behavior for the selected area within the $R - ICA$ geometry for CY and CY with LES blood flow model (bottom). .....	84
<b>Figure 5.36:</b> Velocity profile has been observed on the selected zone within $R - ICA$ model during last cardiac cycle. One slice has been taken after aneurysm sac area (top) and the plot indicates the velocity behavior for the whole slice within the $R - ICA$ geometry for CY and CY with LES blood flow model (bottom).....	85
<b>Figure 5.37:</b> Velocity (m/s) streamlines at peak systolic time of the last cardiac cycle within $R - ICA$ model. First row, CY indicates shear-thinning Carreau-Yasuda model while second row, CY + LES indicates shear-thinning CY with LES turbulence flow model...	86

**Figure 5.38:** Velocity vector field at peak systole of the last cardiac cycle within *R – ICA* model. First row, CY indicates shear-thinning Carreau-Yasuda model while second row, CY + LES indicates Carreau-Yasuda with LES turbulence flow model..... 87

**Figure 5.39:** From left to right, WSS, TAWSS and OSI visualizations for the last cardiac cycle within *R – ICA* model. WSS has been visualized at peak systolic time, TAWSS has been visualized as time-averaged. First row (A) indicates shear-thinning CY model while second row (B) indicates shear-thinning CY with LES turbulence flow model..... 88

**Figure 5.40:** SWSSG and TASWSSG visualizations within *R – ICA* model. SWSSG has been visualized at peak systole. First row, (A) indicates shear-thinning Carreau-Yasuda (CY) model while second row, (B) indicates shear-thinning Carreau-Yasuda (CY) with LES turbulence flow model. .... 89

**Figure 5.41:** The figure represents the values of hemodynamic factors and WSS visualizations for whole geometry and aneurysm sac area within *R – ICA* model. CY indicates Carreau-Yasuda and LES indicates Large Eddy Simulation. WSS has been visualized at peak systole..... 90

# **RUPTURE STATUS INVESTIGATION OF PATIENT SPECIFIC CEREBRAL ANEURYSMS BY ANALYSING HEMODYNAMIC FACTORS USING COMPUTATIONAL FLUID DYNAMICS**

## **SUMMARY**

Cerebral aneurysms are rather common considering the worldwide scale of population and associated with high morbidity and mortality rate. In order to prevent disability problems and deaths caused by cerebral aneurysms, the researchers from both medical side and engineering side have been performing intensive studies. Although the intensive researches, cerebral aneurysms, particularly hemodynamic effects on cerebral aneurysms are not quite well understood. Hence, as long as the researches proceed, the studies in terms of aneurysm status might enlighten the mystery of hemodynamic effects on the cerebral aneurysms.

Essentially, the aneurysms are pathologic and abnormal structures of the blood vessel walls. Cerebral aneurysms arise from the weakness of the cerebral artery caused by various factors such as genetics and hypertension. These structures are abnormal dilations of the arterial wall that mostly localized in the Circle of Willis (CoW). There are three phases for the cerebral aneurysms: formation, growth and eventually rupture. The rupture of the cerebral aneurysm might lead to serious disability problems for the patient or even worse, might be end up with the death of the patient. When the rupture is occurred within the cerebral aneurysm, it might lead to the bleeding into the subarachnoid space in the brain. This phenomenon is called subarachnoid hemorrhage (SAH) and SAH is occurred by cerebral aneurysms with a remarkably rate of 85%. As a consequence, it is significantly crucial to investigate rupture status of the cerebral aneurysms in order to predict the rupture risk.

For a long time, over the centuries, circulatory system had been examined in behalf of discovering the organisms. Blood vessel remodeling with the flow conditions had been studied a long time ago in 1800s by Virchow. Thenceforward, the blood vessels and blood flow studies have been extensively performed in order to examine circulatory system. Before the computational-based investigations in the sense of the cerebral aneurysms and blood flow in arteries, animal-based experiments had been performed considerably to explore this secret world of the blood flow complexity in circulatory and cardiovascular system. The development of technology gives computer-based studies an opportunity in order to examine blood flow simulations that is unfeasible to perform by means of in-vivo methods. Particularly, with the increasing techniques and technologies with regard to imaging, it has become possible to perform computational fluid dynamics (CFD) within patient-specific cerebral aneurysms instead of performing simulations within the artificial straight pipe geometries that are not realistic and reliable.

It has been demonstrated that the examination based on CFD and hemodynamic factors play a significant role in order to investigate cerebral aneurysm steps which

are initiation, growth and rupture, respectively. However, there are still contradictory studies with regards to the rupture risk examinations of the cerebral aneurysms under hemodynamic factors and these factors are not completely understood. For this purpose, within this study, the rupture status of the patient-specific cerebral aneurysms have been examined with regards to hemodynamic factors by means of CFD. The CFD simulations have been performed by means of an open source CFD software based on C++ which is OpenFOAM (Open-source Field Operation And Manipulation).

CFD techniques have been used extensively by researchers and become inspiring methods in terms of analyzing the effects of the hemodynamic factors on the image-based patient-specific cerebral aneurysms. However, the simulation results might be misleading if the grid resolution is not properly fit in with the abnormal and complex aneurysm geometry. In order to overcome this issue, there is a need for estimating the discretization errors in CFD studies. The error analysis studies have been performed extensively in CFD researches for decades, therefore, also within this thesis, grid convergence index (GCI) method based on generalized Richardson Extrapolation has been performed in order to estimate the discretization errors.

Due to its non-Newtonian shear-thinning viscoelastic nature and wave-like Womersley velocity profile, mathematical modeling of blood flow is a challenging phenomenon, more particularly in complex and abnormal patient-specific vessels such as cerebral aneurysms. Moreover, the aneurysm sac region is an abnormal area and within this area blood flow tends to exhibit from transient to turbulence nature with the increasing numbers of Reynolds. Therefore, within this study, under the Navier-Stokes equations, the blood has been modeled as unsteady, incompressible, pulsatile flow with its non-Newtonian shear-thinning characteristic by taking the advantage of Carreau-Yasuda viscosity model. Regarding to the turbulence nature within the aneurysm sac, it has been examined turbulence effects by means of dynamic k-equation for large eddy simulations (LES). Regarding to the patient-specific cerebral aneurysm geometries, due to the lack of the vascular wall information in the sense of thickness and elasticity in the *Aneurisk dataset repository*, the vascular walls have been modeled as rigid with no-slip boundary conditions. All the simulations have been performed with the pisoFoam solver based on PISO (Pressure-Implicit with Splitting of Operators) algorithm under finite volume method (FVM) by using OpenFOAM.

The original patient-specific cerebral aneurysm data have been clipped in order to examine the region of interests, added flow extensions in order to have proper inflow and outflow boundaries by using the Vascular Modeling Toolkit (VMTK), an open source software. In order to perform CFD simulations, triangular surface meshes and tetrahedral volume meshes have been generated by using ICEM CFD 19.2 (ANSYS, Inc., Canonsburg, PA, USA). The simulation results obtained have been visualized in terms of hemodynamic factors such as WSS, oscillatory shear index (OSI), time-averaged WSS (TAWSS), spatial WSS gradient (SWSSG) and time-averaged SWSSG (TASWSSG) by using ParaView, an open source visualization software. This thesis has been written by using L<sup>A</sup>T<sub>E</sub>X.

Within this study, the rupture status of one ruptured which belongs to a female patient aged 26 and one unruptured which belongs to a female patient aged 48, patient-specific cerebral aneurysm data from the *Aneurisk dataset repository* have been investigated in terms of hemodynamic factors by using CFD in order to observe the similarities and differences of rupture status with non-Newtonian shear-thinning characteristic of

blood flow by implementing Carreau-Yasuda viscosity model with the pulsatile nature of blood flow. Moreover, it has been investigated turbulent flow nature of blood with dynamic k-equation for LES turbulence model in order to observe the non-Newtonian characteristic with turbulence effects, particularly in the aneurysm sac region.

Within both ruptured and unruptured cerebral aneurysm data, the streamlines exhibit smoothly in the inlet area and tend to exhibit transient behavior within the curvature regions. The streamlines behave chaotic and exhibit turbulent nature when the flow arrives in the aneurysm sac area.

The simulation results demonstrated that within the patient specific cerebral aneurysm data, particularly in the aneurysm sac, with the increasing Reynolds numbers especially at the peak systole, the mild turbulence effects have been observed. The WSS vectors exhibit different directions under the turbulence effects with the turbulence blood flow model, and as a consequence, OSI values increase.

From the simulations results, considering the WSS values for both non-Newtonian Carreau-Yasuda (CY) and non-Newtonian CY with LES turbulence models, lower WSS has been observed for aneurysm sac region than parent vessel within ruptured cerebral aneurysm  $R - ICA$  while higher WSS has been observed for aneurysm sac region than parent vessel within unruptured cerebral aneurysm  $U - ICA$ . These results have similarities with other studies in the literature (e.g. Shojima et al.).

In opposition to the literature, within this study, OSI values have been observed higher for the unruptured cerebral aneurysm  $U - ICA$  than the ruptured cerebral aneurysm  $R - ICA$ . In a major of the studies, high OSI values are associated with the ruptured cerebral aneurysms. Moreover, high OSI values are associated with endothelial cell dysfunctions and vascular remodeling of the cerebral arteries. As a consequence, since unruptured cerebral aneurysm  $U - ICA$  has high OSI values, it could be interpreted that there might be a high rupture risk within  $U - ICA$  geometry. However, in order to examine rupture status within cerebral aneurysms, there is a strong need for further series of analysis by researchers around the world.

Moreover, since low WSS and high SWSSG are associated with disturbed flow, it might be interpreted that, ruptured cerebral aneurysm  $R - ICA$  has more disturbed flow regions than unruptured cerebral aneurysm  $U - ICA$ .



# HESAPLAMALI AKIŞKANLAR DİNAMIĞI KULLANARAK HEMODİNAMİK FAKTÖRLERİN ANALİZİ İLE HASTAYA ÖZGÜ BEYİN ANEVRİZMALARININ YIRTIлма DURUMU İNCELEMESİ

## ÖZET

Beyin anevrizmaları, dünya çapındaki populasyon düşünüldüğünde çok sık görülen bir durum olmakla beraber, ciddi anlamda yüksek hastalık ve ölüm oranlarıyla ilişkilidir. Temelde, anevrizmalar kan damarı duvarlarındaki patolojik ve anormal yapılarıdır. Anevrizma çeşitleri, içsi ve sakküler olmak üzere şekil bakımından ikiye ayrılır. İçsi anevrizmalar, daha çok vücudun karın aortu bölgesinde lokalize olurken, sakküler anevrizmalar çoğunlukla beyin bölgesindeki Willis çemberi etrafında lokalize olurlar. Sakküler anevrizmalar, Willis çemberi etrafındaki lokalize olduğu damarın adını alarak, isimlendirilmesi yapılır. Örneğin, internal karotid arterde bulunan bir anevrizma ICA anevrizması (internal carotid artery aneurysm) olarak adlandırılır. Bunun yanı sıra, sakküler anevrizmalar lokalize oldukları damarlardaki konumuna göre de sınıflandırılır ve ikiye ayrılır. Anevrizma oluşumunun gerçekleştiği bölgede aferent kan akışının çatallanan kan damarlarıyla en az iki eferent akış yoluna ayrılmasıyla çatallanan bölgenin ortasında oluşan anevrizmaya bifürkasyon veya terminal anevrizma adı verilir. Bu tip anevrizmalara Willis çemberindeki baziler arter anevrizması örnek verilebilir. Bir diğer çeşidinde de anevrizma oluşumunun gerçekleştiği bölgede aferent ve eferent akış aynı kan damarı üzerinde bulunursa, anevrizma kan damarının yanıl duvarında meydana gelir ve bu anevrizma çeşidine yan çeper anevrizması veya lateral anevrizma adı verilir. Bu çeşit anevrizmalara internal karotid arter anevrizması örnek olarak verilebilir. Bu çalışmada biri rüptür olan ve biri rüptür olmayan toplam iki adet sakküler, lateral anevrizma çeşidine sahip internal karotid arter anevrizmalarında, Newton uyumlu olmayan, düzensiz zamana bağlı pulsatil kan akışı modellenmesi gerçekleştirilmiştir. Bunun yanı sıra, bu özelliklere bir de türbülans akış altında bakılıp inceleme gerçekleştirilmiştir.

İntrakraniyal anevrizmalar, bir diğer deyişle, beyin anevrizmaları, beyin arterinin zayıflamasıyla meydana gelir ve önceden de belirtildiği üzere, genellikle Willis çemberinde lokalize olan arteryel duvarın anormal genişlemeleridir. İntrakranial anevrizmalar üç adet evreden meydana gelir. Bu evreler, sırasıyla, anevrizma oluşumu, anevrizma büyümesi ve son olarak da anevrizma yırtılmasıdır. Anevrizma yırtılması tıp dünyasında anevrizma rüptürü olarak adlandırılır. Beyin anevrizmasının rüptür olması halinde, hasta çok ciddi sağlık problemleriyle karşılaşabilir, hatta en kötü senaryoyu düşünecek olursak, bu yırtılma durumu, hastanın ölümüyle sonuçlanabilir. Beyin anevrizmalarının rüptür olması, beyinde bulunan subaraknoid boşluğa doğru olan kanamaya sebep olabilir. Bu durum, subaraknoid kanama veya tıp dünyasındaki ismiyle subaraknoid hemoraji olarak adlandırılır. Subaraknoid kanama beyin anevrizmalarının en ciddi problemlerinden biridir ve yüksek oranda hastalık ve ölüme sebebiyet verir. Bilim dünyasındaki istatistiklerden yola çıkarak, subaraknoid kanamaya %85 gibi büyük bir oranla beyin anevrizmalarının sebep olduğunun altı dikkatle çizilmiştir. Anevrizma rüptürü geçiren hastalar, ne yazık ki, ya bir ay

içerisinde ölür ya da yaşam kalitelerini ciddi anlamda düşürecek yetersizliklere sahip olurlar. Tüm bu nedenlerden dolayı, beyin anevrizmalarının yırtılma durumunun incelenmesi, rüptür riskinin önceden bilinip doğru tedavi uygulanabilmesi için, önemli ölçüde elzemdir.

Kan damarlarının akış koşullarıyla yeniden şekillenmesi ile ilgili ilk çalışmalar Virchow tarafından yapılmış olup asırlar öncesine, 1800'lü yıllara dayanmaktadır. O zamanlardan beri, bilim insanları kan dolaşım sistemini incelemek için yoğun bir şekilde kan damarları ve kan akışlarıyla ilgili çalışmalarını sürdürmektedirler. İntrakranial anevrizmalar ve arterlerde kan akışını incelemek açısından, bilgisayar ve hesaplamalı akışkanlar dinamiği tabanlı çalışmaların olmadığı eski zamanlarda, kan dolaşım sistemindeki kan akışı karmaşıklığının gizemli dünyasını keşfetmek adına, bilim insanları hayvan deneylerini gerçekleştiriyorlardı. Teknolojinin hızla yükselmesiyle birlikte, hem görüntü tekniklerinin kalitelileşmesi hem de bilgisayar yazılımlarının gelişmesi, hastaya özgü beyin anevrizmalarının hesaplı akışkanlar dinamiği kullanılarak araştırılması ortaya umut vaadedici sonuçlar çıkardı. Bilgisayar sistemlerinin hızla güçlenmesi, in-vivo ortamlarda, diğer bir deyişle, yaşayan organizmalarda yapılması imkansız sayılabilecek araştırmaları, bilgisayar tabanlı kan akışı çalışmalarında mümkün kıldı.

Önceki yıllarda, bu kan akış modellemeleri, basit bir yapay boru geometrisi içerisinde gerçekleştiriliyordu. Bu tip çalışmaların, gerçeklikten uzak bir modelleme ortamının yaratılmasının yanı sıra, güvenilir ve kaliteli sonuçlar vermemesi büyük ölçüde olasıdır. Özellikle, beyin anevrizmaları gibi karmaşık yapılar düşünüldüğünde, yapay düz bir boru geometrisinin, yine yapay küresel bir yapı ile birleştirilip simülasyon yapılması, ciddi anlamda yanıltıcı sonuçlara sebebiyet verir. Son yıllardaki görüntüleme tekniklerinin ve teknolojilerinin gelişmesiyle birlikte, hastaya özgü beyin damarları ve beyin anevrizmalarının geometrileri elde edilebilmekte, ve hesaplamalı akışkanlar dinamiği tabanlı üç boyutlu kan akışı simülasyonları hastaya özgü beyin anevrizmaları içerisinde gerçekleştirilebilmektedir.

Kan akışının beyin anevrizmalarında gerçekçi modellenebilmesi için, hastaya özgü geometrilerin kullanılmasının yanı sıra, yapı bakımından çok karmaşık olan kanın da gerçeğe uygun modellenmesi gerekmektedir. Temelde, kan, hücrelere oksijen ve besin sağlayan, ve metabolik atıkların bu hücrelerden uzaklaştırılmasına yardım eden bir vücut sıvısı olmasının yanı sıra, aynı zamanda sıvı bağ dokusu olma özelliğini de taşır. Kan, bileşenlerinden dolayı karmaşık bir oluşumdur. Bu bileşenlerden ilki, içerisinde glukoz ve protein gibi çözülmüş maddeler barındıran ve Newton uyumlu özellik gösteren, homojen yapıda bir sıvı solüsyon olan plazmadır. İkinci bileşen ise, plazma içerisinde askıda duran, tam kan yapısına sadece bir süspansiyon özelliği değil, aynı zamanda Newton uyumlu olmayan bir özellik katan, başta kırmızı kan hücreleri olmak üzere, beyaz kan hücreleri ve trombositlerden oluşan hücresel elementlerden oluşmaktadır.

Kırmızı kan hücreleri, diğer hücrelere oranla, kan içerisinde en çok bulunan hücre olma özelliğini taşır. Bu hücreler, yapılarında mitokondri ve nükleus, diğer bir adıyla hücre çekirdeği, bulundurmamalarıyla, diğer hücrelerden farklılık gösterip özelleşmiş yapıdadırlar. Bu özellikleri, kırmızı kan hücrelerinin, hemoglobin proteinine daha çok yer ayırmalarını sağlamaktadır. Kırmızı kan hücrelerinin temel görevi, bütün hücrelere oksijen taşımaktır. Bu hücrelerin kalınlıkları yaklaşık olarak  $2\mu m$  olup, yaklaşık  $8\mu m$  çapları vardır. Bu boyutsal yapıya rağmen, vücudumuzda bulunan en



küçük kan damarları olan çapı  $6\mu m$  'den az olan kılcal damarlardan bile geçerek bütün hücelere oksijen dağıtımını gerçekleştirir. Bu geçişi gerçekleştirmek için, sıkışma davranışı sergilenmektedir ve bu davranış kanın viskozite karakteristiğini etkiler. Viskozite, reoloji ile ilgili olduğu için, kanın kılcal damarlarda Newton uyumlu olmayan davranış gösterdiğini, 1931 yılında Fahræus and Lindqvist yaptıkları bir deneyle kanıtlamışlardır. 1966 yılında, Chien ve ekibi tam kanda kayma gerilmesi ve kayma hızı arasında doğrusal bir ilişki olmadığını gösterip, normal hematokrit düzeyine sahip tam kanda Newton uyumlu olmayan özellik gözlemlenmiştir. 1972 yılında Thurston, kanın Newton uyumlu olmayan özelliğe sahip olmasının yanı sıra, aynı zamanda viskoelastik davranış gösterdiğini de kanıtladı.

Kırmızı kan hücrelerinin kanın reolojik yapısına olan etkisiyle, tam kanın, Newton uyumlu olmayan kayma incelenmesi özelliği ve bunun dışında sahip olduğu viskoelastik yapısı, kan akışını, özellikle hastaya özgü beyin anevrizmaları gibi kompleks geometrilerde, matematiksel olarak modelleyip çözülecek olan problemi karmaşık kılar. Kan akışının karmaşıklığı sadece kanın yapısal özellikleriyle sınırlı kalmaz, bunun dışında, kanın dalgalı hareketi de, hastaya özgü beyin anevrizmalarında kan akışının matematiksel modellenmesi ve simülasyonu için olan çalışmaları daha da karmaşık hale getirmektedir. Kan, pulsatil olarak adlandırığımız, dalga hareketine benzer bir şekilde kalp tarafından periyodik olarak pompalanıp kan damarları yolu ile bütün vücuda dağılmaktadır. Kanın bu hareketi, bir hayvansal deney ile 1955 yılında McDonald tarafından çalışılmış olup, aynı yıllarda da bu hareketin matematiksel olarak ifadeleri Womersley tarafından çalışılmıştır. Kanın, periyodik olarak kalp tarafından pompalanıp ritmik olarak sistol ve diyastol zamanında değişiklik gösteren pulsatil hareketi matematiksel olarak Womersley profili ile ifade edilmektedir. Kanın hem yapısal hem de hareketel davranışları, hastaya özgü geometrilerde, özellikle beyin anevrizmaları gibi anormal geometrilerde, matematiksel olarak modellenmesini ve simülasyonunu güçleştirmektedir. Kanın damardaki pulsatil hareketini göz ardı edip, bu yapıyı zamandan bağımsız olarak modellemek, yapılan çalışmayı gerçeklikten uzak kıldığı ve problemi basitleştirdiği gibi bir de elde edilen sonuçların yanıltıcı olmasına sebebiyet verebilir. Bu problemlerden kaçınmak ve kan akış hareketini gerçekçi modellemek amaçlı, bu çalışmada kan, Womersley profil kabulüyle, zamana bağlı düzensiz pulsatil akış olarak modellenmiştir. Aynı şekilde, kanın yapısal özelliğini ihmal ederek modelleme yapmak, bu karmaşık yapıyı basitleştirip, gerçeklikten uzaklaşmaya ve bunun sonucunda elde edilen bilgilerin araştırmacıları yanıltıcı yorumlara itebileceği gerçeği olasıdır. Yanıltıcı sonuçlardan kaçınabilmek adına, bu çalışmada kan, Newton uyumlu olmayan kayma incelenmesi özelliği ile modellenip, bu viskozite modeli için de deneysel verilere oturtulan, gerçekçiliğe çok yakın olan Carreau-Yasuda viskozite modeli kullanılmıştır.

Hastaya özgü beyin anevrizmalarının incelenmesi çalışmalarında, hesaplı akışkanlar dinamiği tabanlı araştırmaların ve hemodinamik faktörlerin, anevrizma fazları olan anevrizma oluşumu, anevrizma büyümesi ve anevrizma yırtılması üzerinde önemli ölçüde rol oynadığı gösterilmiştir. Akabinde, bir çok araştırmacı bu alandaki çalışmalar için hesaplamalı akışkanlar dinamiği ile hemodinamik faktörleri analiz ederek yoğun olarak incelemeler yapmaktadırlar. Bununla birlikte, beyin anevrizmalarının rüptür riski bakımından olan çalışmalarda hemodinamik faktörler açısından karşıt görüşler hala varlığını sürdürmektedir. Bu sebepten dolayı, hala tam olarak anlaşılmayan hemodinamik faktörlerin beyin anevrizmaları üzerindeki etkilerini anlaşılır kılmak için, hesaplamalı akışkanlar dinamiği tabanlı çalışmaların

sürdürülmesine büyük ölçüde ihtiyaç duyulmaktadır. Bu çalışmada, beyin anevrizmalarının rüptür durumları, hemodinamik faktörlere dayalı olarak incelenmiş, bu amacı gerçekleştirmek için, hastaya özgü beyin anevrizma geometrileri kullanılıp, hesaplamalı akışkanlar dinamiği çalışmalarını gerçekleştirmek için de C++ tabanlı açık kaynak bir yazılım olan OpenFOAM yazılımı kullanılmıştır.

Hesaplamalı akışkanlar dinamiğinin popüleritesi teknolojinin gelişmesiyle birlikte yaygınlaşmış, ve bu teknoloji beyin anevrizmalarındaki kan akışı modellemeleri için umut kaynağı olmuştur. Bununla birlikte, eğer ağ ayırma duyarlılığı karmaşık anevrizma geometrisi ile örtüşmez ise simülasyon sonuçları yanıltıcı olabilir. Bunun üstesinden gelebilmek adına, hesaplamalı akışkanlar dinamiği çalışmalarında ayrıklaştırma hataları değerlendirilmesine güçlü bir ihtiyaç vardır. Hata analizleri çalışmaları Roache tarafından önerilip, daha sonra geniş ölçüde araştırmacılar tarafından hesaplamalı akışkanlar dinamiği çalışmalarında kullanımı yaygınlaşmıştır. Hata analizlerinin önemi dikkate alınıp, yanıltıcı sonuçlardan kaçınabilmek için bu çalışmada, genelleştirilmiş Richardson Ekstrapolasyonu tabanlı ağ yakınsama indeksi metodu ayrıklaştırma hatalarının değerlendirilmesi adına uygulanmıştır. Ağ yakınsama indeksi çalışması için, beş farklı ağ eleman sayısına sahip geometrilerde analiz yapılmış, bunlar arasından en hassas üç tanesinin arasında ağ yakınsama indeksi değerleri tablolar halinde verilmiştir. Elde edilen sonuçlar yakınsama aralığına uyum sağlamış olup, Richardson Ekstrapolasyonu sonucuyla da birebir örtüşmektedir.

Kan damarları yaşayan canlı organlar olduğundan dolayı, hem vücut içindeki kimyasal ve fiziksel değişikliklere hem de dışarıdan gelen uyarıya kendi iç dengesini korumak için tepki gösterirler. Dolayısı ile, farklılık gösteren hemodinamik şartlar altında, uyum sağlama amaçlı olarak büzülme ve genişleme hareketleri yapmaktadırlar. Vücutta anormal hemodinamik etkiler olduğu zaman, bu etkilere tepki vermek için ya molekül sentezleme yoluna giderler ya da kan damarı duvarlarını yeniden şekillendirirler. Beyin anevrizmaları da, beyindeki Willis çemberinde lokalize olmuş kan damarlarının patolojik genişlemesi bir başka deyişle kan damarlarının yeniden şekillenmesinin bir ürünü olduğu için hemodinamik faktörlerin anevrizma oluşumuna, büyümesine ve yırtılmasına olan etkileri önemli ölçüde büyüktür. Bu çalışmada, anevrizma rüptürü durumu incelemesi, hesaplamalı akışkanlar dinamiği yardımıyla hemodinamik faktörler analiz edilerek yapılmıştır. Kullanılan hemodinamik faktörler, anevrizma çalışmalarında yoğunlukla kullanılan duvar kayma gerilmesi, damarın yeniden şekillenmesinde büyük rol alan salınımlı kayma indeksi, zamana göre ortalaması alınmış duvar kayma gerilmesi, iç zar gözesi tarafından gen ekspresyonu yaparak ve damar duvarı şekillendirmede rol alarak anevrizma oluşumuna sebep olduğu bilinen, bunun yanı sıra iltihaba neden olan etkilere de rol alan konumsal duvar kayma gerilmesi gradyanı, zamana göre ortalaması alınmış konumsal duvar kayma gerilmesi gradyanı, hız ve basınç olarak çalışmada yer almaktadır.

Bu çalışmada, daha önce belirtildiği üzere, biri rüptür olup 26 yaşında kadın bir hastaya aittir ve diğeri rüptür olmayan 48 yaşında kadın bir hastaya ait olmak üzere toplam iki adet hastaya özgü beyin anevrizma modelleri kullanılmıştır. Orijinal geometriler, ilgi bölgesine göre kesilip, düzgün akışın giriş çıkışı için her ekstremitte bölgesine uygun ölçüde uzantılar eklenmiştir. Geometrilere hacim ağı üretmek için, sistem kapalı bir hale getirilip giriş çıkış bölgeleri kapatılmıştır. Hastaya özgü beyin anevrizma datalarına yapılan bu işlemler açık kaynaklı the Vascular Modeling Toolkit (VMTK) kullanılarak gerçekleştirilmiştir.

Geometrilerde yüzeysel ve hacimsel ağ üretimi için ICEM CFD 19.2 (ANSYS, Inc., Canonsburg, PA, USA) ağ üreticisi yazılımı kullanılmış olup, ağ çeşidi dörtyüzlü ağ olarak üretilmiştir. Bütün simülasyonlar, OpenFOAM yazılımına ait kapalı metod kullanan pisoFOAM çözücüsünde sonlu hacim yöntemi altında OpenFOAM yazılımı kullanılarak gerçekleştirilmiştir. Kullanılan hemodinamik faktörlerin görselleştirmeleri, açık kaynaklı bir yazılım olan ParaView kullanılarak yapılmıştır. Bu tezin yazımında  $\LaTeX$  kullanılmıştır.

Hastaya özgü beyin anevrizmalarındaki kan akışı modellenmesi, Navier-Stokes denklemleri altında, düzensiz zamana bağlı pulsatil davranışı ile modellenip ayrıca kanın Newton uyumlu olmayan, kayma incilmesi özelliğini hesaba katarak bu özelliği vermek için Carreau-Yasuda viskozite modeli kullanılmış olup sıkıştırılmaz akış olarak gerçekleştirilmiştir. Kan damarları, kaymaz sınır koşulları ile sabit olarak modellenmiştir. Simülasyonlar hem rüptür model hem de rüptür olmayan model için, geçişli ve türbülans akış modellenmesi yapılarak ayrı ayrı hesaplanmıştır. Türbülans modeli yaratmak için, pisoFOAM çözücüsü kullanılarak, dinamik k-denklemleri büyük girdap benzeşim yöntemi için OpenFOAM kullanılarak çözülmüştür.

Bu çalışmada, simülasyon sonuçları ile elde edilen hemodinamik faktörler, literatürdeki data ile kıyaslanarak nümerik doğruluğu yapılmıştır. Simülasyon sonuçları, hastaya özgü beyin anevrizmalarında, özellikle anevrizma keseciği bölgesinde, bilhassa sistol zamanında artan Reynolds sayılarının da etkisiyle türbülans etkilerin yoğun olarak hissedildiğini göstermiştir. Türbülans etkileri, geçişli simülasyonlara nazaran, salınımlı kayma indeksini de değer olarak arttırmıştır. Rüptür modelde rüptür olmayan modele göre duvar kayma gerilmesi değerleri daha düşük gözlemlenip, literatür ile desteklenmiştir. Rüptür olmayan geometride gözlemlenen, salınımlı kayma indeksinin yüksek değerleri, bu model için rüptür riskinin yüksek olabileceğine işaret etmektedir. Her iki geometride de akış çizgileri, giriş bölgesinde düzgün davranış sergilerken, kıvrımlara geçtikçe geçişli bir davranış sergileyip, anevrizma kesesi içinde de büyük ölçüde kaotik bir davranış sergilemiştir. Duvar kayma gerilmesi vektörleri türbülans etkiler altında farklı yön davranışları yaparak salınım kayma indeksinin değerini arttırıp, canlı organ olan damarı yeniden şekillendirmeye zorlamıştır. Ayrıca, rüptür geometrinin sahip olduğu düşük duvar kayma gerilmesi ve yüksek konumsal duvar kayma gerilmesi gradyanı, bu anevrizmada önemli ölçüde dengesiz akış bölgelerinin fazlalığına işaret etmektedir.



## 1. INTRODUCTION

Cerebral aneurysms are quite common on a worldwide scale of population [1–5] and related to high morbidity and mortality rate [2, 6, 7]. Especially, the rupture of an intracranial aneurysm might lead to the bleeding into the subarachnoid space, this phenomenon is called subarachnoid hemorrhage (SAH). SAH is the most serious problem of brain aneurysms and causes high risk of death and disability [8–14]. It is remarked that cerebral aneurysms are the reason of SAH with a rate of 85% [15]. People who have aneurysm rupture, either die within one month or have serious disabilities [2, 4, 11]. Therefore, it is very important to make an accurate prediction for rupture risk of intracranial aneurysms.

Cerebral aneurysms arise from the weakness of the cerebral artery and they are abnormal dilations of the arterial wall that usually localized in the Circle of Willis (CoW) [8, 16–18]. There are three steps for intracranial aneurysms and these steps are called formation, growth and rupture, respectively [19–21]. A large number of different risk factors and sometimes combination of them cause the initiation, growth and rupture of the aneurysm [22]. Some risk factors such as smoking, cocaine consumption, hypertension, high alcohol consumption and so forth are under consideration to cause to each steps of the aneurysm by increasing blood pressure of the patient [4, 23, 24]. Cebal et al. [25] published a comprehensive review article about connection between risk factors which are grouped as location, peri-aneurysmal environment, multiplicity, geometry, hemodynamics, vascular wall, genetics and clinical factors. In [25], some groups were investigated into sub-groups e.g. aneurysm location: posterior circulation, anterior circulation and CoW. The risk factors of cerebral aneurysms and their interactions from Cebal et al. [25] can be seen in Figure 1.1.

Aneurysm location and its morphological features are the most frequently used parameters to predict aneurysm rupture in clinical practice [2, 21, 26, 27]. However, the investigation based only on the location and the morphological features make

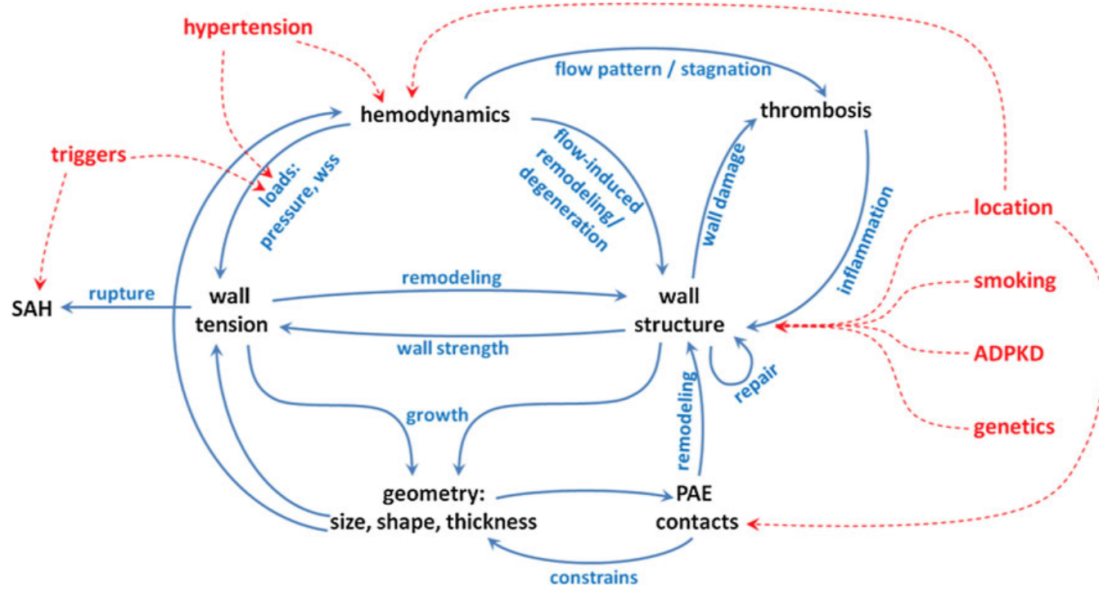


**Figure 1.1** : Intracranial aneurysm risk factors and their relations [25].

the rupture risk assessment oversimplify and less reliable [14, 21, 28]. It has been demonstrated that assessment based on computational fluid dynamics (CFD) and hemodynamic factors play a fundamental role to investigate intracranial aneurysm stages (initiation, growth and rupture) [19, 29–32]. In order to estimate rupture status, these promising techniques are getting more realistic and reliable tools [31, 33, 34]. Therefore, there is a strong need for computational methods and numerical analysis for an accurate rupture risk prediction [5, 19].

After demonstrating that hemodynamic factors have a significant role on aneurysms, a large number of studies for intracranial aneurysms have been examined in details by using CFD techniques [5, 19, 20, 34, 35]. Although these tools provide remarkable improvements, there are some contradictions about low wall shear stress (WSS) and high WSS theories in terms of hemodynamics in brain aneurysms [29, 30]. However, Meng et al. [19] reported that both theories have significant effects on aneurysm growth and rupture as seen in Figure 1.2 clearly. It can be found a comprehensive literature review respecting brain aneurysms, low and high WSS theories about growth and rupture with hemodynamic factors by using fluid dynamics in *Section 1.2* within this *Chapter*.

Modeling and simulation of the blood flow in an artificial straight pipe geometry instead of a patient specific geometry is a very primitive method and considering

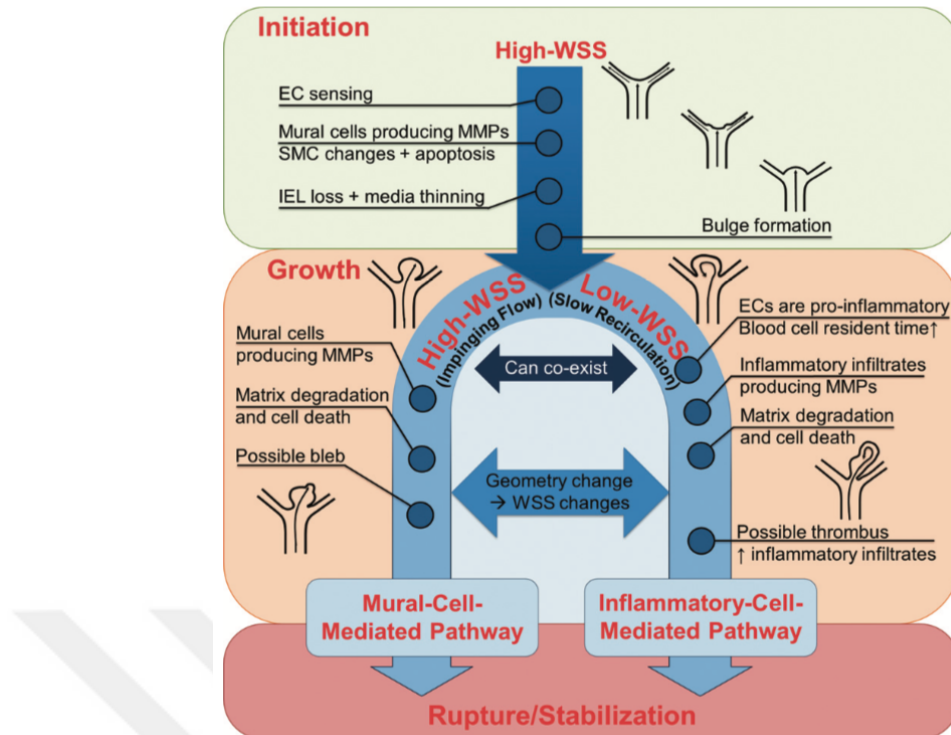


**Figure 1.2 :** The role of high and low WSS in aneurysm initiation, growth and rupture [19].

the complexity of human vessels, using a pipe geometry as a vessel is not realistic and reliable. With the developments of imaging technologies such as magnetic resonance imaging (MRI), computed tomography angiography (CTA) and imaging techniques such as acquisition, segmentation and processing, the quality of the images is becoming significantly high. With a combination of imaging techniques and CFD methods, patient specific models of cerebral aneurysms have been examined extensively [8, 35–37]. Patient specific geometry-based CFD simulations provide more reliable and realistic results to study hemodynamic factors, blood flow modeling and rupture status within intracranial aneurysms. [30, 35–39]. Also, it is notable to emphasize that hemodynamic factors have a major effect on brain aneurysms thus, investigations of rupture risk by using CFD on patient-specific geometries provide a precise prediction for diagnosis and treatment by individually in clinical practices [40–43].

Considering the importance of CFD listed above, in this thesis, patient-specific intracranial aneurysms have been studied regarding to blood flow modeling and simulation to investigate rupture status.

## 1.1 Literature Review

Blood vessel remodeling with flow conditions was studied long time ago by Virchow in 1800s. Thenceforward, a large number of researches have been performed in order to reveal the complexities of blood flow modeling in circulatory system. Particularly, development of technology provides computational-based researches an opportunity to investigate blood flow simulations that is unfeasible to perform by means of in-vivo methods. Before computer-based examinations in the sense of cerebral aneurysms and blood flow in arteries, animal-based experiments had been performed notably to discover this secret world of blood flow complexity in circulatory system. Since blood is pumped by the heart with a periodic wave-like motion, this phenomenon is defined as pulsatile flow [44]. In 1955, McDonald [45] performed an animal-based experiment using the femoral artery of a dog and demonstrated the phasic changes of blood flow throughout each cardiac cycle, and this type of flow formed by pressure oscillations. McDonald [45] took the advantage of the equations derived from Womersley [46] to calculate flow curves, and showed that the similarity of flow patterns between rabbit aorta [47] and dog femoral artery [45], the velocity of flow against one cardiac cycle duration can be found in Figure 1.3.

The complexity of flow patterns and Womersley profile [44] of blood flow are not the only challenges. As discussed extensively in *Chapter 2*, the features of blood make this liquid to act like shear-thinning non-Newtonian and viscoelastic in terms of rheological properties [48–50]. In 1969, Merrill [49] published a very comprehensive paper with regards to non-Newtonian rheology of blood including theory and equations. Due to its rheologic nature and wave-like inlet profile, mathematical modeling of blood flow is a challenging study, more particularly in complex and abnormal patient-specific vessels such as intracranial aneurysms.

In 1971, one of the earliest researches regarding to mathematical modeling of intracranial aneurysms located in the CoW was studied via Duffing Equation and electrical circuit by Austin [51]. Subsequently, in 1974, Cronin [52] analyzed



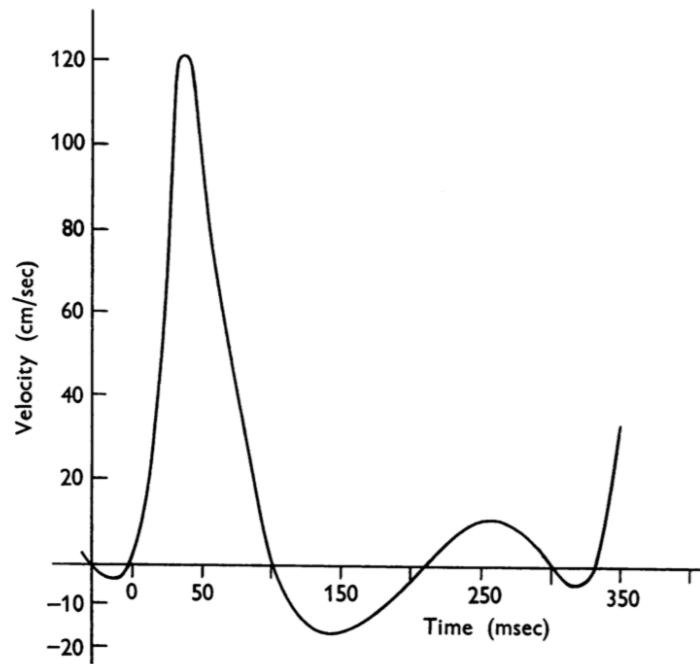


**Figure 1.3** : The flow velocity in the femoral artery of the dog during one cardiac cycle [45].

the differential equation derived from Austin [51] by using qualitative method and concluded high and lowered pulse rate might be dangerous for aneurysm. In 1989, Perktold et al. [53] analyzed blood flow in an idealized arterial bifurcation based-on computer simulation with pulsatile inlet profile by solving the governing equations numerically using finite element method (FEM). Due to the rheology of blood, they examined the difference between non-Newtonian and Newtonian flow, afterwards they concluded that considering large arteries, no significant difference has been observed.

The mostly used parameters in terms of hemodynamics are WSS and oscillatory shear index (OSI) in cerebral aneurysms [8, 19, 30, 54, 55]. In 1985, OSI was proposed by Ku et al. [56] to quantify the shear stress acting on the vessel wall with pulsatile flow. After realizing that OSI has a significant role in order to analyze aneurysm steps, this parameter has been used numerously in addition to WSS in cerebral aneurysm studies [8, 14, 19, 30, 57].

In order to explain in more detail how these hemodynamic parameters have been used in cerebral aneurysm studies, in 2004 Shojima et al. [54] published a paper about WSS from the point of view of magnitude and the role on middle cerebral artery (MCA) aneurysms (See Figure 1.4). The data they analyzed were acquired by using three dimensional computed tomographic angiography (3D-CTA) from 19 patients with

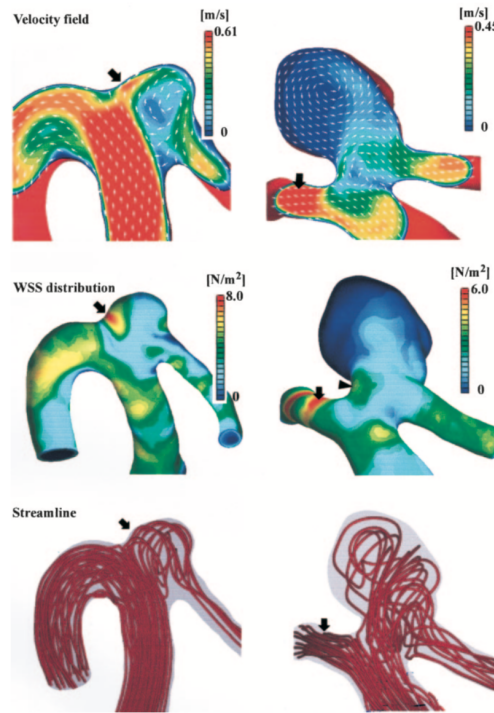


**Figure 1.4** : Velocity field, WSS distribution and streamline visualizations of two unruptured aneurysms, the arrows indicate the sites of maximum WSS, Shojima et al. [54].

a total amount of 20 aneurysms. Due to the WSS assessments, CFD calculations were examined for 5 cardiac cycles with their original finite-element solver described by Navier-Stokes equations. They assumed the blood as incompressible, pulsatile, Newtonian with a dynamic viscosity of  $4 \times 10^{-3} \text{ N/m}^2$  per second and the vessel wall as rigid with no-slip boundary condition. They deduced that low WSS might lead to the growth and the rupture steps of an aneurysm as a consequence of abnormal changes in the vessel wall. They also noted that WSS might be a strong parameter to enable rupture risk prediction.

Shojima and his colleagues [54] were not the only ones to consider the association between low WSS and aneurysm rupture. Xiang et al. [30] examined various morphological parameters such as aspect ratio (AR), size ratio (SR) and hemodynamic parameters such as WSS, OSI, relative residence time (RRT) to differentiate rupture status within intracranial aneurysms. They [30] analyzed 38 ruptured and 81 unruptured patient specific data acquired from three dimensional (3D) angiography. They [30] modeled blood flow as incompressible, Newtonian fluid with rigid vessel wall during 3 cardiac cycles under pulsatile flow profile using CFD. They [30] analyzed

morphological parameters, hemodynamic parameters one by one and a combination of them with a total amount of three different models experimenting upon ruptured and unruptured aneurysms. And they deduced that hemodynamics has a significant role to differentiate rupture status of intracranial aneurysms.

There are a number of discrepancies in consensus whether low WSS [30, 54, 58] or high WSS [59–62] might be associated with aneurysm rupture among the studies. In contrast to Shojima et al. [54] and Xiang et al. [30], Castro et al. [61] found an association between high level of maximum WSS and cerebral aneurysm rupture. They [61] had performed CFD simulations of blood flow with pulsatile, incompressible, Newtonian properties under three dimensional unsteady Navier-Stokes equations within the patient specific data acquired from 3D rotational angiography. They [61] had characterized varied flow types and examined peak WSS, impaction zone area and flow patterns of the blood in order to investigate the correlations among these parameters and aneurysm rupture. The results they [61] obtained demonstrated that high flow rates and maximum WSS have strong correlations with aneurysm rupture. They [61] noted that aneurysms which have small impaction zones are associated with rupture as well.

Likewise, Cebal et al. [59] had similar findings in terms of high WSS theory just as Castro et al. [61]. They [59] conducted a comprehensive image-based CFD study including both ruptured and unruptured 210 patient-specific cerebral aneurysm geometries from 128 patients that acquired from 3D rotational angiography. Their aim was to indicate quantitative evaluations correlated with their previous study [29][30] regarding to qualitative observations and to examine whether these quantitative measurements are associated with aneurysm rupture. Some of the parameters they [59] examined were: inflow concentration index (ICI), shear concentration index (SCI), kinetic energy ratio (KER) as aneurysm hemodynamic variables. As a consequence, there was a strong correlation between high level of maximum WSS and aneurysm rupture whereas low WSS did not have that correlation. They [59] also emphasized the importance of image-based CFD analysis in clinical practice to assess cerebral aneurysm risks. The hemodynamic reduction figure can be found in Figure 1.5.

As mentioned before, there are a large number of contradictory thoughts in consensus with regards to low and high WSS theories [30, 54, 59, 62]. Therewith, Meng et

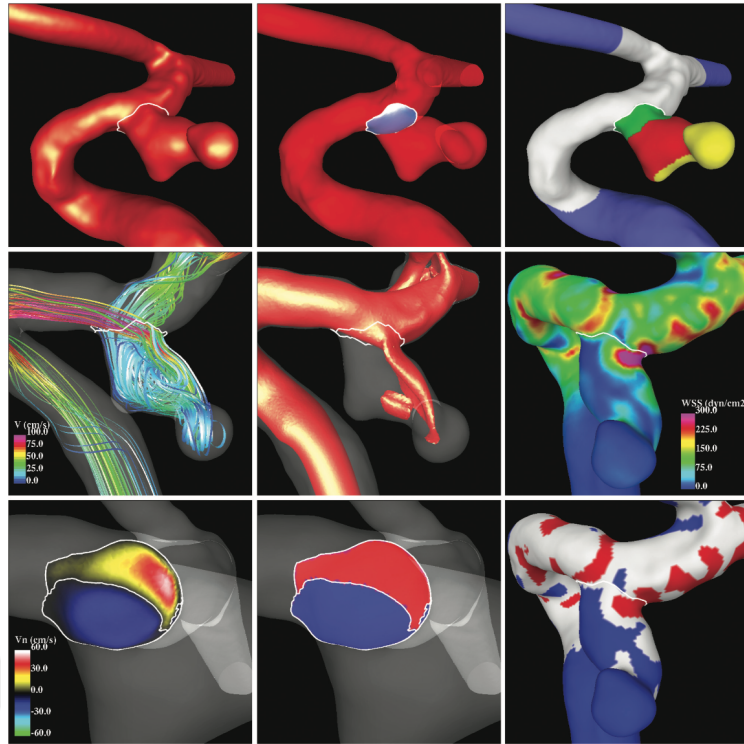


**Figure 1.5** : Hemodynamic effects on the aneurysms by Cebal et al. [59].

al. [19] has published a review article about the role of low and high WSS effects over the intracranial aneurysms and proposed two different biologic-hemodynamic models that drive an aneurysm growth and rupture: A combination of low WSS and high OSI may cause inflammatory-cell-mediated vessel wall deterioration and thrombus formation and eventually rupture of the aneurysm while a combination of high WSS and a positive WSS gradient may cause mural-cell-mediated vessel wall deterioration and as a consequence, the vessel wall might be thinner and eventually rupture might be occurred. Since both low and high hemodynamic conditions are abnormal, they both might change the balance of the vessel wall and might cause aneurysm rupture. Moreover, they [19] noted that these two different models might be associated with two aneurysm phenotypes: atherosclerotic aneurysms with thicker wall and translucent aneurysms with thinner wall. An explanatory schema can be found in Figure 1.6.

Another significant cerebral aneurysm study with regards to WSS, various viscosity models and flow profiles belongs to Evju et al. [5]. Their study [5] involved 12 MCA aneurysm geometries from CTA images. They performed mesh generation with a range of 800.000-1.200.000 tetrahedral elements and image segmentation to CTA images by using the Vascular Modeling Toolkit (VMTK) [63]. CFD calculations were run during

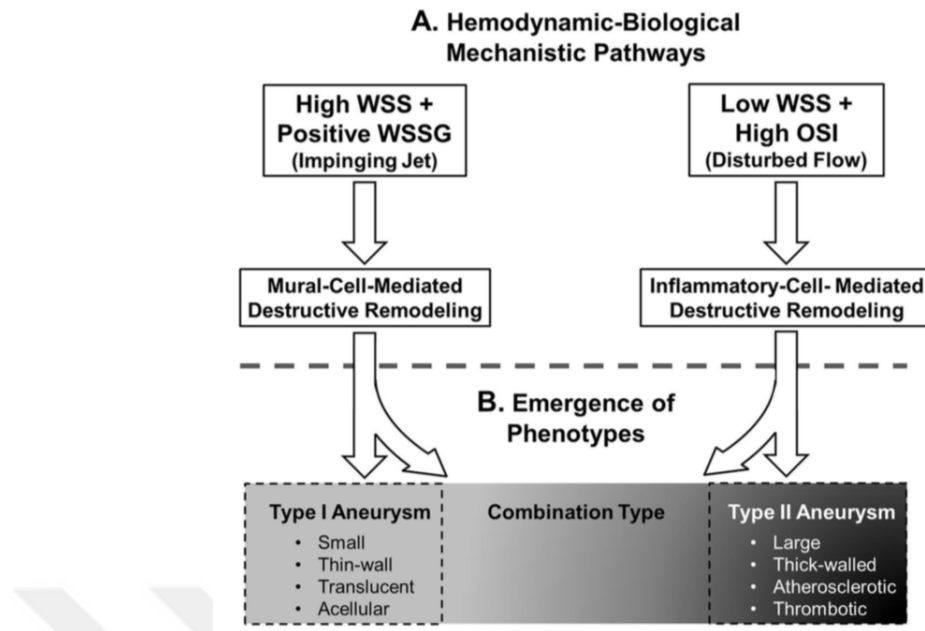


**Figure 1.6 :** Figure shows two independent hypotheses, (A) indicates hemodynamic-biologic pathways that cause intracranial aneurysm growth and rupture and (B) shows the relationship between them and intracranial aneurysm phenotypes proposed by Meng et al. [19].

four cycles under Navier-Stokes equations within 12 MCA aneurysm geometries for a total amount of 72 simulations. The various parameters were investigated among the simulations. The comparisons of the effects of various viscosity models such as Casson model, inlet and outlet conditions were examined with respect to three different WSS models. Thereafter, the results they obtained demonstrated that there is a significant relation between the viscosity models and the boundary conditions, on the contrary there is no significant relation between the different WSS models and classifications.

By means of increasing technologies and techniques of medical imaging, patient-specific computational hemodynamic methods are getting more realistic, accurate and reliable to investigate cerebral aneurysms and have been performed extensively by researchers [5, 8, 35–37, 64]. In 2003, Steinman et al. [35] published a paper addressing to combination of CFD and medical imaging techniques. Due to the lack of capabilities of in-vivo techniques, they [35] aimed to demonstrate that the combination of CFD and computed rotational angiography enables to get hemodynamic information. They [35] performed CFD calculations within patient-specific cerebral aneurysm model assuming rigid vessel walls during 3 cardiac cycles under pulsatile flow conditions with a Womersley number of 3 and Reynolds

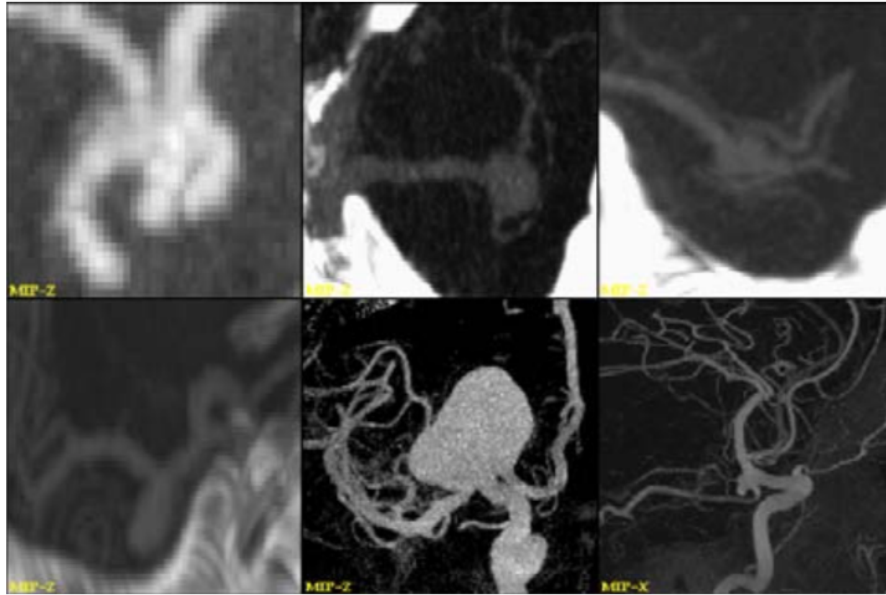


**Figure 1.7** : The figure provided by Cebal et al. [36]: "Maximum intensity projections (MIP) of intracranial aneurysms from CTA and 3DRA."

number of 336. Their study provided the first analysis of patient-specific hemodynamic information of the aneurysm based on CFD methods and in-vivo 3D angiography thus enlightened the significance of the combination of CFD and imaging techniques in clinical practice.

Similarly to Steinman et al. [35], Cebal et. al [36] agreed that image-based CFD methods might aid the diagnosis and the treatment of the cerebral aneurysms. Thus, they [36] also performed the combination of finite element methods within patient-specific cerebral aneurysms and medical imaging techniques. They [36] modelled the blood as incompressible, unsteady, Newtonian fluid under the Navier-Stokes equations. They [36] assumed no-slip boundary conditions for the vessel walls and used fully developed pulsatile inlet velocity profile for the inflow conditions. CFD calculations were performed within six patient specific geometries acquired by CTA (4 geometries) and 3D rotational angiography (2 geometries) (See Figure 1.7). The results they obtained indicated that when the flow impinges on the aneurysm vessel walls with a high speed, WSS increases as a consequence. They [36] also noted that CFD methods based on patient-specific geometries might be advantageous tools in clinical practice.

Intracranial aneurysms have quite complex structures with curvatures and connectivities between parent and daughter vessels. 3D rotational angiography is the most

frequently used technique to obtain high quality images of CoW. Nevertheless, this technique has limitations to obtain whole 3D model to examine patient-specific CFD when it comes to aneurysms with two sources of the blood inflow. Some of the cerebral aneurysms localized in the CoW such as basilar tip aneurysms have two sources of the blood inflow and examinations without obtaining a complete model of these aneurysms reduce the accuracy of the patient-specific CFD calculations. In order to come through this issue, Castro et al. [64] presented a novel method that combines image co-registration and surface-merging techniques together to construct patient-specific cerebral aneurysms with two source of blood inflow from rotational angiography images.

Despite the fact that acquiring the high resolution images of cerebral aneurysms, the investigations are not quite accurate due to the lack of patient-specific flow informations in a major part of the studies [8, 14, 65]. Besides these limitations, it is remarkable to emphasize that the majority of the image data of the ruptured cerebral aneurysms are acquired after rupture occurred. Nevertheless, the shape of the cerebral aneurysms might change after rupture. Generally, it is assumed that the changes are small enough to neglect the difference between before and after rupture of an aneurysm. Thereupon, Rahman et al. [66] examined the image data of the cerebral aneurysms before and after rupture from 13 patients. They [66] evaluated the patients with some parameters such as neck diameter and maximal width. The results they obtained demonstrated that there was no remarkable difference in terms of the size of the aneurysms. Six ruptured aneurysms were detected with an increase of the size around 2 millimeters (mm) comparing their unruptured status. They [66] concluded that the unruptured aneurysms do not decrease in terms of size after the rupture occurred.

The blood could be modeled either Newtonian or non-Newtonian properties of the fluid according to the assumptions. With regards to Newtonian and non-Newtonian models for blood flow that the researchers assumed, Campo-Deano et al. [67] presented very explanatory tables with boundary conditions metrics.

Notwithstanding a great majority of the image-based CFD within the cerebral aneurysm studies neglect the non-Newtonian shear-thinning features of the blood and assume the blood as Newtonian fluid, Valencia et al. [68] studied fluid dynamics

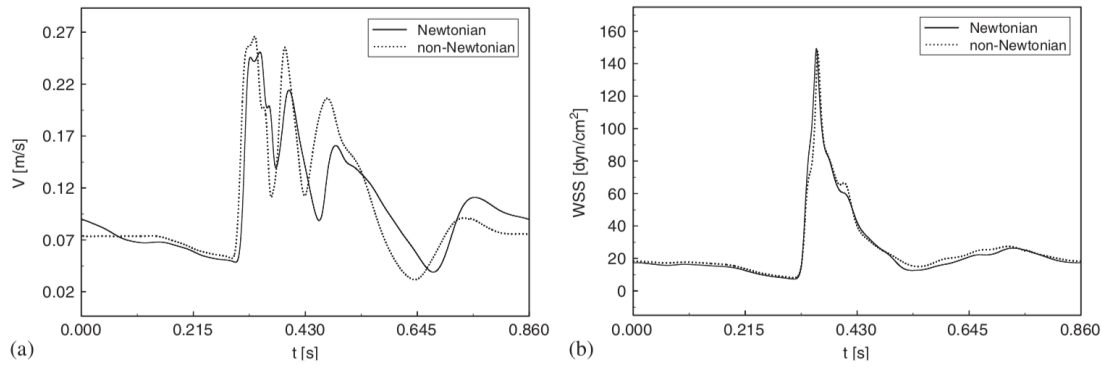


**Figure 1.8 :** In the figure (a) shows the velocity magnitude in the centre of the aneurysm; and (b) shows the WSS in one point of the aneurysm dome by Valencia et al. [68].

in a patient-specific saccular aneurysm image data obtained from 3D rotational angiography, with assumptions of the blood as Newtonian and non-Newtonian fluids under a wave-like inlet profile. CFD calculations for blood flow were performed under incompressible, unsteady laminar flow and they [68] used a fine mesh with 283.115 elements. They [68] investigated WSS and flow characteristics under non-Newtonian blood properties. The results they obtained demonstrated that non-Newtonian features on the WSS was significant only in the arterial zones with high velocity gradients, on the other hand, Newtonian and non-Newtonian fluids were similar on the aneurysmal wall (Fig 1.8).

The contradictions about the theories of high or low WSS, limitations of imaging techniques, modeling the blood with Newtonian or non-Newtonian properties, the change of the aneurysm geometry after rupture are not the only challenging parts of the CFD with patient-specific intracranial aneurysms. The another challenging part of modeling blood flow within an intracranial aneurysm is to count on the structure metrics of the vessel walls. A majority of the studies of the cerebral aneurysms with regards to hemodynamics are under assumption that vessel walls are rigid. A fluid-structure interaction (FSI) study with regards to cerebral aneurysms was carried out by Torii et al [69]. They [69] performed two linearly elastic and one hyper-elastic constitutive models of cerebral aneurysms. They [69] concluded that although the hyper-elastic model is theoretically more preferred, the linearly elastic models might be used as an alternative due to the simple implementation. They noted that both



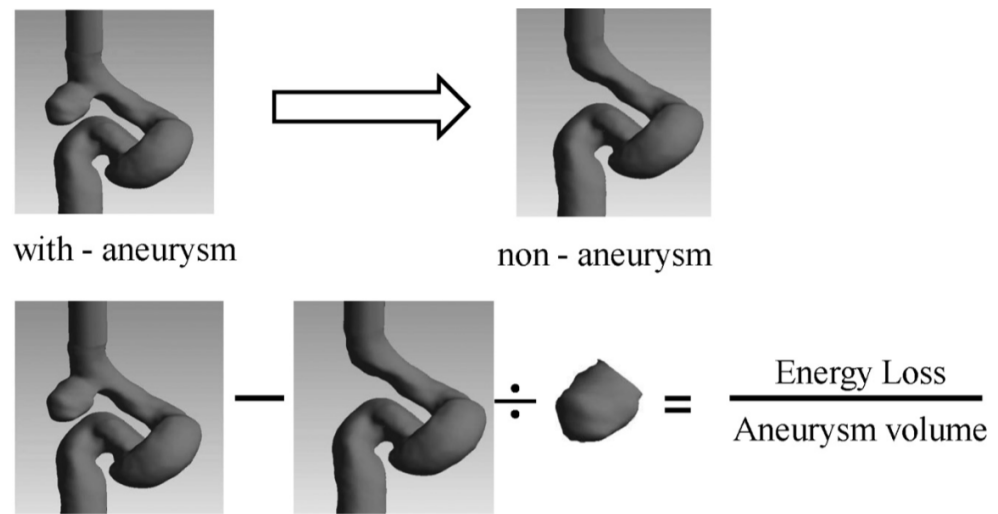


**Figure 1.9** : Energy loss (EL) calculation method by Qian et al. [31].

linearly elastic and hyper-elastic models could be performed to investigate cerebral aneurysms in terms of FSI.

Rupture risk analysis of the cerebral aneurysms by means of CFD techniques are quite significant for diagnosis and treatment in clinical practice so as to take precaution for the health of the patient. Apart from the hemodynamic factors such as WSS and OSI to analyze rupture risk of intracranial aneurysms, Qian et al. [31] proposed an additional quantitative hemodynamic parameter called energy loss (EL) (See Figure 1.9).

EL parameter was used as an alternative method to WSS and OSI to estimate the effects of the stable unruptured intracranial aneurysms. The blood fluid model they assumed was an incompressible, laminar and Newtonian fluid. They [31] performed CFD calculations with pulsatile flow conditions within aneurysm geometries during 3 cardiac cycles and with a time step of 500 for each cardiac cycle. The CFD calculations took for an hour on a PC with 2 CPU, 32 Gb RAM and 3.3 GHz processor for 3 cardiac cycles. They [31] used a mesh size with a range of 700.000 - 800.000 for tetrahedral cells of intracranial aneurysm geometries. They [31] compared the results between four coincidentally ruptured aneurysms and another 26 stable unruptured aneurysms in terms of WSS and EL and showed that in the ruptured aneurysms, EL factor was found considerably higher than the stable unruptured aneurysms. Their results demonstrated that blood flow patterns are more complex and unstable in ruptured aneurysm than

the unruptured ones. They also noted that there was no significant difference between ruptured and unruptured aneurysms in terms of time average WSS.

One of the most recently studies with respect to cerebral aneurysms hemodynamics belongs to Doddasomayajula et al. [70]. In 2017, they [70] investigated mirror aneurysms and ipsilateral multiple aneurysms in order to analyze if hemodynamic characteristics of the ruptured aneurysms differs from the unruptured ones within the same patient. They [70] used a mirror-pair model which means two aneurysms localized at the same anatomic zone, assessing 24 ruptured aneurysms and corresponding them, 24 unruptured aneurysms with a total amount of 48 aneurysms in 24 patients. CFD simulations were run putatively rigid vessel walls, Newtonian viscosity and pulsatile flow profile during 2 cardiac cycle. The results they obtained showed that the ruptured aneurysms have larger oscillatory WSS and aspect ratios than the unruptured ones. Also, they noted that the ruptured aneurysms had complex and unstable flows comparing to unruptured aneurysms.

Another recent study has been performed by Berg et al. [14] in 2018. They [14] analyzed multiple intracranial aneurysms instead of one aneurysm geometry. They studied 17 intracranial aneurysms from 4 female and 2 male patients. They analyzed morphologic features such as SR and AS besides hemodynamic features. The blood was modeled as incompressible, Newtonian fluid and CFD calculations have been performed during 3 cardiac cycles with a time step of 1 millisecond (ms). The hemodynamic parameters they analyzed were spatially mean and maximum time-averaged wall shear stresses, OSI, RRT and oscillatory velocity index (OVI) to compare between ruptured and unruptured cerebral aneurysms. The results they obtained showed that SR and AS were noteworthy higher in the ruptured aneurysms regarding to the geometrical parameters. As regards to hemodynamic factors, with a combination of high OSI and low averaged WSS were seen in the ruptured aneurysms. They [14] also mentioned that the ruptured aneurysms had complex and unstable flow patterns. The ruptured aneurysms also had the highest RRT values according to Berg et al. [14].

## **2. BIOLOGICAL CHARACTERISTICS**

### **2.1 Purpose**

Since the intracranial aneurysms might cause to serious health problems or even worse, might be end up with the death of the patient [6, 7, 10, 12], it is considerably crucial to investigate rupture status in order to estimate the rupture risks of the cerebral aneurysms. At the point where the in-vivo techniques are inadequate and when CFD techniques step in, the improvements of the researches increase the demands for computational methods. However, an accurate blood flow modeling within patient-specific cerebral aneurysms by means of computational methods requires profound knowledge of the biological structures and characteristics of the blood as well as cerebral aneurysms. The comprehension of the biological structures and characteristics of the blood such as density and velocity provides to obtain accurate results in this field. Therewithal, considering the types, morphological properties and locations of the aneurysms in order to model blood flow realistically provides more reliable results. Therefore, the purpose of this *Chapter* is to express the biological characteristics of the current study since it is significantly crucial to comprehend the properties of the blood as well as the structures of the blood vessels in order to model accurately blood flow within the patient-specific cerebral aneurysms.

### **2.2 The Characteristics of the Blood and Vessels**

Essentially, blood is a body fluid as well as a fluid connective tissue which is responsible for supplying oxygen and nutrients to the cells of the body and removing metabolic wastes away from the cells.

In principle, blood is a complex composition due to its constitutions: the liquid solution of the plasma which is a homogeneous liquid with dissolved components such as glucose, proteins in and exhibits as Newtonian nature; and the cellular elements - erythrocytes also known as red blood cells (RBCs), leukocytes also known as white

blood cells (WBCs) and platelets - suspended in the plasma that make the whole blood not only a suspension but also exhibits as non-Newtonian nature [48, 50, 71–74]. The plasma approximately comprises 55% of the blood volume [72] with the components such as ions, enzymes and other proteins dissolved in. The rest of the blood volume is the cellular elements - predominately RBCs - which comprise approximately 45%. RBCs comprise 97% of the cellular element volume [72] and the volume percentage of the RBCs in the whole blood is approximately 42% in women and 45% in men [75], this phenomenon is called hematocrit. The density of the blood is varies from 1040 to 1060  $kg/m^3$  [72]. Within this study, the density of the blood is taken as 1060  $kg/m^3$ .

Flowing through the living organs, namely vessels, with living cells, plasma and dissolved components in the plasma, the blood has various functions from *transportations* oxygen - by means of RBCs -, nutrients and wastes throughout the body, *regulations* of osmotic pressure and pH to *protections* against the infections by means of the WBCs and in due course of injury, formation of thrombus that prevents blood loss, by means of platelets.

RBCs are the most numerous cellular elements in the blood. They are significantly specialized comparing to the other cells that own neither the cell nucleus nor mitochondria, herewith, they possess enormously space for hemoglobin proteins which are responsible for transporting oxygen to the cells and carrying carbon dioxide back to the lungs flowing through the vessels as well as responsible for the characteristic of red color of the blood. Without any nucleus inside and with owning a discoidal biconcave shape, in spite of their thicknesses are approximately  $2\mu m$  (micrometre) and diameters are around  $8\mu m$ , RBCs achieve to carry the oxygen by squeezing throughout the smallest capillaries with the diameters of less than  $6\mu m$  [72]. This squeezing behavior of RBCs within the small capillaries effects the viscosity characteristic of the blood. In capillaries, the viscosity of the blood decreases due to the significantly small diameter less than 0.3mm, by the reason of RBCs move in the fast axial stream while plasma moves in the slow marginal stream, hereat, the velocity of RBCs becomes greater than the velocity of plasma and this phenomenon is called Fåhræus–Lindqvist effect [76]. Also, the non-Newtonian nature of blood shows itself particularly at low shear rates.

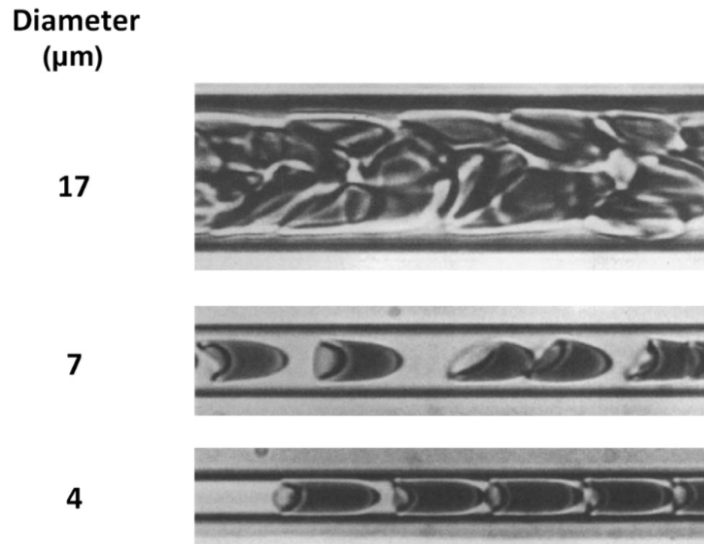


**Figure 2.1** : RBCs flowing within glass tubes for three different diameters [77]. This figure is a modification of [78].

Since the viscosity of the blood is associated with the rheology, blood exhibits as non-Newtonian within the capillaries that had been demonstrated by the experiment of Fåhræus and Lindqvist [76] with regard to the viscosity of the blood within capillary tubes. In 1966, Chien et al. [79] demonstrated that in the whole blood, there is no linear relation between the shear stress and the shear rate. They observed non-Newtonian behavior in the whole blood with normal hematocrit. In 1972, Thurston [80] demonstrated that the blood has not only non-Newtonian behavior but also has viscoelastic nature. In 1979, Thurston [50] investigated the rheological parameters of the blood with regards to viscosity, viscoelasticity and thixotropy.

Non-Newtonian, shear-thinning, viscoelastic nature of the whole blood arise from the cellular elements, predominantly RBCs - which have a remarkable effect on the blood viscosity in terms of rheology - in a Newtonian liquid, plasma [72, 74]. Moreover, the blood is pumped by the heart periodically with a wave-like motion which this phenomenon is called pulsatile flow. Considering all these features, modeling blood flow is a challenging problem, particularly, in the abnormal geometries such as image-based patient-specific cerebral aneurysms.

The blood is pumped by the heart through the arteries with a heart rate, range from 60 to 100 beats per minute (bpm). The pumping behavior of the heart creates pulsatile conditions within the arteries. The heart has systole and diastole periods, which means the heart pumps the blood during systole while rests during the diastole period. The

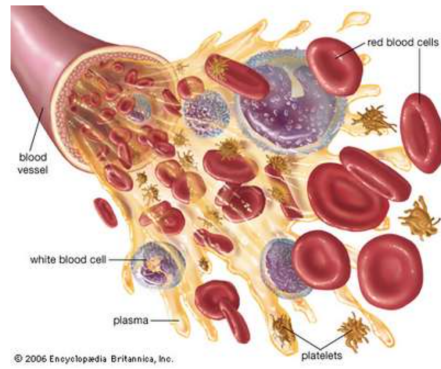


**Figure 2.2** : Cellular elements of the blood (2006 Encyclopaedia Britannica, Inc.).

arteries and capillaries have a sophisticated branching system, thus, the blood could be distributed to each part of the body. The vessels of the blood are living organs, hence, they could adjust to and behave according to the varying hemodynamic conditions by enlarging or shrinking behaviors [74]. Basically, there are three types of blood vessels: *arteries* distribute the blood pumped by the heart to the organs in order to supply nutrients and oxygen, *capillaries* which are the smallest blood vessels, transport the products by means of osmotic gradient, and *veins* carry carbon dioxide and waste back to the lungs. The arteries and veins comprise of three layers. The internal lumen layer is called *tunica intima*, which is the thinnest layer and consists of endothelial cells. The middle layer, thickest layer in arteries, is called *tunica media* which consists of smooth muscle cells, collagen and elastic fiber. The external layer is *tunica adventitia*, consists of predominantly loose connective tissue with some smooth muscle cells. This external layer also includes nerves and vasa vasorum in large vessels (See Figure 2.3).

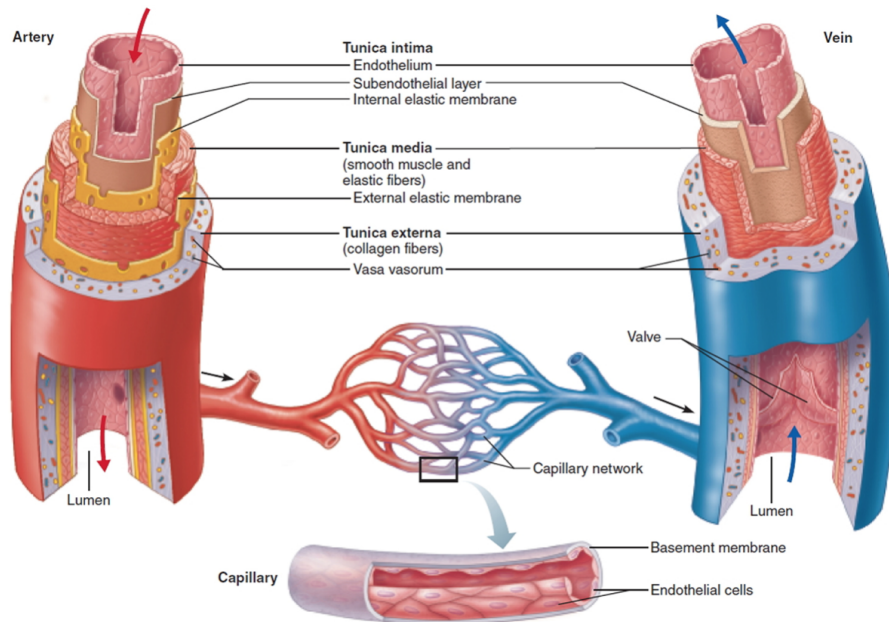


**Figure 2.3 :** Layers of artery, vein and capillary [81].

### 2.3 Cerebral Aneurysms

The blood vessels are living organs, hence, under physical conditions they react to the stimuli. In order to respond to the abnormal hemodynamic effects, the vessel walls could synthesize molecules or re-model the vessel walls. Basically, aneurysms are the pathologic, re-modeled, abnormal structures of the blood vessel walls. Aneurysms could be categorized in terms of their locations such as coronary artery aneurysms are localized at the heart while cerebral aneurysms are localized at the brain. In terms of their shape, aneurysms could be classified into two main types: *fusiform* and *saccular*. Fusiform aneurysms with their spindle shapes are mostly localized in the abdominal aorta while berrylike-shaped saccular aneurysms are usually localized in the brain area, most particularly, in the CoW. Withal, there are two fundamental types of saccular aneurysms: *side – wall*, also known as *lateral* and *terminal*, also known as *bifurcation*. A major of the intracranial aneurysms are the saccular aneurysms which are localized apex of bifurcation arteries and on the side-wall of the curved arteries [82].

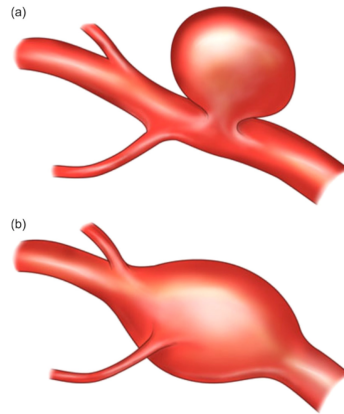


**Figure 2.4** : Aneurysm types in terms of their shapes. Saccular aneurysm on the top (a) and fusiform aneurysm on the bottom (b) by Campo-Deano et al. [67].

Cerebral aneurysms arise from the weakness of the cerebral artery, in particular, under abnormal hemodynamic conditions that cause to pathologic dilations of the cerebral artery walls that commonly localized in the CoW [8, 16–18, 82].

Basically, there are three steps with regards to cerebral aneurysms: *formation*, *growth*, and eventually *rupture*, respectively [19, 20]. The reasons underlying formation, growth and rupture steps of the intracranial aneurysms might be some risk factors such as hypertension, high alcohol consumption, smoking, heredity and so forth [4, 23]. These reasons might change the homeostasis and cause to result some problems such as high blood pressure. These abnormal conditions might cause to change the hemodynamic factors of the CoW and as a consequence intracranial aneurysms might occur. Moreover, destabilizing conditions cause to lead not only aneurysms but also atherosclerosis (See Figure 2.6) within CoW.

The rupture of an aneurysm cause to bleed within subarachnoid space and this phenomenon is called SAH. Considering bleeding is a serious problem, high rates of mortality and morbidity are occurred due to the SAH [8–10]. The prevalence of the intracranial aneurysms are quite common in population [1, 3].

The CoW is supplied 80% by the two carotid arteries and approximately 20% by the basilar artery. The anterior zone of the CoW is supplied by the two carotid arteries and more than 85% of the cerebral aneurysms occur in this zone [17]. Particularly, cerebral aneurysms could be found in the arteries of ACoA, PCoA, MCA, ICA, BA with high percentages as seen in Figure 2.7.



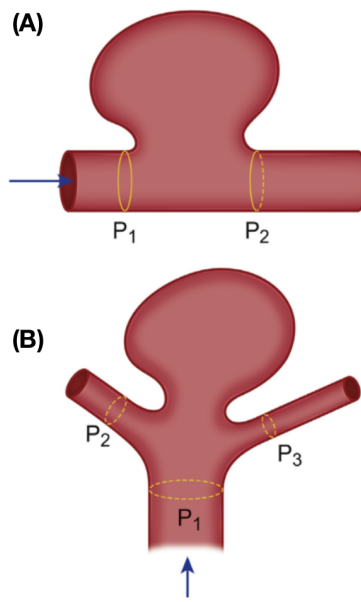


**Figure 2.5** : (A) shows side-wall aneurysm with  $P_1$  afferent vessel and  $P_2$  efferent vessel while (B) shows terminal aneurysm with  $P_1$  afferent vessel and  $P_2, P_3$  efferent vessels by Munarriz et. al [21].

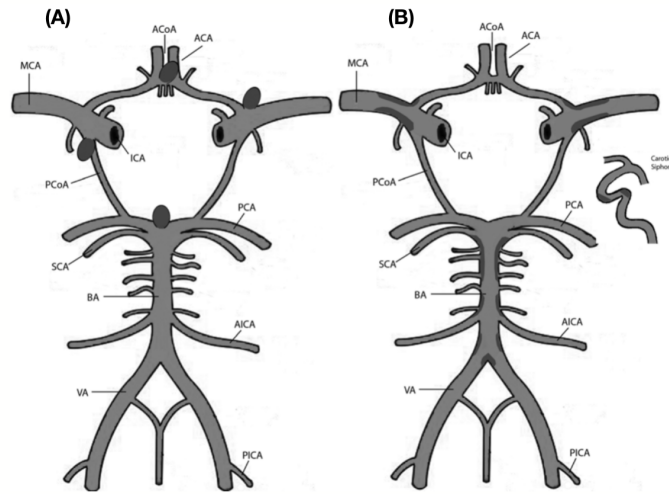


**Figure 2.6** : The figure shows both aneurysm and atherosclerosis in the CoW. Locations in CoW could be summarized as follows: ACA (Anterior Cerebral Artery), ACoA (Anterior Communicating Artery), AICA (Anterior Inferior Cerebellar Artery), BA (Basilar Artery), ICA (Internal Carotid Artery), MCA (Middle Cerebral Artery), PCA (Posterior Cerebral Artery), PCoA (Posterior Communicating Artery), PICA (Posterior Inferior Cerebellar Artery), SCA (Superior Cerebellar Artery), VA (Vertebral Artery). Darker color in (A) indicates saccular aneurysms, while indicates atherosclerosis in (B) by Nixon et al. [83].

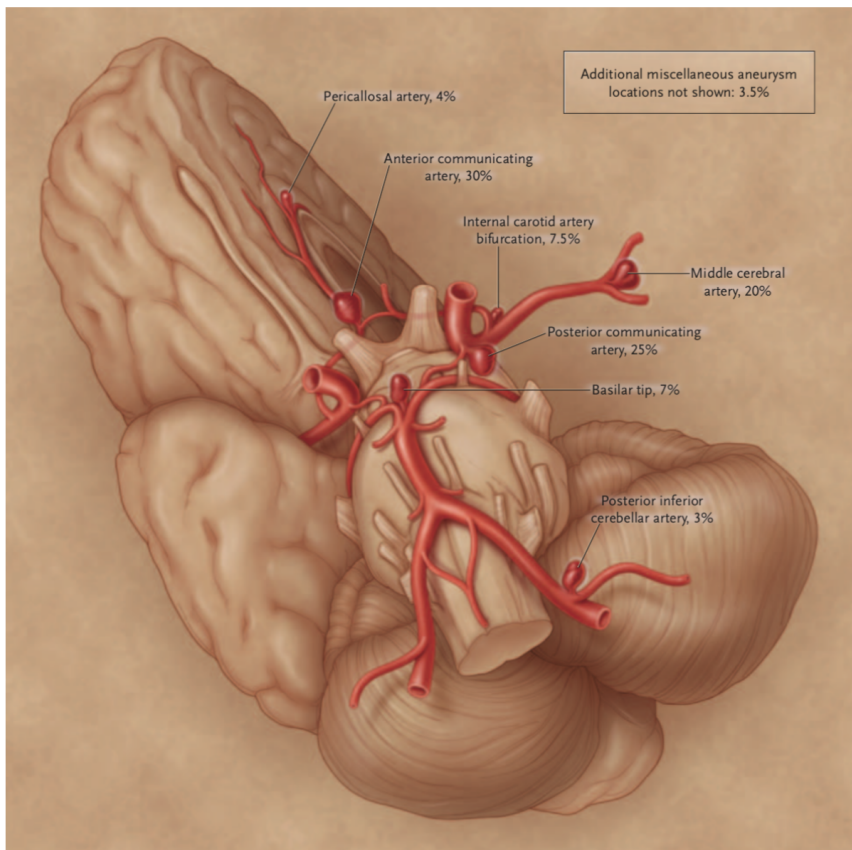


**Figure 2.7** : The arteries and the corresponding aneurysms with their prevalences in the CoW by Brisman et al. [2].

### **3. MATHEMATICAL MODELING OF BLOOD FLOW**

#### **3.1 Purpose**

Cerebral aneurysms are rather common considering the world population [1–5]. The rupture of an aneurysm might cause to serious disability problems for the patient or when thinking the worst-case scenario, might cause to death of the patient [2, 6, 7, 9, 10, 12]. Consequently, it is remarkably crucial to predict the rupture risk of the cerebral aneurysms. Unfortunately, the prediction of the rupture risk only by means of in-vivo techniques is not sufficient. It has been demonstrated that the analysis of the rupture status by means of CFD techniques and numerical simulations are getting more reliable and with the increasing technology of imaging techniques and CFD, the researchers have been extensively examined the rupture status of the intracranial aneurysms [19, 29, 30, 34]. Hence, there is a vast scale of need for imaging methods, computational techniques and mathematical models to analyze the rupture status of the cerebral aneurysms.

As mentioned comprehensively in *Chapter 2*, the blood exhibits a shear-thinning non-Newtonian fluid owing to the cells such as RBCs suspended in the plasma which exhibits a Newtonian fluid [72]. Since the blood is a viscoelastic, shear-thinning, non-Newtonian fluid, the mathematical modeling of this liquid becomes a challenging problem. Taking into account all of these reasons, the purpose of this section is to express the blood flow within patient-specific cerebral aneurysms from the point of view of the mathematical modeling.

#### **3.2 The Governing Equations**

Considering the fluid is isothermal, the governing equations - also known as the Navier-Stokes equations - are the conservation of mass and momentum and could be described mathematically for a time-dependent incompressible fluid as follows:

$$\frac{\partial \rho}{\partial t} + \nabla \cdot (\rho \mathbf{u}) = 0 \quad (3.1)$$

and

$$\rho \left( \frac{\partial \mathbf{u}}{\partial t} + \mathbf{u} \cdot \nabla \mathbf{u} \right) = -\nabla p + \nabla \cdot \boldsymbol{\tau} + \rho G \quad (3.2)$$

where  $\rho$  is the fluid density,  $\mathbf{u}$  is the velocity vector field,  $t$  is the time,  $p$  is the pressure,  $\boldsymbol{\tau}$  is the stress tensor,  $\nabla$  is the nabla operator and  $G$  is the external field such as gravity.

Since  $\rho$  is constant for an incompressible fluid, the conservation of mass equation which is the equation of (3.1) might be simplified as follows:

$$\nabla \cdot \mathbf{u} = 0 \quad (3.3)$$

For a compressible fluid  $\nabla \cdot \mathbf{u} \neq 0$  while for an incompressible fluid  $\nabla \cdot \mathbf{u} = 0$ .

The conservation of momentum equation which is (3.2) has a stress tensor  $\boldsymbol{\tau}$  which could be described mathematically as follows:

$$\boldsymbol{\tau} = 2\mu \boldsymbol{\varepsilon} \quad (3.4)$$

for a better understanding, the term  $\boldsymbol{\varepsilon}$  is:

$$\boldsymbol{\varepsilon} = (\nabla \mathbf{u} + \nabla \mathbf{u}^T)/2 \quad (3.5)$$

where  $\boldsymbol{\tau}$  is the stress tensor and  $\mathbf{u}$  is the velocity vector field as expressed before,  $\mu$  is the dynamic viscosity,  $\boldsymbol{\varepsilon}$  is the strain rate tensor - also known as rate of deformation tensor - and  $\mathbf{u}^T$  is the transpose of the velocity vector. Considering the equations above, stress tensor could be re-written as follows:

$$\boldsymbol{\tau} = 2\mu(\nabla \mathbf{u} + \nabla \mathbf{u}^T)/2 = \mu(\nabla \mathbf{u} + \nabla \mathbf{u}^T) \quad (3.6)$$

Thus, the divergence of the stress tensor is:

$$\nabla \cdot \boldsymbol{\tau} = \mu \nabla^2 \mathbf{u} \quad (3.7)$$

Since  $\nabla^2 F = \nabla \cdot \nabla F = \Delta F$ , the conservation of momentum equation could be written for a time-dependent incompressible Newtonian fluid as:

$$\rho \left( \frac{\partial \mathbf{u}}{\partial t} + \mathbf{u} \cdot \nabla \mathbf{u} \right) = -\nabla p + \mu \Delta \mathbf{u} + \rho G \quad (3.8)$$

When taken into account the blood flow as a non-Newtonian fluid, the dynamic viscosity term  $\mu$  ought to be written as a function, depends on the shear rate term  $\dot{\gamma}$  which looks like  $\implies \mu(\dot{\gamma})$ . Within this study, Carreau-Yasuda viscosity model has been performed in terms of non-Newtonian nature of the blood. Considering this model, the conservation of momentum equation could be re-written for a time-dependent viscous shear-thinning non-Newtonian fluid as follows:

$$\rho \left( \frac{\partial \mathbf{u}}{\partial t} + \mathbf{u} \cdot \nabla \mathbf{u} \right) = -\nabla p + \mu(\dot{\gamma}) \Delta \mathbf{u} + \rho G \quad (3.9)$$

where  $\mu(\dot{\gamma})$  could be written for Carreau-Yasuda model as:

$$\mu(\dot{\gamma}) = \mu_\infty + (\mu_0 - \mu_\infty) [1 + (\lambda \dot{\gamma})^a]^{\frac{(n-1)}{a}}. \quad (3.10)$$

where  $\lambda$  is the time constant,  $n$  is the power constant,  $a$  is the parameter used to fit experimental data.

The shear rate term  $\dot{\gamma}$ , which is a scalar measure of the strain rate tensor, could be expressed mathematically as follows:

$$\dot{\gamma} = \sqrt{2tr(\boldsymbol{\varepsilon}^2)}. \quad (3.11)$$

### 3.3 Rheology of Blood

Rheology is a specific study apropos of fluid mechanics and dynamics. Substantially, the word of "rheology" connotes the non-Newtonian and viscoelastic fluids [49]. Since this *Chapter* is related to mathematical modeling of blood flow and the study of rheology is a very comprehensive area as well as a complex phenomenon, in this section, it will be examined primary differences amidst Newtonian and various non-Newtonian fluids with their mathematical expressions.

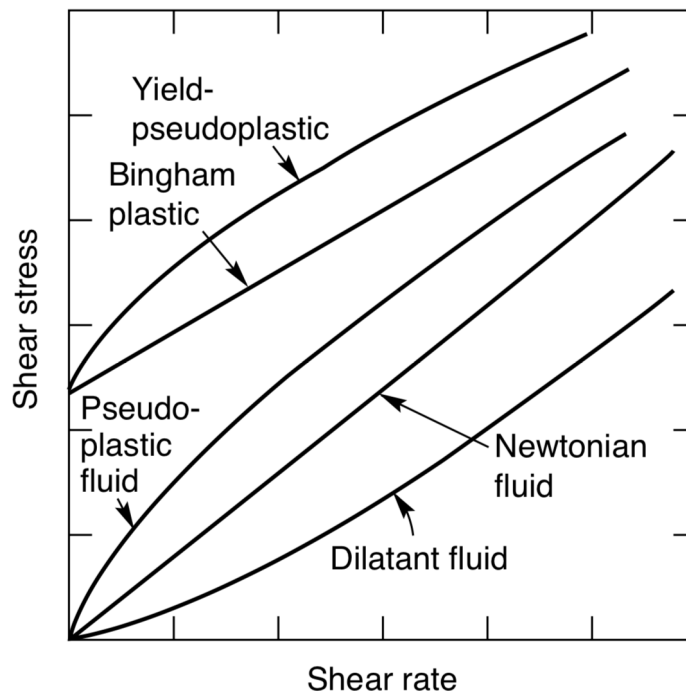


**Figure 3.1 :** Rheology diagram of the flow behaviors [84].

The main difference between a Newtonian and a non-Newtonian fluid is the dynamic viscosity  $\mu$  which is constant and independent from the shear rate  $\dot{\gamma}$  in a Newtonian fluid while it is a function depends on the shear rate as  $\mu(\dot{\gamma})$  in a non-Newtonian fluid.

Essentially, the blood consists of the liquid solution of plasma with proteins - which exhibits as a Newtonian behavior - and cellular elements such as erythrocytes, leukocytes and platelets suspended in the plasma that make this liquid a suspension [48, 50, 71–73]. The non-Newtonian nature of whole blood arise from the cellular elements, particularly, from erythrocytes - also known as RBCs which have a significant effect on blood viscosity [72,73,85]. Although non-Newtonian effects could be neglected in large arteries such as aorta due to the large shear rates, the whole blood exhibits shear-thinning nature at low shear rates as well as in capillaries and small arteries less than 1 mm [72] and these shear-thinning effects ought to be taken into account in order to perform the blood flow modeling under the accurate assumptions particularly in capillaries.

Thus far, blood has been described in multifarious ways taking the advantage of various non-Newtonian models in a major of the CFD studies by researchers (See Table 3.1).

Since, non-Newtonian nature of the whole blood is associated with the shear stress and rate, it could be described mathematically in the general formula as follows:

$$\mu(\dot{\gamma}) = \mu_{\infty} + (\mu_0 - \mu_{\infty})F(\dot{\gamma}) \quad (3.12)$$

where  $\mu_0$  and  $\mu_{\infty}$  are the asymptotic viscosities at zero and infinity shear rates respectively,

$$\mu_0 = \lim_{\dot{\gamma} \rightarrow 0} \mu(\dot{\gamma}), \mu_{\infty} = \lim_{\dot{\gamma} \rightarrow \infty} \mu(\dot{\gamma})$$

and  $F(\dot{\gamma})$  is the shear dependent function such that,

$$\lim_{\dot{\gamma} \rightarrow 0} F(\dot{\gamma}) = 1, \lim_{\dot{\gamma} \rightarrow \infty} F(\dot{\gamma}) = 0. \quad (3.13)$$

Hence, at the point of varying  $F(\dot{\gamma})$  function as shear-thinning characteristic addresses different non-Newtonian models of the blood flow (See Table 3.1).

In order to model blood flow with its shear-thinning nature, a variety of viscosity models have been used by the researchers. The viscosity model has a strong effect on the hemodynamic results [5]. Therefore, it is crucial to choose an accurate and realistic viscosity model that harmonize with the experimental blood viscosity. The Herschel-Bulkley viscosity model harmonize experimental blood viscosity at middle and high shear rates while at low shear rates this model is not realistic to model blood flow with its shear-thinning nature. On the other side, another viscosity model, Power-Law, represents a linear relation between viscosity and shear rate and this characteristic is disharmonious with experimental blood viscosity. Carreau-Yasuda viscosity model is more realistic and accurate model with its parameter used to fit experimental data,  $a$ .

In this current study, Carreau-Yasuda viscosity model is implemented in order to perform CFD simulations to express non-Newtonian shear-thinning flow behavior of the whole blood within image-based patient specific intracranial aneurysms. This viscosity model has been extensively used in a wide range of studies in order to model blood flow with shear-thinning characteristic of the fluid [86, 87, 90–92].

**Table 3.1** : Some non-Newtonian viscosity models for blood flow. The parameters are the time constant  $\lambda$ , power constant  $n$ , parameter used to fit experimental data  $a$ , model constant  $k$  and yield stress  $\tau_0$ .

Model Name	Constitutive Equation	Parameters
<i>Carreau</i>	$\mu(\dot{\gamma}) = \mu_\infty + (\mu_0 - \mu_\infty)[1 + (\lambda \dot{\gamma})^2]^{\frac{n-1}{2}}$	$\lambda = 3.313s$ $n = 0.3568$ $\mu_0 = 0.56poise$ $\mu_\infty = 0.0345poise$ <i>Cho et al.</i> 1991 [86]
<i>Carreau – Yasuda</i>	$\mu(\dot{\gamma}) = \mu_\infty + (\mu_0 - \mu_\infty)[1 + (\lambda \dot{\gamma})^a]^{\frac{(n-1)}{a}}$	$\lambda = 0.110s$ $n = 0.392$ $\mu_0 = 22 \times 10^{-3} Pa s$ $\mu_\infty = 2.2 \times 10^{-3} Pa s$ $a = 0.644$ <i>Gijsen et al.</i> 1999 [87]
<i>Cross</i>	$\mu(\dot{\gamma}) = \mu_\infty + (\mu_0 - \mu_\infty)/(1 + (\lambda \dot{\gamma})^n)$	$\lambda = 1.007s$ $n = 1.028$ $\mu_0 = 0.56poise$ $\mu_\infty = 0.0345poise$ <i>Cho et al.</i> 1991 [86]
<i>Herschel – Bulkley</i>	$\mu(\dot{\gamma}) = k(\dot{\gamma})^{n-1} + (\tau_0/\dot{\gamma})$	$k = 8.9721 \times 10^{-3} Ns^n/m^2$ $n = 0.8601$ $\tau_0 = 0.0175N/m^2$ <i>Valencia et al.</i> 2008 [88]
<i>Power – Law</i>	$\mu(\dot{\gamma}) = k(\dot{\gamma})^{n-1}$	$k = 14.67 \times 10^{-3} Ns^n/m^2$ $n = 0.7755$ <i>Molla et al.</i> 2012 [89]





**Figure 3.2** : The turbulence regime sketches by Leonardo da Vinci (Nature).

### 3.4 Blood as a Turbulent Flow

In principle, there are two fundamental regimes of the motion of fluids, laminar flow which is smooth and has no disruptions or eddies and turbulent flow which is a complex phenomenon with chaotic behavior and contrary to laminar flow, it has disruptions, eddies and significant fluctuation rates.

The turbulence regime of fluids has been aroused curiosity among the artists and scientists from far in the past. Leonardo da Vinci studied fluid mechanics and drew sketches of turbulent flows (See Figure 3.2). However, the major study of turbulent flow had been performed by Osborne Reynolds, a British scientist and mathematician in the 19th century [93]. He observed the fluid motion regime changes with the ratio of internal forces to viscous forces and this dimensionless ratio is called *Reynolds number*,  $Re$  described mathematically as:

$$Re = \frac{\rho U D}{\mu} \quad (3.14)$$

where  $U$  is the mean velocity of the fluid ( $m/s$ ) in a pipe and  $D$  is the characteristic diameter ( $m$ ) of the pipe. Since there is a relation among dynamic viscosity  $\mu$ , fluid density  $\rho$  and kinematic viscosity  $\nu$  such that  $\nu = \mu/\rho$ , the Reynolds equation could be re-written as follows:

$$Re = \frac{U D}{\nu}. \quad (3.15)$$

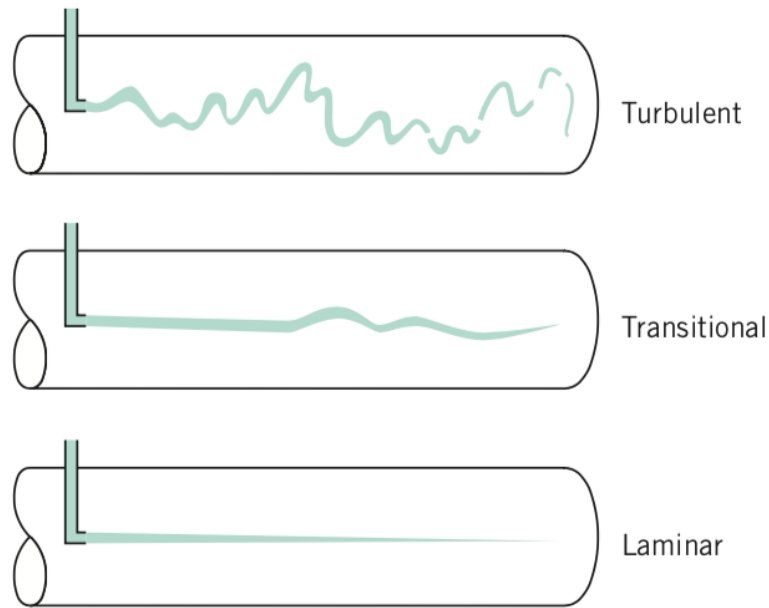


**Figure 3.3** : From laminar to turbulent flow [94].

The characteristic of the fluid motion regime could be identified according to *Reynolds number*  $Re$ . The flow is laminar if the  $Re$  is less than approximately 2100 while turbulent regime could be observed if the  $Re$  is greater than approximately 4000 [94]. The numbers between these two cases, the flow regime might change between laminar and turbulent which is called transitional flow [94].

Blood flow is generally modeled with laminar regime among the scientists. However, considering abnormal formations in the blood vessels such as atherosclerosis and aneurysms, the blood flow acts in a particular manner of chaotic and complex regimes. In 1972, Roach et al. [95] performed a study about bifurcations localized in CoW, and observed turbulent flow at  $Re = 1200$  under steady conditions and also they observed lowest  $Re$  with a value of less than 500 in the aneurysm bifurcation.

In order to perform turbulence simulations, there are three major methods which are called Reynolds Averaged Navier Stokes (RANS), Large Eddy Simulation (LES) and Direct Numerical Simulation (DNS). Since RANS model is based on time averaging, this model is less accurate and less expensive than LES and DNS. DNS model solves the flow field directly using Navier Stokes equations without modeling and time averaging, hence, this makes DNS the most accurate method in order to model flow with turbulence nature. However, DNS model requires very fine grids comparing to RANS and LES and also requires large computational resources. When considered from these aspects, DNS model is not only expensive but also time-consuming. LES

model has advantages and disadvantages comparing to RANS and DNS. Although it is less expensive and less time-consuming, it is less accurate than DNS. In spite of requiring finer grids, time and more computational resources, it is more accurate than RANS. Essentially LES model is based on spatial filtering system. It solves the flow field larger than the filter size directly with Navier Stokes equations and models the rest of flow scales smaller than the filter. Considering the filter size approaches to zero, the solution approaches to DNS model.

Within the current study, considering the abnormal geometries of the patient specific cerebral aneurysm data, the blood flow is modeled with the nature of turbulent flow regime as well as unsteady and pulsatile flow. The turbulence model used in this study is *dynamic k equation model*, namely, dynamic one equation subgrid-scale model for Large Eddy Simulation (LES) within OpenFOAM [96].

As mentioned before, LES method is based on a filtering system. The mathematical equation [97] could be written as follows:

$$\bar{f}(x) = \int G(x-x')f(x')dx' \quad (3.16)$$

where  $f(x)$  includes all the scales that defined and  $G(x)$  is the filter function. The filtered governing equations for LES [98] could be written as follows:

$$\frac{\partial \bar{u}_i}{\partial x_i} = 0 \quad (3.17)$$

the equation 3.17 is the continuity equation for LES and,

$$\frac{\partial \bar{u}_i}{\partial t} + \frac{\partial (\bar{u}_i \bar{u}_j)}{\partial x_j} = -\frac{1}{\rho} \frac{\partial \bar{p}}{\partial x_i} + \frac{\partial}{\partial x_j} (-\tau_{ij} + 2\nu \bar{\epsilon}_{ij}) \quad (3.18)$$

the equation 3.18 is the momentum equation for LES. The term  $\nu$  indicates kinematic viscosity. Grid-scale strain rate tensor could be written [98]:

$$\bar{\epsilon}_{ij} = \frac{1}{2} \left( \frac{\partial \bar{u}_i}{\partial x_j} + \frac{\partial \bar{u}_j}{\partial x_i} \right) \quad (3.19)$$

and subgrid scale stress could be written [98]:

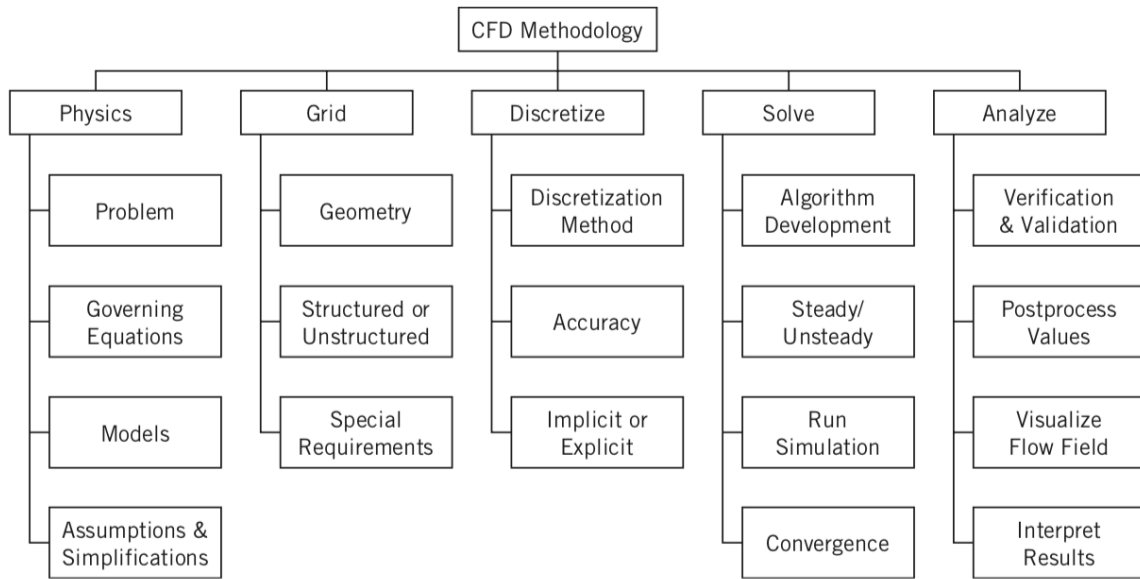


**Figure 3.4 :** CFD methodology flowchart [94].

$$\tau_{ij} = \overline{u_i u_j} - \overline{u_i} \overline{u_j}. \quad (3.20)$$

### 3.5 Numerical Discretization

Numerical techniques and methods based on computers provides an opportunity for the scientists to solve a wide range of computational problems. With an increasing technology of high-performance-computing, it has become possible to solve partial differential equations (PDEs) related to fluid problems using CFD, which is a branch of fluid mechanics, with numerical approaches. This process requires replacing the partial differential equations with discretized algebraic equations which approach to the PDEs [94]. CFD process involves various complex phenomenon from governing equations, model assumptions to discretization techniques, developing algorithms, post-processing and visualizations (See Figure 3.4) thus, this process has to be performed precisely.

The most known discretization techniques are Finite Difference Method (FDM), Finite Element Method (FEM) and Finite Volume Method (FVM), respectively. Within this study, FVM is implemented to obtain approximate numerical solutions for Navier-Stokes equations and PDEs for CFD calculations.

## 4. MATERIALS AND METHODS

CFD methodology is a very comprehensive process due to the combination of the various areas such as physics and fluid mechanics. CFD analysis process generally consists of three stages: 1) *Pre – processing* stage involves preparing the geometry for the CFD simulations such as adding flow extensions and generating mesh for the geometry; 2) *Processing* stage involves numerical techniques and CFD simulations which they are usually performed by means of high-performance-computing; 3) *Post – processing* stage involves extracting the needed flow properties and visualizing the data after applying the numerical methods. Taking account of all these stages listed, it is very crucial to perform each step precisely in order to analyze CFD results accurately. Within this *Chapter*, each step will be discussed extensively from the very beginning of the aneurysm data before *pre – processing* to the end of the scientific visualizations, and the process between them with the materials used such as mesh generator, CFD software and the methods used such as FVM.

### 4.1 Cerebral Aneurysm Data

Cerebral aneurysms are related to high morbidity and mortality rate as mentioned before in the previous *Chapters*. More particularly, the rupture of an intracranial aneurysm might lead to SAH which is the most serious problem of the cerebral aneurysms. Consequently, it is remarkably essential to study the rupture status of the cerebral aneurysms for diagnosis and treatment. With the increasing technology of the CFD and imaging techniques, it has become possible to examine blood flow simulations that is unfeasible to perform using in-vivo techniques in clinical practice.

In order to investigate the rupture status of intracranial aneurysms by means of modeling blood flow and simulations using CFD techniques within an artificial balloon-like geometry might cause to misleading results and interpretations. To overcome this issue, it is significantly crucial to use patient-specific cerebral aneurysm

geometries instead of artificial straight pipe geometries with the balloon-shaped structures.

The researches based-on patient-specific cerebral aneurysm geometries in terms of CFD simulations require image data. However, there are limited image data in the online platforms to perform scientific experiments. In order to provide an opportunity to perform experiments using patient-specific cerebral aneurysm data in terms of better understanding of the cerebral aneurysms, *The Aneurisk Project* [99] shares the data in a downloadable form via the online platform.

The image-based patient-specific cerebral aneurysm data set of *The Aneurisk Project* [99] are DICOM images acquired from 3D rotational angiographies and the cerebral aneurysm model geometries are ready for the simulations of the blood flow dynamics after reconstruction, characterization and segmentation process.

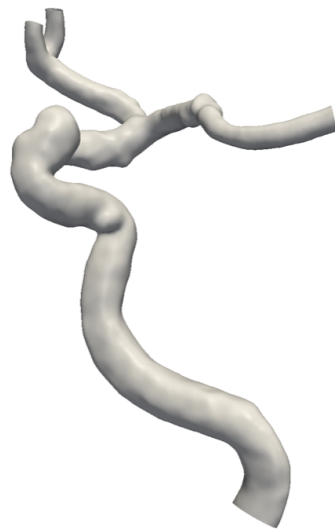
The repository of the project comprises various cerebral aneurysm models in terms of the aneurysm location such as ICA, MCA, the rupture status and the aneurysm type such as terminal or side-wall. Use of the data in the AneuriskWeb repository has been authorized by the Ethical Committee of the Ca' Granda Niguarda Hospital.

In order to investigate the effects of the hemodynamic factors with non-Newtonian and turbulent flow characteristics on the rupture status of the intracranial aneurysms, the CFD calculations have been performed within the data from *The Aneurisk Project* repository: one ruptured aneurysm located on ICA, named as  $R - ICA$  and one unruptured aneurysm located on ICA, named as  $U - ICA$  (See Figures 4.1 and 4.2).

Both models are the side-wall type ICA geometries with the saccular aneurysms. The original geometries have been clipped in order to examine the region of interest which is close to the aneurysm zone and added flow extensions in order to have accurate inflow and outflow boundaries.

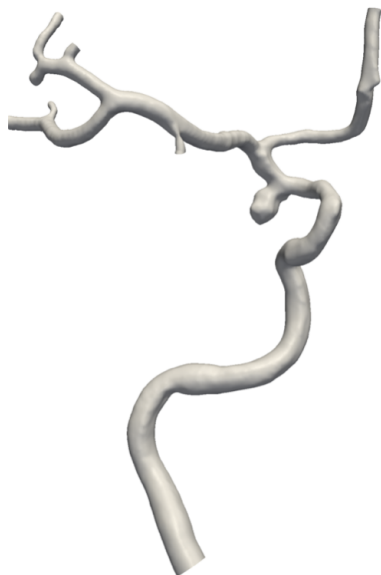
## **4.2 Cerebral Aneurysm Data Preparation for CFD Processing**

The patient-specific data-set in the Aneurisk repository have various aneurysm types and models. The original stereolithography (STL) geometries used in this current study have been clipped in order to focus on the region of interest which is around the aneurysm zone by using the VMTK [63] software. Using the same software,



**Artery Location in CoW** : Internal Carotid Artery (ICA)  
**Image Data** : 3D Rotational Angiography  
**Rupture Status** : Unruptured Aneurysm  
**Patient Sex** : Female  
**Patient Age** : 48  
**Aneurysm Type** : Side-Wall Aneurysm  
**Aneurysm Shape** : Saccular Aneurysm  
**Model Name** : U-ICA

**Figure 4.1** : Original geometry image represents  $U - ICA$  model from the AneuriskWeb repository.



**Artery Location in CoW** : Internal Carotid Artery (ICA)  
**Image Data** : 3D Rotational Angiography  
**Rupture Status** : Ruptured Aneurysm  
**Patient Sex** : Female  
**Patient Age** : 26  
**Aneurysm Type** : Side-Wall Aneurysm  
**Aneurysm Shape** : Saccular Aneurysm  
**Model Name** : R-ICA

**Figure 4.2** : Original geometry image represents  $R - ICA$  model from the AneuriskWeb repository.

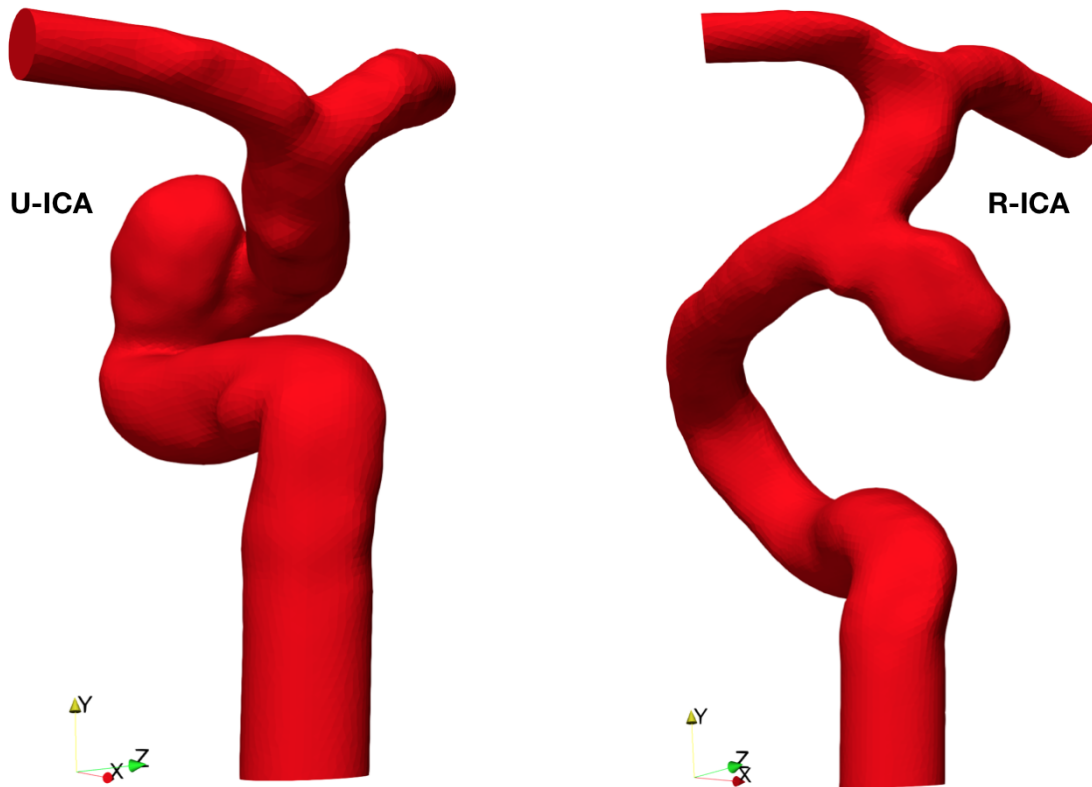


**Figure 4.3** : The STL geometry images after clipping, adding flow extensions, closing the gaps and scaling applied to the original STL data.

after clipping process, the flow extensions have been added to each extremity of the surface to have cylindrical prolongations in order to have accurate inflow and outflow boundaries. In order to generate a volume mesh, the gaps corresponding to the inlet and outlet boundaries have been closed by using VMTK. Since in this thesis, the blood flow simulations within patient-specific cerebral aneurysm geometries have been performed by means of OpenFOAM (Open-source Field Operation And Manipulation) software [96], an opensource C++ toolbox for CFD which performs calculations within the geometries for dimensions in terms of meter (m), the length of the geometries of the original data have been scaled to meter by using OpenFOAM [96] software (See Figure 4.3).

Subsequent to the treatments within the original STL data by means of VMTK [63], the modified STL data are ready for the mesh generation in order to perform 3D blood flow simulations using OpenFOAM [96] software with FVM. For the purpose of generating both triangular surface meshes and tetrahedral volume meshes from the 3D surface geometries in order to perform grid convergence index (GCI) method, an open-source mesh generator software Netgen [100] has been used within this thesis



(Netgen Version 6.2.1803). It has been generated a wide range of tetrahedral elements from approximately 400.000 to 3.500.000 in order to perform the discretization error analysis by means of GCI (See Figure 4.4). In the furtherance of generating triangular surface meshes and tetrahedral volume meshes from the 3D surface geometries - which are  $R - ICA$  geometry and  $U - ICA$  geometry - for the CFD simulations in terms of non-Newtonian shear-thinning Carreau-Yasuda model cases and non-Newtonian shear-thinning Carreau-Yasuda with large eddy simulation (LES) turbulence flow model cases, octree mesh method has been used for the mesh generations by means of ICEM CFD 19.2 (ANSYS, Inc., Canonsburg, PA, USA). Since LES model requires finer grids as discussed before within *Chapter 3*, it has been used 595129 elements for Carreau-Yasuda (CY) model case and 1048397 for CY with LES turbulence blood flow model case for the  $U - ICA$  geometry while  $R - ICA$  geometry has 522295 elements for CY blood flow model case and 1050456 elements for CY with LES turbulence blood flow model case - these meshes have been generated by means of ICEM CFD 19.2 (ANSYS, Inc., Canonsburg, PA, USA). Post-processing and visualization applications have been performed using an open-source software, ParaView [101].

### **4.3 Numerical Methods for CFD Processing**

CFD methods have been extensively performed with the increasing technology of high-performance-computing in order to examine blood flow modeling within patient-specific geometries. Also, in the current study, it has been taken the advantages of these promising techniques as well as open-source softwares such as OpenFOAM [96] and ParaView [101].

OpenFOAM is a finite volume-based open-source C++ toolbox for CFD calculations by means of solving the PDEs, most particularly, in order to examine fluid dynamics. OpenFOAM also provides *pre - processing* and *post - processing* utilities such as blockMesh and paraFoam besides the solvers that solve PDEs. Since OpenFOAM is an open-source software, it could be easily customized with regards to demands of the specific problems.

OpenFOAM uses FVM which is a numerical method putting the PDEs into discretized algebraic equations which approach to the PDEs over finite volumes. With a basis of FVM, OpenFOAM provides ready solvers for the specific problems. Within this thesis,

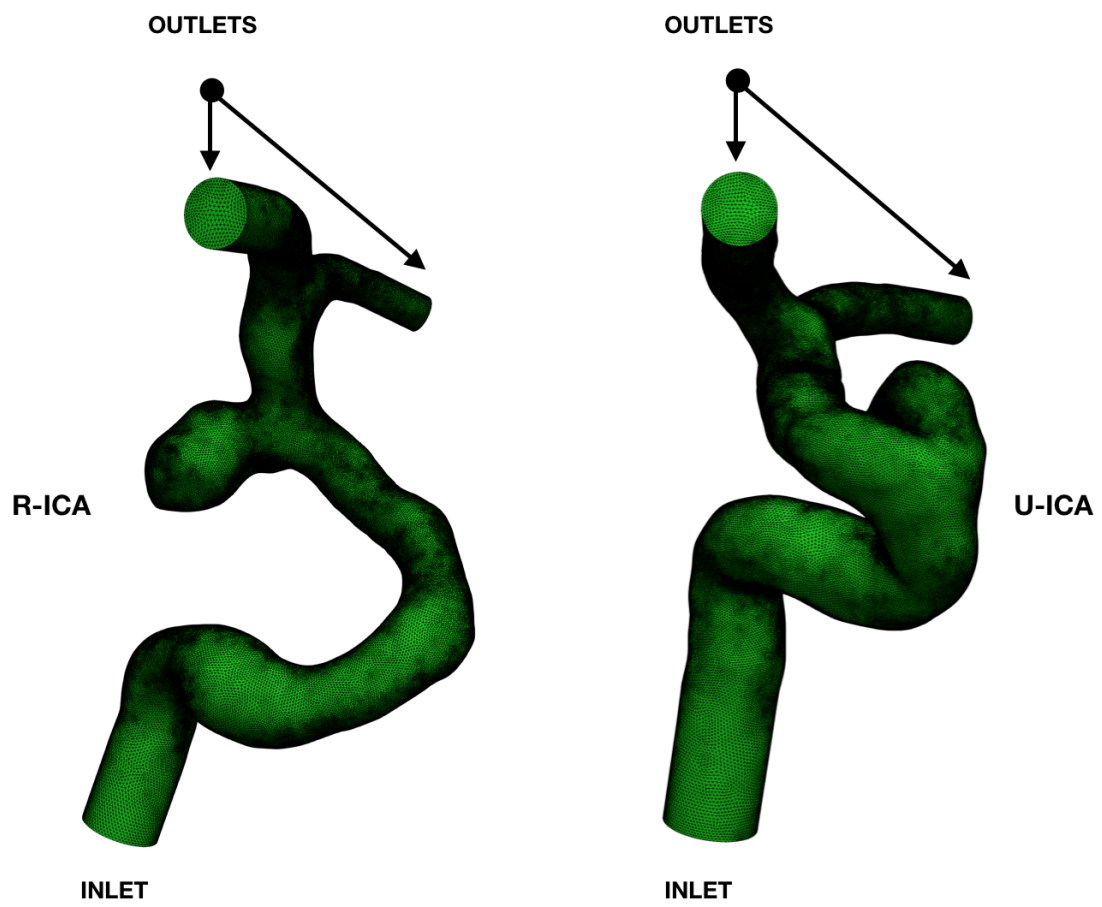


**Figure 4.4** : Mesh generations have been performed using Netgen [100].

it has been taken the advantage of *pisoFoam* solver for unsteady incompressible flow. The solver of *pisoFoam* uses the PISO (Pressure-Implicit with Splitting of Operators) algorithm behind in order to solve Navier-Stokes equations. In the current study, both non-Newtonian Carreau-Yasuda and non-Newtonian Carreau-Yasuda with turbulence effects blood flow simulations had been performed by means of *pisoFoam* solver within OpenFOAM.

In the current study, the non-Newtonian Carreau-Yasuda with turbulence effects simulations had been performed in order to examine the unsteady pulsatile flow behavior in complex 3D patient-specific cerebral aneurysm geometries with LES which is a mathematical method for turbulence in CFD. Within OpenFOAM, there are various LES models such as Smagorinsky and Dynamic k-equation. Within this thesis, it had been taken the advantage of *dynamicKEqn* also known as dynamic one equation eddy-viscosity for LES subgrid-scale (SGS) model by using OpenFOAM. Subsequent to the CFD simulations, ParaView [101] software had been used for the visualizations.

#### **4.4 Hemodynamic Indices for Post Processing Analyzes**

Hemodynamic indices are the parameters which provide particular indicators for morphological and functional changes of arteries and veins. Subsequent to the CFD calculations, hemodynamic effects have been analyzed for the image-based patient-specific cerebral aneurysms. WSS has been calculated by means of the post processing utility which is *wallShearStress* within OpenFOAM software for all the simulations. Other hemodynamic indices could be calculated from WSS parameter. Within this current study, in order to observe hemodynamic effects on the patient-specific cerebral aneurysms, the hemodynamic parameters which are WSS, OSI, time-averaged WSS (TAWSS), spatial WSS gradient (SWSSG) and time-averaged SWSSG (TASWSSG) have been calculated within *U – ICA* and *R – ICA* geometries for both non-Newtonian shear-thinning Carreau-Yasuda (CY) model case and non-Newtonian shear-thinning CY with LES turbulence effects model case (CY + LES).

#### 4.4.1 Wall shear stress

WSS is the foremost parameter in terms of hemodynamic assessments and extensively examined within rupture status investigations of cerebral aneurysms by researchers [8, 19, 30, 54, 59, 62]. Basically, WSS  $\tau_w$  is a tangential force generated by blood flowing along vessel wall and could be described mathematically as follows:

$$\tau_w = \mu \left( \frac{\partial \mathbf{u}}{\partial y} \right) \Big|_{y=0} \quad (4.1)$$

where  $\tau_w$  is the WSS,  $\mu$  is dynamic viscosity,  $\mathbf{u}$  is the velocity along wall tangential direction,  $y$  is the distance to the wall.

In terms of rupture status investigation of the cerebral aneurysms, WSS parameter is significantly effective among the hemodynamic factors. Circulatory system consists of living elements - such as organs and cells - and these living structures react to the hemodynamic stimuli in order to protect the homeostasis by means of their reactions such as gene expression and vascular remodeling. Particularly, abnormal WSS conditions might lead to the vascular remodeling [102], hence, blood vessels might change their structures and with the weakening of the cerebral arteries, aneurysm might be occurred under these abnormal hemodynamic conditions. As discussed before within *Literature Review* section in *Chapter 1*, Meng et al. [19] proposed two types of aneurysms: small with thin-walled aneurysms which arise from high WSS effect and large with thick-walled aneurysms which arise from low WSS effect. Besides, Malek et al. [55] demonstrated that low shear stress areas might tend to have atherosclerosis. Since both low and high WSS have the abnormal effects on the blood vessels, they might lead to cause aneurysm growth and rupture. Moreover, abnormal WSS might cause endothelial cell degeneration and dysfunction.

#### 4.4.2 Oscillatory shear index

Oscillatory shear index (OSI) is the major parameter just like WSS in order to investigate rupture status of the cerebral aneurysms in terms of hemodynamic factors. OSI was proposed for the first time by Ku et al. [56] in 1985 with the following definition: "an index which describes the shear stress acting in directions other than

the direction of the temporal mean shear stress vector.". Subsequent to demonstration of the significant effects of OSI on rupture status of cerebral aneurysms, this parameter has been extensively used within CFD-based cerebral aneurysm studies in terms of hemodynamic factors [19, 30, 54]. OSI factor could be expressed mathematically as follows:

$$OSI = \frac{1}{2} \left\{ 1 - \left( \frac{\left| \int_0^T \tau_w dt \right|}{\int_0^T |\tau_w| dt} \right) \right\} \quad (4.2)$$

where  $\tau_w$  is WSS and  $T$  is the cardiac cycle time.

OSI is a non-dimensional parameter and its values vary from 0 to 0,5 where the value of 0 addresses that there is no cyclic variation ( $0^\circ$ ) of WSS vector while the value of 0,5 addresses that there is  $180^\circ$  deflection of WSS vector direction.

High OSI values might lead to vascular remodeling within blood vessels [103], therefore, this hemodynamic parameter is strongly associated with cerebral aneurysm growth and rupture. High OSI also might effect endothelial cell response and dysfunction. Furthermore, OSI parameter might be associated with plaque formation [104].

#### 4.4.3 Time averaged wall shear stress

Time averaged wall shear stress (TAWSS) is the classic time average of each WSS vector magnitude at the wall and could be described mathematically as follows:

$$TAWSS = \frac{1}{T} \int_0^T |\tau_w| dt \quad (4.3)$$

where  $\tau_w$  is the WSS vector and  $T$  is the cardiac cycle period.

TAWSS could provide an insight in order to observe the overall cardiac cycle averaged WSS at the cerebral aneurysm wall.

#### 4.4.4 Spatial wall shear stress gradient

One of the most analyzed hemodynamic index is the spatial WSS gradient (SWSSG) - the spatial derivative of WSS - in terms of hemodynamic effects within cerebral aneurysms. SWSSG could be expressed as follows:

$$SWSSG = \left[ \left( \left| \frac{\partial \tau_w}{\partial x} \right| \right)^2 + \left( \left| \frac{\partial \tau_w}{\partial y} \right| \right)^2 + \left( \left| \frac{\partial \tau_w}{\partial z} \right| \right)^2 \right]^{\frac{1}{2}} \quad (4.4)$$

The positive WSS gradient and high WSS might lead to small with thin-walled aneurysms according to Meng et al. [19]. The fluctuations and oscillations in SWSSG might be associated with cerebral aneurysm initiation and for this purpose Shimogonya et al. [105] proposed a new hemodynamic parameter which is called gradient oscillatory number (GON). Moreover, SWSSG might be effective on endothelial cells and remodeling, and consequently might be associated with aneurysm growth [106, 107]. Dilations and the weakening of the cerebral arteries might be occurred due to the SWSSG. This parameter has been also thought to be associated with gene expression. Furthermore, DePaola et al. [108] had been performed an experiment and observed within disturbed flow regions WSS was low and SWSSG was high. They [108] observed cell migration, and surmised that high SWSSG might lead to morphological changes for endothelial structures under disturbed flow areas.

#### 4.4.5 Time averaged spatial wall shear stress gradient

Time averaged spatial wall shear stress gradient (TASWSSG) could provide an insight for overall SWSSG in cardiac cycle averaged. This parameter could be expressed as follows:

$$TASWSSG = \frac{1}{T} \int_0^T (SWSSG) dt \quad (4.5)$$

where  $T$  is the cardiac cycle time and  $SWSSG$  is the spatial wall shear stress gradient.

## 5. NUMERICAL RESULTS

Cerebral aneurysms are sizably common in the worldwide population [1, 4]. With the increasing techniques and technologies of imaging, CFD and high performance computing, cerebral aneurysms have been examined extensively by means of computer based researches and it has been demonstrated that hemodynamics play a significant role in order to investigate intracranial aneurysm stages and status by using these promising techniques [19, 29, 30].

Similarly, in this study, it has been taken the advantages of these techniques and technologies. The effects of hemodynamic factors on the imaged-based patient-specific cerebral aneurysms have been examined by means of CFD and high-performance-computing. Furthermore, grid convergence index method has been implemented in order to estimate the discretization errors in the simulations.

The foremost hemodynamic factors analyzed in this study are *WSS*, a tangential force generated by blood flowing along vessel wall; and *OSI*, proposed by Ku et al. [56] with the purpose: “specifically to provide an index which describes the shear stress acting in directions other than the direction of the temporal mean shear stress vector.”. The other parameters analyzed in this study are time-averaged *WSS* (*TAWSS*), spatial *WSS* gradient (*SWSSG*), time-averaged *SWSSG* (*TASWSSG*), velocity and pressure. The hemodynamic parameters have been expressed mathematically within the section of *Hemodynamic Indices for Post Processing Analyzes* under *Chapter 4*.

### 5.1 Grid Convergence Index Method and Results

CFD techniques have become promising methods in terms of investigating the effects of the hemodynamic factors on the patient-specific cerebral aneurysms. However, the simulation results might be misleading if the grid resolution is not accurately fit in with the complex aneurysm geometry. To overcome this issue, there is a need for estimating the discretization errors in CFD studies. The error analysis studies have been performed extensively in CFD researches [109–111], hence, also within this

**Table 5.1** : Different maximum velocity values  $f_i$  corresponding to different number of elements  $N_i$ . The values are obtained from nearby outflow area.

i	$N_i$	$f_i$
(1)	3.335.224	2.27708
(2)	2.036.136	2.27704
(3)	1.482.896	2.24064

thesis, grid convergence index method based on generalized Richardson Extrapolation has been performed in order to estimate the discretization errors.

GCI method requires CFD simulations within a geometry for at least three different grid sizes in terms of refinement; coarse-grid, moderate-grid, fine-grid, respectively. The required steps could be written as follows:

(1) Defining refinement ratio, ( $r$ ); in a majority of the studies, refinement ratio  $r$  between 3 grids is set to 2 and the meshes are generated according to this constant number. However, in a number of studies [112],  $r$  is defined by means of the element numbers with the following formula:

$$r = \frac{1}{2} \left[ \left( \frac{N_1}{N_2} \right)^{1/3} + \left( \frac{N_2}{N_3} \right)^{1/3} \right] \quad (5.1)$$

where  $N_1$ ,  $N_2$  and  $N_3$  are the number of elements of the grids; fine, moderate and coarse, respectively. In this study, refinement ratio is defined with the Equation 5.1 [112].

(2) Determining a parameter indicating the grid convergence related to the study. In the current study, this parameter is the maximum velocity which has been calculated after the simulations, along the center line of the cross section whereabouts nearby the outlet boundary at the peak systolic time (See Figure 5.1). The Womersley velocity inlet profile [113] used within the GCI analysis could be seen in the Figure 5.2.

The parameter of the maximum velocity has been calculated for five different element sizes from the coarsest to the finest 416.903, 803.976, 1.482.896, 2.036.136, 3.335.224 cells respectively and GCI has been performed for the five of them. However, only the finest three grids have been taken into account since obtaining more reasonable GCI values between the grids, as seen in the Figure 5.3. The parameter of the maximum velocity has been assigned as  $f_1$  for the fine,  $f_2$  for the moderate and  $f_3$  for the coarse grid as seen in the Table 5.1.



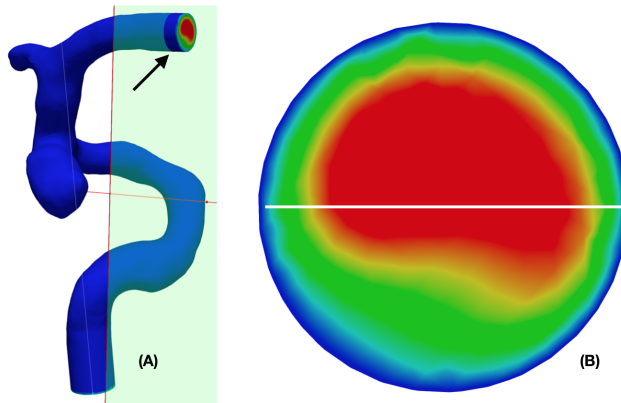


**Figure 5.1** : The cross section, nearby the outlet boundary (A). The line onto the cross section indicates where maximum velocity has been calculated along (B).

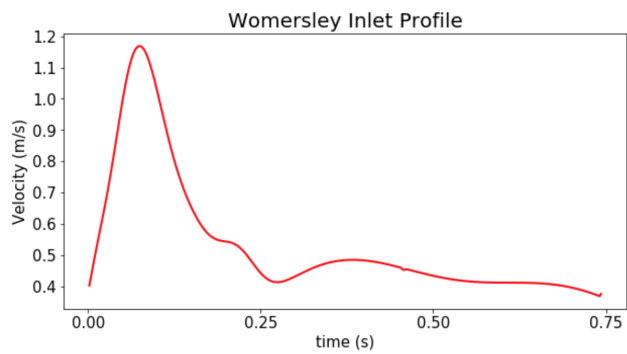


**Figure 5.2** : Womersley Inlet profile used in GCI analysis.

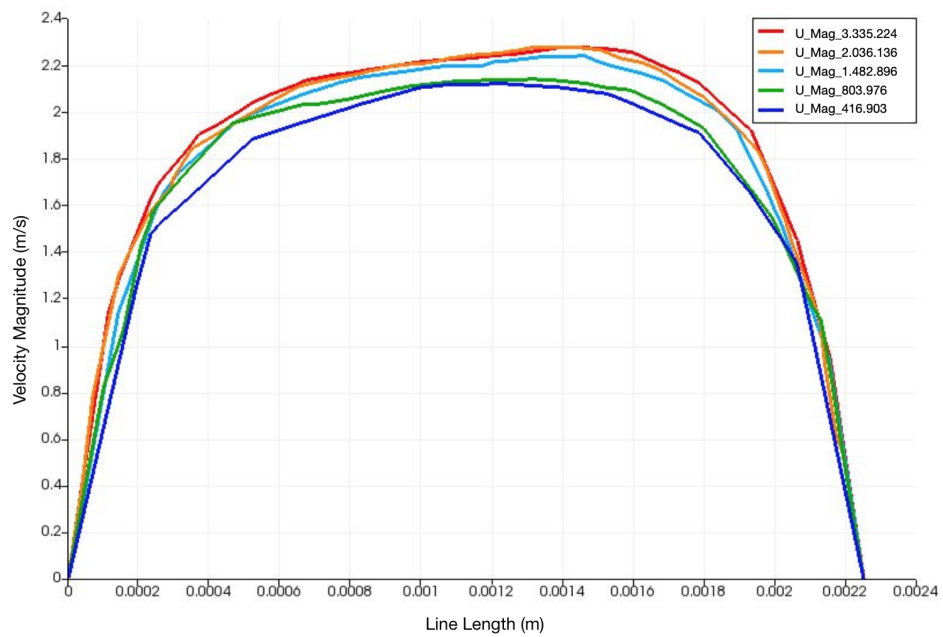


**Figure 5.3** : Velocity magnitude values on the line of the cross section nearby the outflow area for the 5 different grids in terms of cell numbers. Axis x indicates the length of the line and axis y indicates velocity magnitude.

**Table 5.2** : GCI method parameters and corresponding values regarding to the nearby outflow area.

Parameter	Value
$GCI_{1,2}$	2.4156156371658483e-06 %
$GCI_{2,3}$	0.0021982488450303164 %
$f_{ex}$	2.27708
<i>Control – Value</i>	1.0000176

(3) Calculating order of convergence,  $p$  with the following equation:

$$p = \ln \left( \frac{f_3 - f_2}{f_2 - f_1} \right) \frac{1}{\ln(r)} \quad (5.2)$$

(4) Performing Richardson Extrapolation method in order to obtain extrapolated solution by means of fine and moderate grids with the following formula:

$$f_{ex} = f_1 + \frac{f_1 - f_2}{r^p - 1} \quad (5.3)$$

where  $f_{ex}$  is the extrapolated solution,  $r$  is the refinement ratio and  $p$  is the order of convergence.

(5) Calculating GCI (%) between the grids with the following equations:

$$GCI_{2,3} = F_s \times \left| \frac{f_2 - f_3}{f_2} \right| \times \frac{1}{r^p - 1} \times 100 \quad (5.4)$$

$$GCI_{1,2} = F_s \times \left| \frac{f_1 - f_2}{f_1} \right| \times \frac{1}{r^p - 1} \times 100 \quad (5.5)$$

where  $F_s$  is the safety factor in order to have more accurate error estimations. In the current study, this factor is set to 1.25, same as the wide range of grid convergence studies.

(6) Validating the asymptotic range of convergence. In order to be in the range of the asymptotic convergence, following equation ought to be approximately equal to one:

$$\text{Control – Value} = \frac{GCI_{2,3}}{r^p \times GCI_{1,2}} \approx 1 \quad (5.6)$$

The results obtained from the GCI method applied nearby the outflow area could be seen in Table 5.2.  $GCI_{2,3}$  value is the discretization error difference between

**Table 5.3** : Different maximum velocity values  $f_i$  corresponding to different number of elements  $N_i$ . The values are obtained from nearby before aneurysm neck area.

i	$N_i$	$f_i$
(1)	3.335.224	2.68693
(2)	2.036.136	2.68528
(3)	1.482.896	2.67908

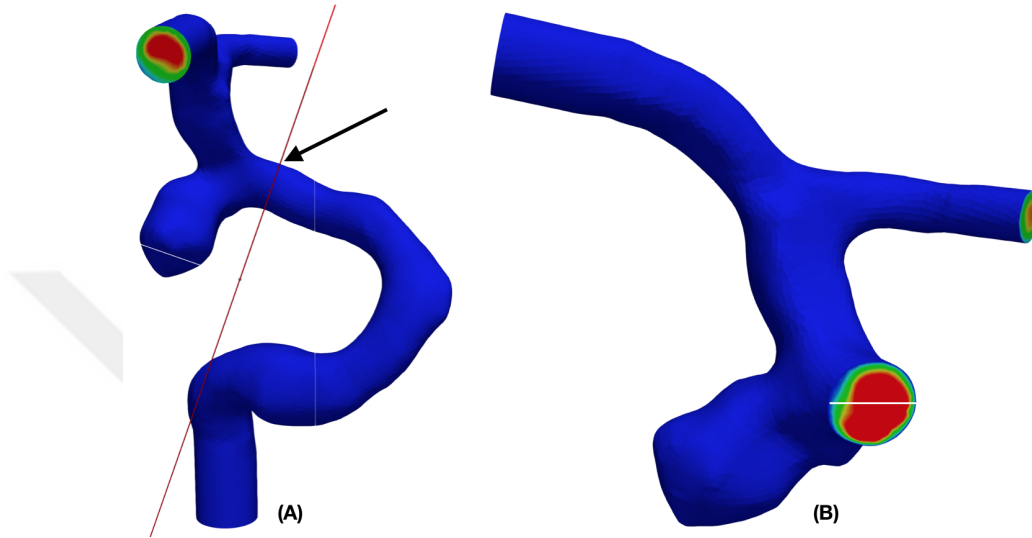


**Figure 5.4** : The arrow indicates the cross section, nearby before aneurysm neck area (A). The line onto the cross section indicates where maximum velocity has been calculated along (B).

*Grid* – 2 (moderate) and *Grid* – 3 (coarse). The results obtained from GCI indicate that there is only margin error of 0.0021982488450303164 %, which is significantly small, between the results obtained after simulations performed with moderate and coarse grids. Likewise, the value of  $GCI_{1,2}$  is the error difference between *Grid* – 1 (fine) and *Grid* – 2 (moderate). This value indicates that there is only margin error of 2.4156156371658483e-06 %, which is quite small that it might be negligible, between the results obtained after simulations performed with fine and moderate grids.

The value of  $f_{ex}$ , which is obtained by performing Richardson Extrapolation, is exactly the same with the calculated value of  $f_1$ . Furthermore, the calculated *Control* – *Value*, which is 1.0000176, demonstrates that GCI validates the asymptotic range of convergence.

Although applying GCI method by using maximum velocity values along the center line of the cross section whereabouts nearby the outlet flow area at peak systole provides high quality results, in order to ensure if the grid resolution is accurately fit in with the

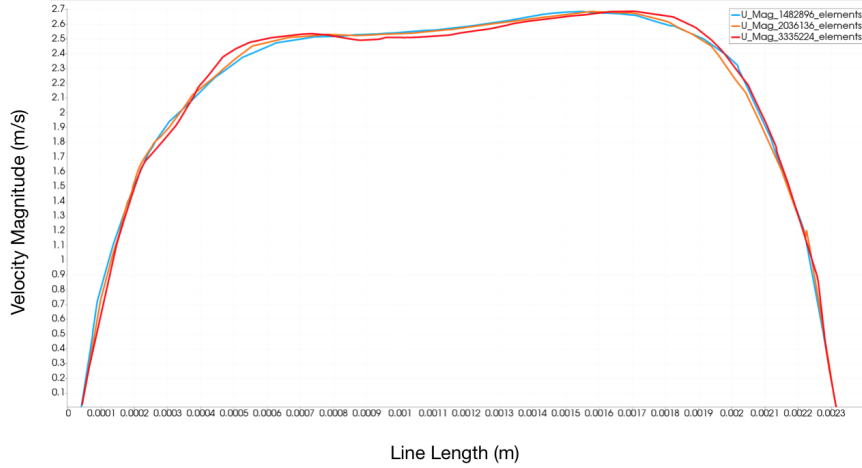


**Figure 5.5** : Velocity magnitude values on the line of the cross section nearby before aneurysm neck for the 3 different grids in terms of cell numbers. Axis x indicates the length of the line and axis y indicates velocity magnitude.

**Table 5.4** : GCI method parameters and corresponding values regarding to the area of before aneurysm neck.

Parameter	Value
$GCI_{1,2}$	0.027836213 %
$GCI_{2,3}$	0.10466095 %
$f_{ex}$	2.68752
Control – Value	1.000614

complex aneurysm geometry, another discretization error analysis has been performed by using the same determining parameter which is the maximum velocity, along the center line of the cross section whereabouts nearby the area of before aneurysm neck (See Figure 5.4). The same procedure regarding to GCI method has been repeated and obtained results could be seen in Table 5.4.

As seen from the Figure 5.5, for the three different element sizes, the velocity behaviors along the line onto the cross section nearby before aneurysm neck are almost the same.

The results obtained from the GCI method applied nearby before aneurysm neck area could be seen in Table 5.4.  $GCI_{2,3}$  value is the discretization error difference between *Grid – 2* (moderate) and *Grid – 3* (coarse). The results obtained from GCI indicate that there is only margin error of 0.10466095 %, which is in the acceptable range, between the results obtained after simulations performed with moderate and coarse grids. Likewise, the value of  $GCI_{1,2}$  is the error difference between *Grid – 1* (fine) and *Grid – 2* (moderate). This value indicates that there is only margin error of

0.027836213 %, which is quite small, between the results obtained after simulations performed with fine and moderate grids. The results obtained after applying GCI method before aneurysm neck area infer, although the values are higher from the GCI method applied for nearby outflow area, the three different grids provide approximately same results. Indeed, as expected, in the critical regions, mesh elements need smaller grids in order to fit in with the complex aneurysm geometries. Within this study the GCI results demonstrate that the three different grid elements give approximately the same results.

Additionally, the value of  $f_{ex}$ , which is obtained by performing Richardson Extrapolation for before aneurysm neck, is approximately the same with the calculated value of  $f_1$ . Furthermore, the calculated *Control – Value*, which is 1.000614, demonstrates that GCI validates the asymptotic range of convergence for before aneurysm neck area.

In order to analyze GCI, CFD simulations have been performed by means of OpenFOAM [96] (Version: v6), on the Amazon Elastic Compute Cloud (Amazon EC2), Amazon Web Services (AWS) [114, 115].

## 5.2 Patient-Specific Model Case Setups and Boundary Conditions

In order to investigate the rupture status within image-based patient-specific cerebral aneurysms in terms of hemodynamic factors, CFD simulations have been performed by using OpenFOAM [96] software. The patient-specific geometries have been provided from *Aneurisk Project* repository [99]. It has been investigated two internal carotid arteries; an unruptured internal carotid artery (ICA) which is named as  $U - ICA$  and a ruptured internal carotid artery (ICA) which is named as  $R - ICA$ . The blood flow has been modeled as unsteady, pulsatile, incompressible, non-Newtonian shear-thinning, with a density value of  $1060 \text{ kg/m}^3$  for both non-Newtonian and non-Newtonian with LES turbulence effects simulations. In order to investigate the non-Newtonian properties of blood, Carreau-Yasuda viscosity model has been used with the parameters from Gijssen et al. [87] as seen in the Table 5.5.

In order to ensure the stability, the CFD simulations with regards to  $U - ICA$  and  $R - ICA$  geometries, have been performed during 5 cardiac cycles with the time-step

**Table 5.5** : Parameters and corresponding values of Carreau-Yasuda viscosity model [87].

Parameter	Value
$\lambda$	0.110 s
$n$	0.392
$\mu_0$	$22 \times 10^{-3} \text{ Pa s}$
$\mu_\infty$	$2.2 \times 10^{-3} \text{ Pa s}$
$a$	0.644

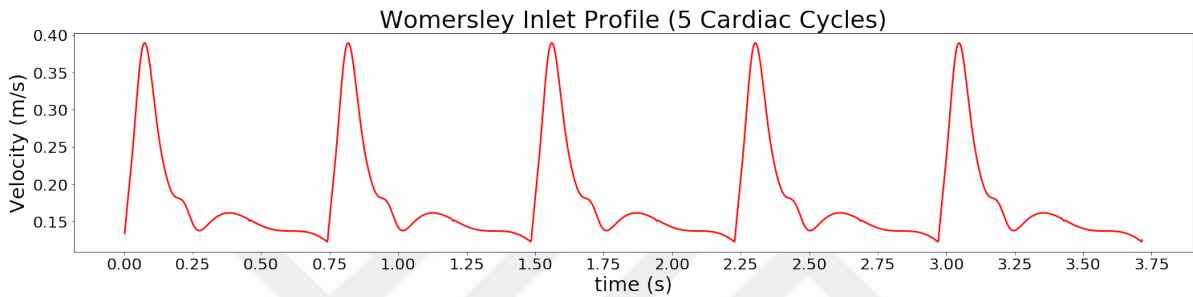


**Figure 5.6** : Womersley velocity profile during five cardiac cycles. One cardiac cycle takes 0,743 seconds to complete and five cardiac cycles last 3,715 seconds.

of  $10^{-5}$ . The simulation results have been compared and interpreted with regards to the last cardiac cycle which is fifth. Since the information with regards to the flow rates and velocities of the patient-specific geometries are not available in the *Aneurisk* repository, Womersley inlet profile has been taken from Piskin et al. [113] and modified according to cerebral aneurysms then modified Womersley inlet profile has been implemented to the  $U - ICA$  and  $R - ICA$  geometries. The Womersley inlet profile that implemented to both patient-specific cerebral aneurysm geometries could be seen in the Figure 5.6.

The CFD simulations within the patient-specific geometries of  $U - ICA$  and  $R - ICA$  have been performed for an unsteady laminar blood flow with non-Newtonian Carreau-Yasuda viscosity model and an unsteady mild turbulent flow with non-Newtonian Carreau-Yasuda viscosity model. The patient-specific cerebral aneurysm model cases could be seen in Figure 5.7. In order to simplify the case names, non-Newtonian Carreau-Yasuda blood flow model has been named as *shear – thinning model* and non-Newtonian Carreau-Yasuda mild turbulence blood flow model has been named as *turbulence flow model* within this thesis. Within tables and

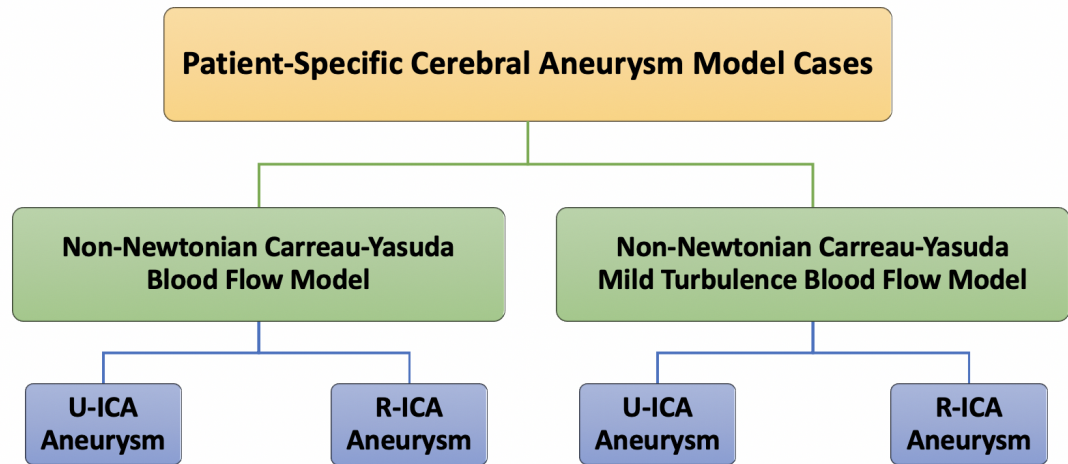


**Figure 5.7 :** Patient-specific cerebral aneurysm model cases.

figures, non-Newtonian Carreau-Yasuda blood flow model could be seen as CY while non-Newtonian Carreau-Yasuda mild turbulence blood flow model could be seen as CY + LES.

The *inlet* boundary conditions are Womersley inlet velocity profile while the outlet boundary conditions are Neumann boundary conditions for shear-thinning model simulations and turbulence flow model simulations in terms of velocity.

Due to the lack of the information with regards to the vascular wall thickness and elasticity of the patient-specific cerebral aneurysm geometries, the vascular walls have been modeled as rigid with no-slip boundary conditions for both shear-thinning model and turbulence flow model simulations.

In order to investigate the turbulence effects within cerebral aneurysm geometries, dynamic k equation model, namely, dynamic one-equation subgrid scale model for LES has been implemented.

The simulations have been carried out by using OpenFOAM (Version: v6) software [96] with pisoFoam solver based on PISO algorithm under FVM. ParaView software [101] has been used in order to visualize hemodynamic effects upon the imaged-based patient-specific cerebral aneurysms. WSS has been calculated by means of the *post – processing utility* of OpenFOAM. Since OpenFOAM uses  $\rho$ (density) – normalized WSS and pressure, the units are  $m^2/s^2$  within the corresponding plots.

It has been taken the advantage of high-performance-computing for CFD calculations. In the current study, the simulations had been carried out within the server system Saryer under UHeM (Ulusal Yüksek Başarımli Hesaplama Merkezi, English: National Center for High Performance Computing) [116].

### 5.3 Numerical Simulation Results for U-ICA

The unruptured cerebral aneurysm data localized in ICA has been investigated in order to examine the effects of hemodynamic factors such as WSS and OSI on the aneurysm. CFD simulations have been performed during five cardiac cycles to ensure the stability and the last cardiac cycle has been analyzed and visualized.

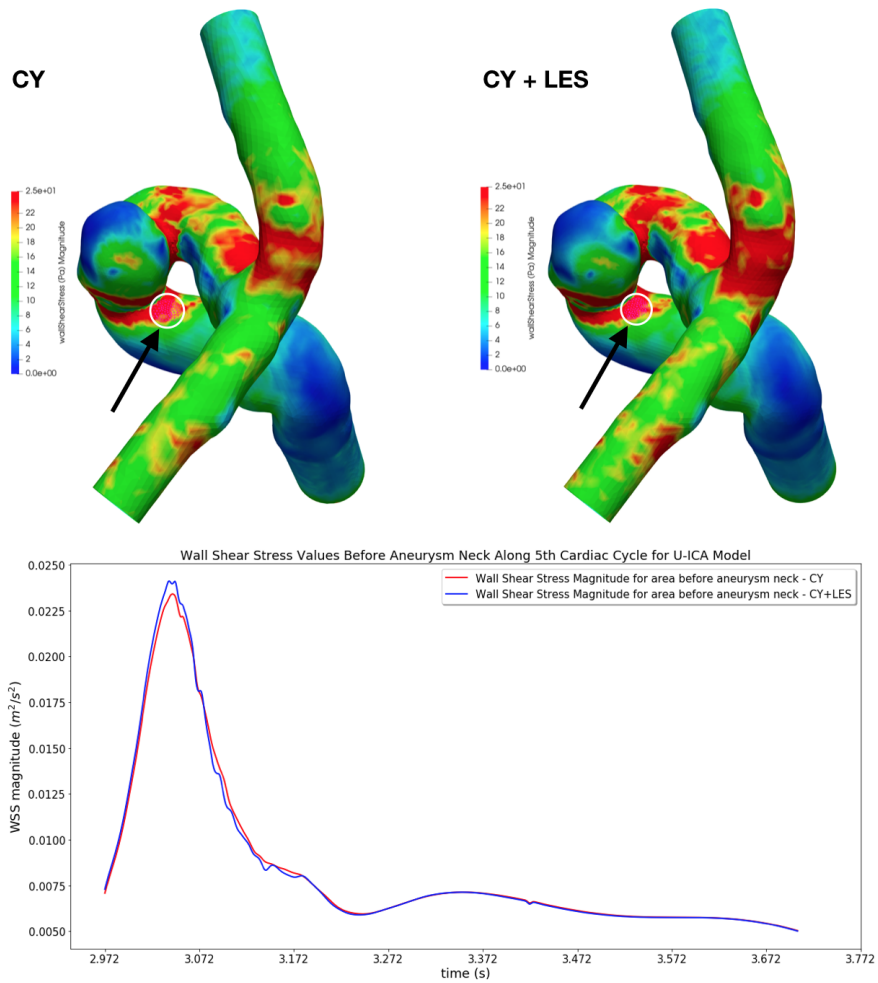
In order to investigate pressure and WSS behavior along the last cardiac cycle for shear-thinning Carreau-Yasuda (CY) model, one region has been selected on before aneurysm neck while another region has been selected after aneurysm neck. Moreover, two regions have been analyzed on aneurysm sac area in terms of WSS and pressure. Each region has been taken in the areas of high values of the parameters. Pressure and WSS have been analyzed for the same regions. Since OpenFOAM uses *density – normalized* WSS and pressure, the units are  $m^2/s^2$ .

Figure 5.8 represents WSS visualizations (top) and WSS plot (bottom) for CY and CY with LES models. As seen from the Figure 5.8, although CY with LES model has relatively high WSS values than the CY model, both cases have approximately same WSS values for the region of before aneurysm neck area within  $U - ICA$  geometry.

Figure 5.9 indicates WSS visualizations (top) and pressure plot (bottom) since both WSS and pressure have been analyzed for same areas. Pressure behavior for the region of before aneurysm neck area is almost the same for both CY model and CY with LES model within  $U - ICA$  geometry as seen from the Figure 5.9.

Velocity behavior has been analyzed by taking one cross section before aneurysm neck and the other cross section after aneurysm neck. Moreover, two more cross sections have been taken from aneurysm sac area. Within the slices, velocity profile has been observed for shear-thinning CY blood flow model and shear-thinning CY with LES turbulence flow model. Also, the streamlines have been visualized in order to observe





**Figure 5.8 :** WSS behavior has been observed during last cardiac cycle within  $U - ICA$  geometry for the selected region before aneurysm neck which is indicated with white circle. CY indicates Carreau-Yasuda viscosity model and LES indicates Large Eddy Simulation.

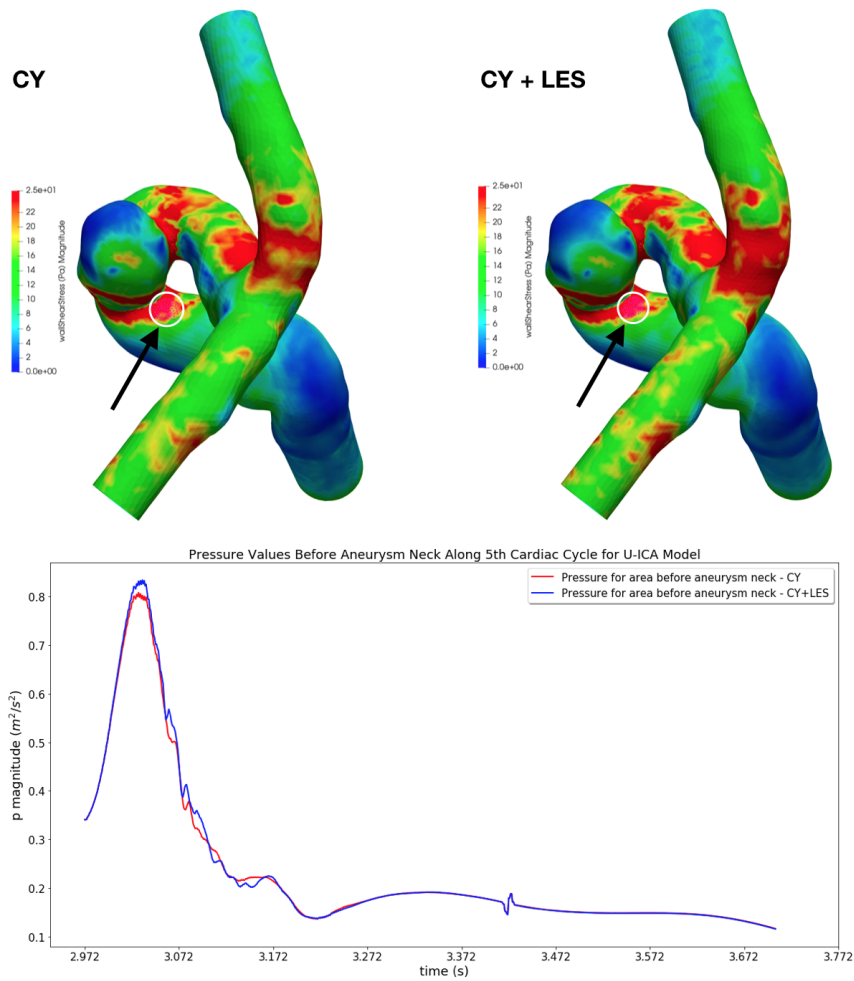


**Figure 5.9 :** Pressure behavior has been observed during last cardiac cycle within  $U - ICA$  geometry for the selected region before aneurysm neck which is indicated with white circle. CY indicates Carreau-Yasuda viscosity model and LES indicates Large Eddy Simulation.

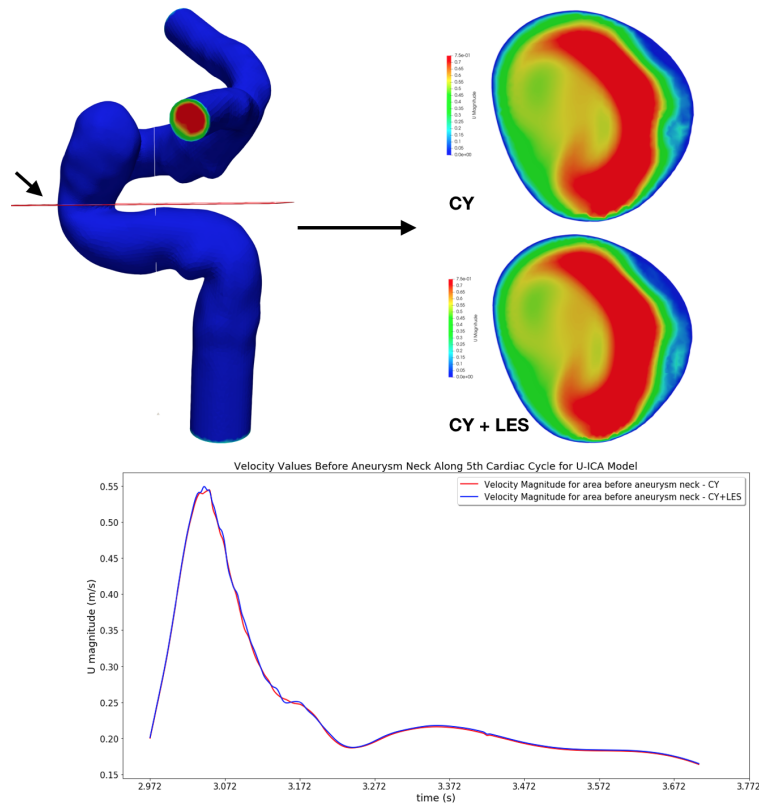
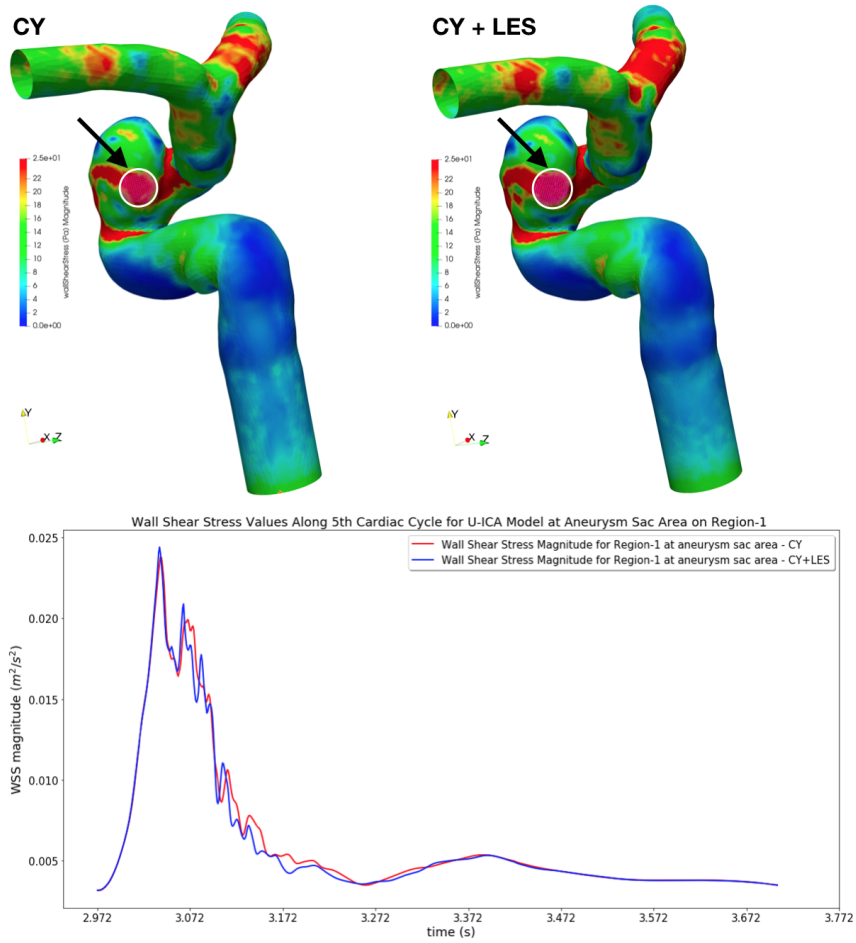


**Figure 5.10** : Velocity behavior has been observed during last cardiac cycle within  $U - ICA$  geometry for the whole slice before aneurysm neck. CY indicates shear-thinning Carreau-Yasuda viscosity model and LES indicates Large Eddy Simulation.

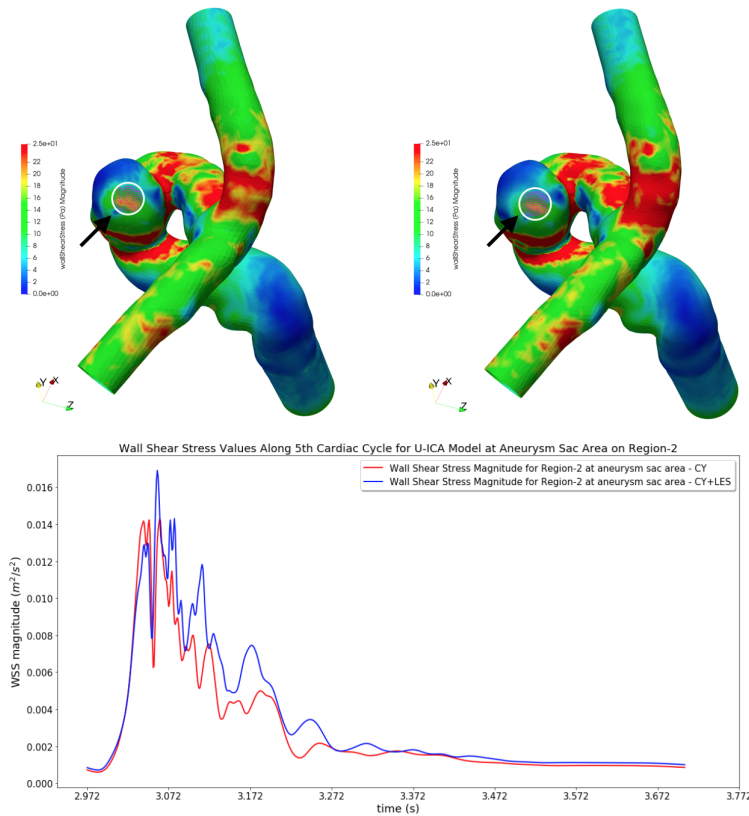
chaotic behavior of the flow within the aneurysm, particularly in the sac area, for shear-thinning CY and shear-thinning CY with LES turbulence blood flow models.

Figure 5.10 represents cross section regarding to before aneurysm neck area and corresponding slices for that cross section in terms of CY and CY with LES models (top) and velocity plot (bottom). As seen from the Figure 5.10, velocity behavior for both CY and CY with LES turbulence model within  $U - ICA$  geometry for the slice of before aneurysm neck area is almost the same.

Aneurysm sac area is the most critical region since it is the abnormal part of the cerebral artery. Therefore, in order to observe WSS and pressure behavior along the cardiac cycle, two regions have been selected with relatively high WSS area. The analyses have been performed on the exact same regions for WSS and pressure observations. Also, velocity behavior have been analyzed during the cardiac cycle within aneurysm sac for two slices.



**Figure 5.11** : WSS behavior has been observed during last cardiac cycle within  $U - ICA$  geometry for the region-1 on the aneurysm sac area which is indicated with white circle. CY indicates Carreau-Yasuda viscosity model and LES indicates Large Eddy Simulation.



**Figure 5.12** : WSS behavior has been observed during last cardiac cycle within  $U - ICA$  geometry for the region-2 on the aneurysm sac area which is indicated with white circle. CY indicates Carreau-Yasuda viscosity model and LES indicates Stress Large Eddy Simulation.

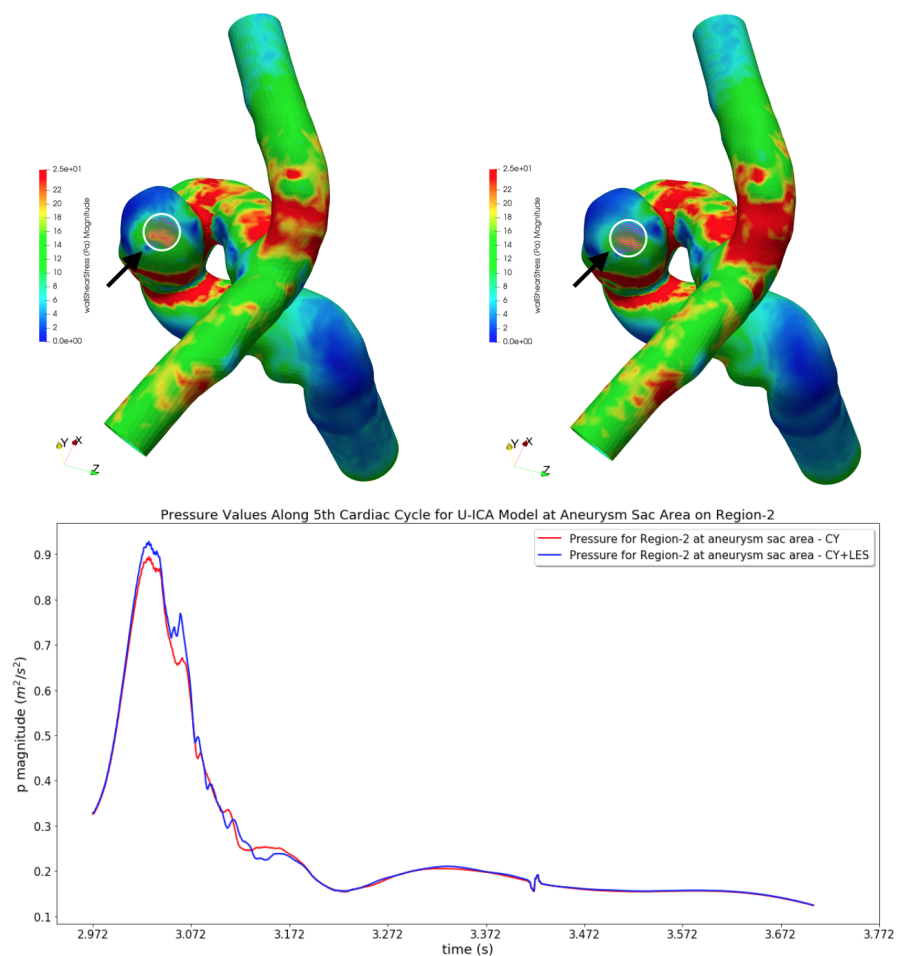
Figure represents WSS visualizations for CY and CY with LES models and selected regions with white circles in order to analyze WSS behavior for those regions and at the bottom of the figure WSS plot could be seen regarding to CY and CY with LES models. The Figure 5.11 shows that for both CY and CY with LES turbulence flow models, WSS exhibits almost the same within  $U - ICA$  geometry for first region of the aneurysm sac area.

As seen from the Figure 5.12, although CY with LES turbulence model has relatively high values of WSS, the values of WSS for CY and CY with LES model are close to each other within  $U - ICA$  geometry for second region of aneurysm sac area.

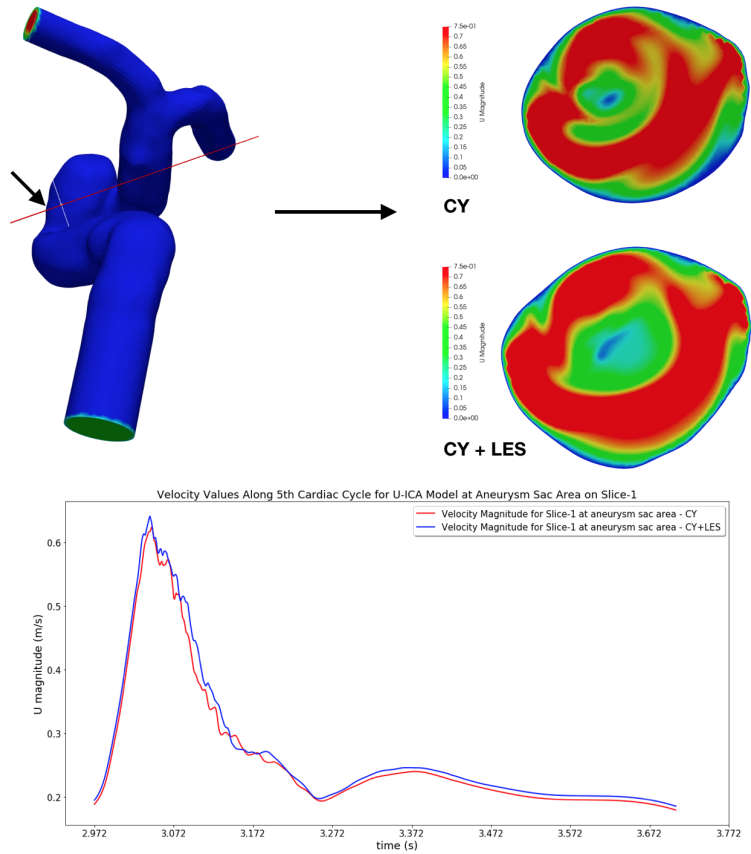
Although the values of pressure are relatively higher for CY with LES model at peak systole as seen in Figure 5.13, the pressure values go parallel for CY and CY with LES models within  $U - ICA$  geometry for the first region of the aneurysm sac area.



**Figure 5.13** : Pressure behavior has been observed during last cardiac cycle within *U – ICA* geometry for the region-1 on the aneurysm sac area which is indicated with white circle. *CY* indicates Carreau-Yasuda viscosity model and *LES* indicates Large Eddy Simulation.



**Figure 5.14** : Pressure behavior has been observed during last cardiac cycle within  $U - ICA$  geometry for the region-2 on the aneurysm sac area which is indicated with white circle. CY indicates Carreau-Yasuda viscosity model and LES indicates Large Eddy Simulation.



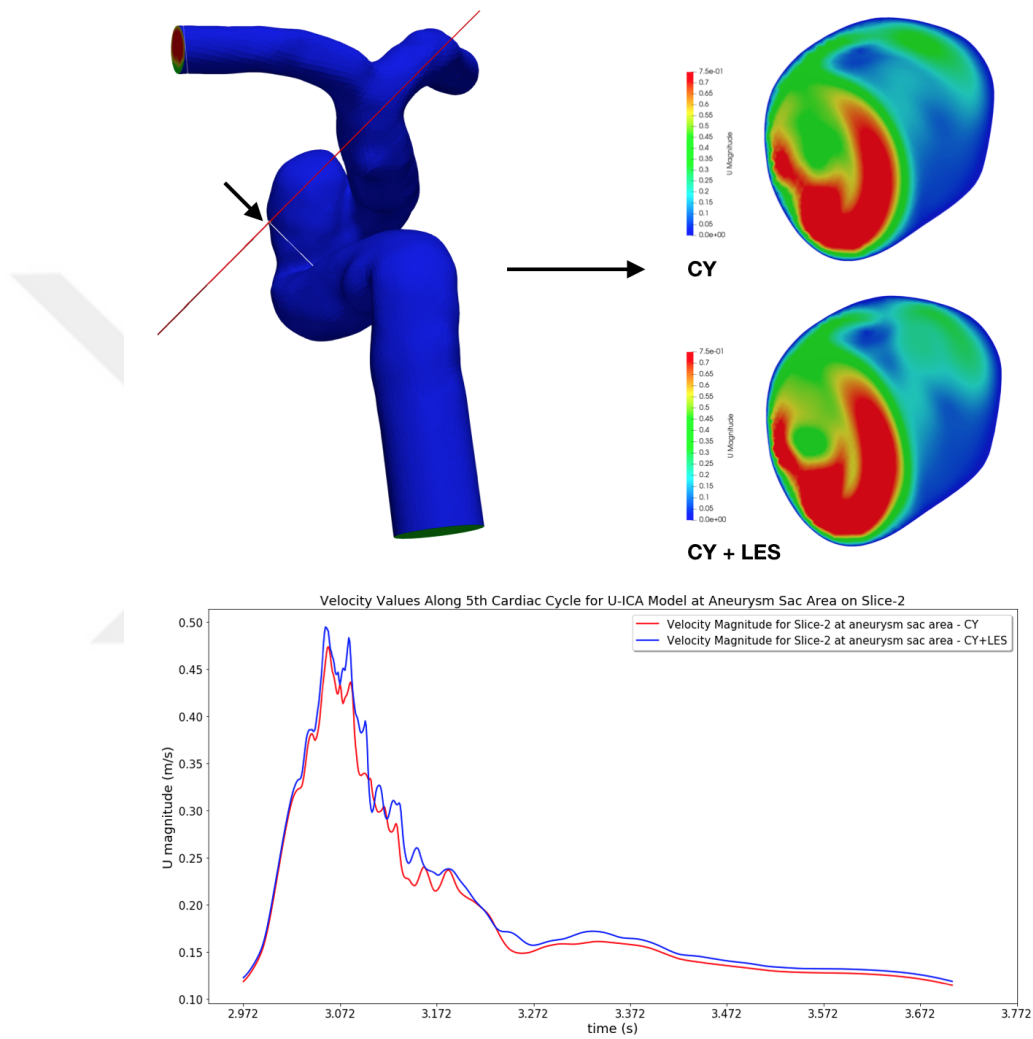
**Figure 5.15** : Velocity behavior has been observed during last cardiac cycle within  $U - ICA$  geometry for the slice-1 on the aneurysm sac area. CY indicates shear-thinning Carreau-Yasuda viscosity model and LES indicates Large Eddy Simulation.

Figure 5.14 represents pressure plot and WSS visualizations at peak systole since both WSS and pressure behaviors have been analyzed for the same areas within  $U - ICA$  geometry. As seen from the Figure 5.14, pressure exhibits approximately the same for CY and CY with LES model within  $U - ICA$  geometry for the second region of the aneurysm sac area.

Figure 5.15 indicates velocity plot and cross section of the aneurysm sac area and corresponding slices of CY and CY with LES models regarding to that cross section. Although it could be seen differences between CY model slice and CY with LES model slice from the Figure 5.15 for first region of aneurysm sac area, the behavior of averaged velocity values go parallel with each other within  $U - ICA$  geometry.

As seen from the Figure 5.16, just same as previous plots, velocity behavior for the second region of the aneurysm sac area within  $U - ICA$  geometry has been observed approximately the same for CY and CY with LES models.





**Figure 5.16** : Velocity behavior has been observed during last cardiac cycle within  $U - ICA$  geometry for the slice-2 on the aneurysm sac area. CY indicates shear-thinning Carreau-Yasuda viscosity model and LES indicates Large Eddy Simulation.

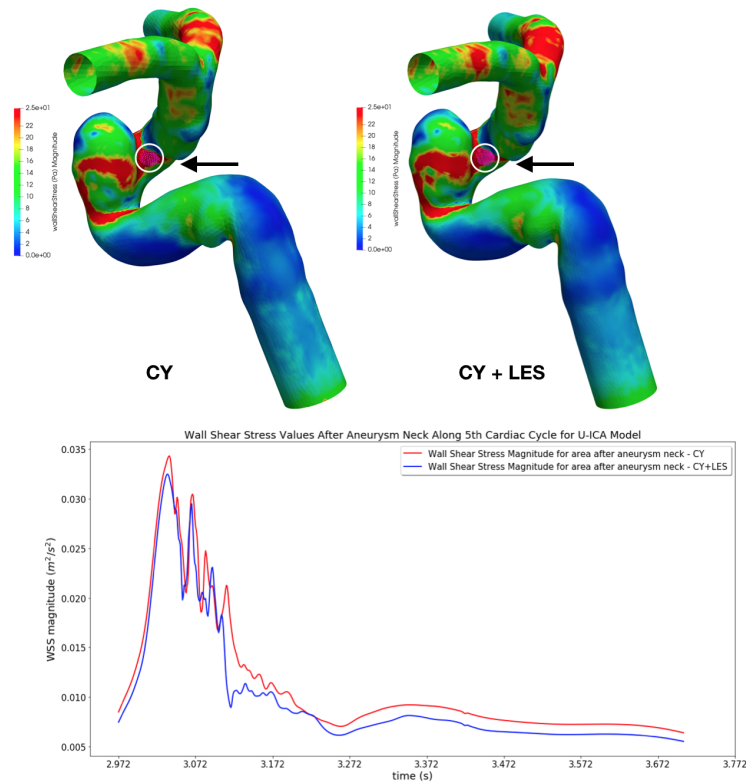


**Figure 5.17 :** WSS behavior has been observed during last cardiac cycle within  $U - ICA$  geometry for the selected region after aneurysm neck which is indicated with white circle. CY indicates Carreau-Yasuda viscosity model and LES indicates Large Eddy Simulation.

The blood flow comes in from the aneurysm inlet and through the parent vessel it reaches to the aneurysm sac area and the area of after aneurysm neck. Therefore, this region is very critical in terms of hemodynamic factors. Hence, the analyses during the cardiac cycle have been also performed for the region of after aneurysm neck in terms of WSS, pressure and velocity within  $U - ICA$  geometry.

Although the values of WSS for the CY model are relatively higher than the WSS values for CY with LES model as seen from the Figure 5.17, WSS behavior is approximately the same for both cases within  $U - ICA$  geometry for the region of after aneurysm neck.

As seen from the Figure 5.18, although there are some differences between the pressure behaviors of CY model and CY with LES model, the values of pressure are approximately the same for both cases within  $U - ICA$  geometry for the after aneurysm neck area.

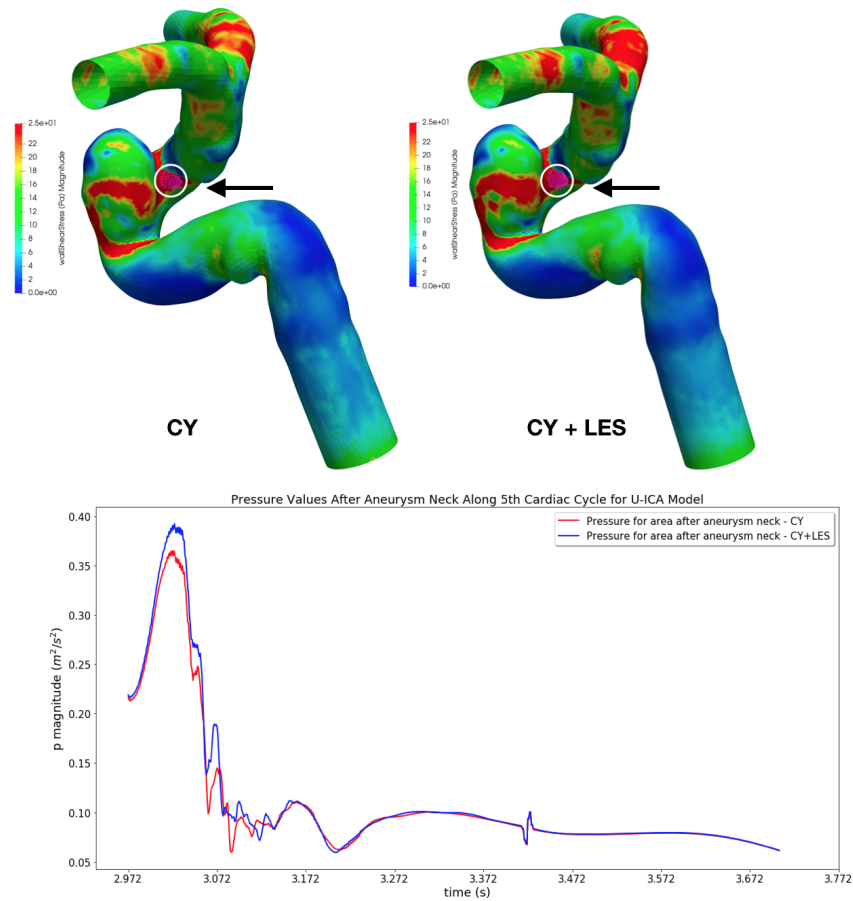


**Figure 5.18** : Pressure behavior has been observed during last cardiac cycle within  $U - ICA$  geometry for the selected region after aneurysm neck which is indicated with white circle. CY indicates Carreau-Yasuda viscosity model and LES indicates Large Eddy Simulation.

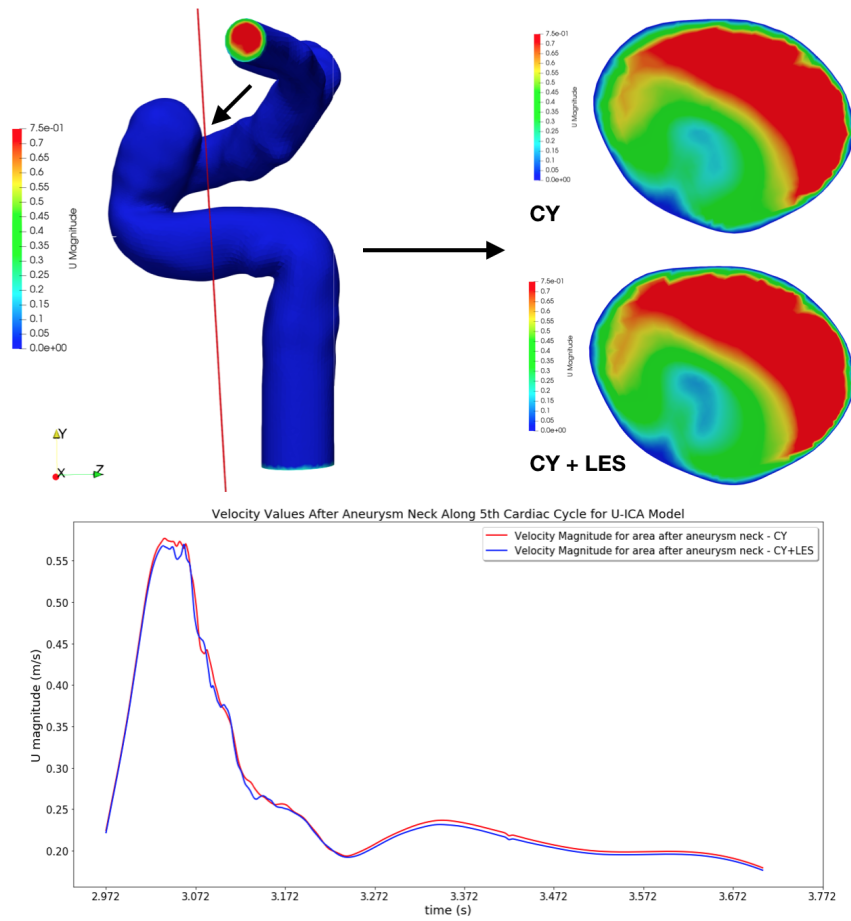


**Figure 5.19** : Velocity behavior has been observed during last cardiac cycle within  $U - ICA$  geometry for the whole slice after aneurysm neck. CY indicates shear-thinning Carreau-Yasuda viscosity model and LES indicates Large Eddy Simulation.

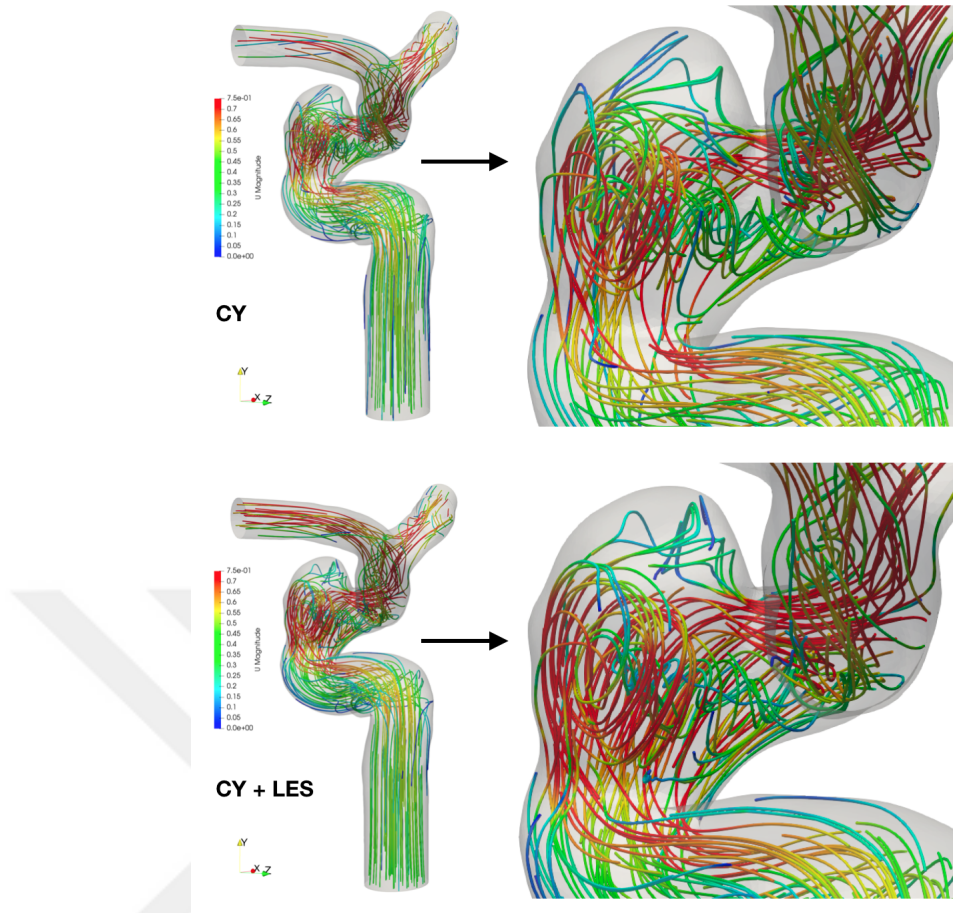


**Figure 5.20** : First row indicates velocity (m/s) streamlines for non-Newtonian Carreau-Yasuda (CY) model while second row indicates velocity streamlines for non-Newtonian Carreau-Yasuda (CY) with LES turbulence effects model for the last cardiac cycle within  $U - ICA$  geometry. The figures have been visualized at peak systole.

As seen from the Figure 5.19, velocity behavior for the slices of the after aneurysm neck area exhibits approximately the same for CY and CY with LES turbulence blood flow models within  $U - ICA$  geometry.

In respect of velocity profile, the streamlines and velocity vector field have been visualized at peak systole of the last cardiac cycle within  $U - ICA$  model for both shear-thinning CY blood flow model and shear-thinning CY with LES turbulence blood flow model. (See Figure 5.20). Velocity profile exhibits smoothly within the inlet area as seen from the Figure 5.20.

It could be inferred from the streamlines and velocity vector field in the Figures 5.20 and 5.21 that, velocity profile tends to behave as *transient* flow when it comes to curvature region of the geometry for both CY and CY with LES models. The

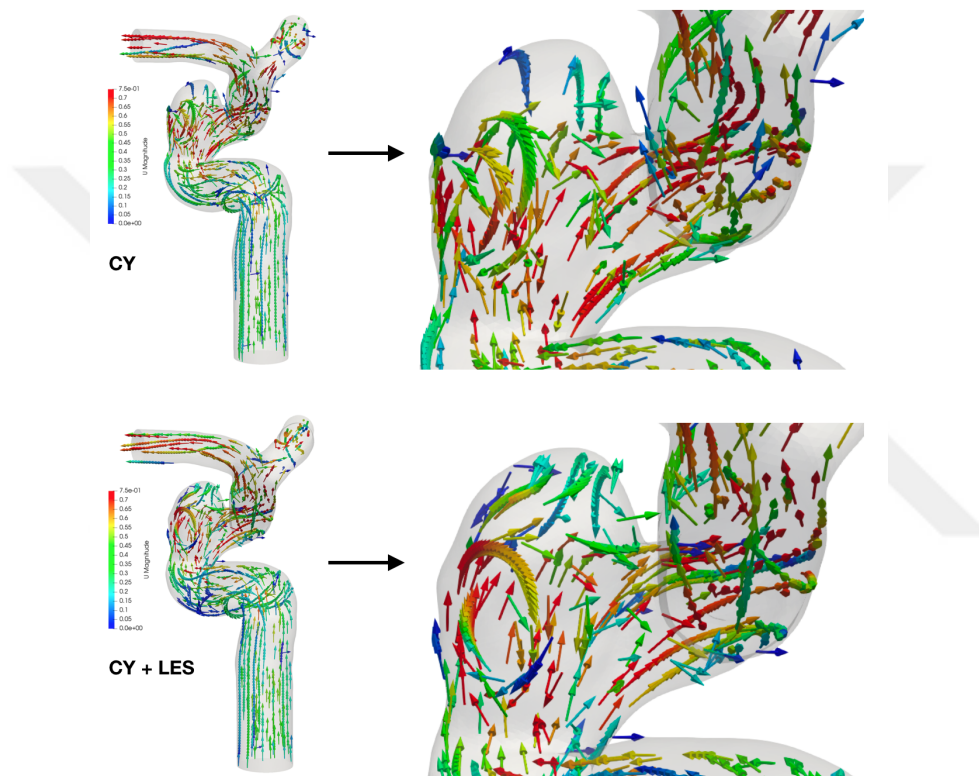


**Figure 5.21** : First row indicates velocity (m/s) vector field for non-Newtonian Carreau-Yasuda (CY) model while second row indicates velocity vector field for non-Newtonian CY with LES turbulence effects model for the last cardiac cycle within  $U - ICA$  geometry. The figures have been visualized at peak systole.

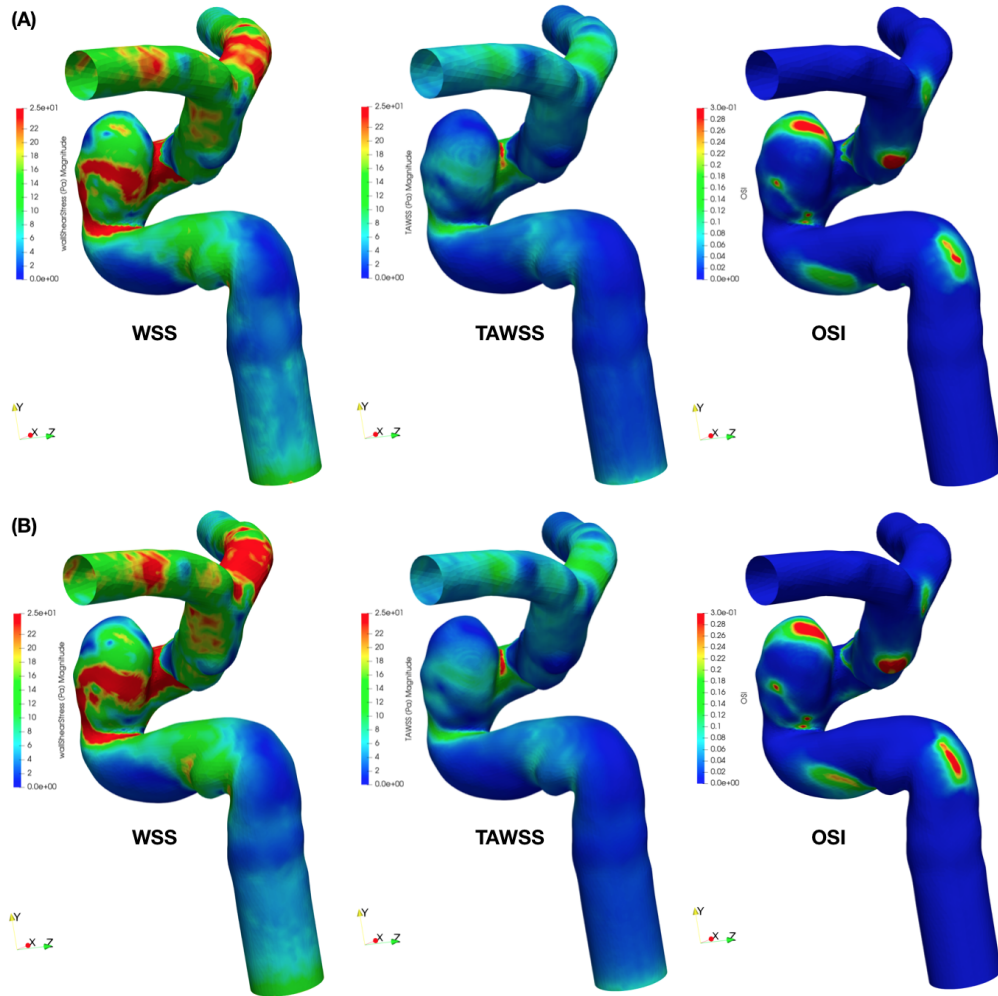


**Figure 5.22** : From left to right, WSS, TAWSS and OSI visualizations for the last cardiac cycle within  $U - ICA$  model. (A) indicates non-Newtonian shear-thinning Carreau-Yasuda flow model (CY) while (B) indicates CY with LES turbulence effects. WSS has been visualized at peak systolic time, TAWSS has been visualized as time-averaged.

streamlines and velocity vector fields show the chaotic and complex behavior of blood flow within  $U - ICA$  model particularly in the sac area.

Figure 5.22 addresses WSS, TAWSS and OSI visualizations for CY and CY with LES model within  $U - ICA$  geometry. WSS has been visualized at peak systole and TAWSS has been visualized as time-averaged. As seen from this figure, the WSS difference between CY model and CY with LES model shows itself aneurysm sac area and daughter vessels of  $U - ICA$  geometry. WSS values for these regions have been observed higher for CY with LES model than the values of WSS for CY model. When it comes to TAWSS for CY model and CY with LES model within  $U - ICA$  geometry, no significant difference has been observed. On the other hand OSI visualization

for CY with LES model has been observed relatively higher than CY model within  $U - ICA$  geometry.

Figure 5.23 represents SWSSG and TASWSSG visualizations for CY model and CY with LES model within  $U - ICA$  geometry. SWSSG has been visualized at peak systole while TASWSSG has been visualized as time-averaged. As seen from this figure, SWSSG has been observed higher for CY with LES model, particularly in the aneurysm sac area and bifurcation region. Since high SWSSG is associated with vascular re-modeling, these regions might be critical. TASWSSG has been observed almost the same for CY model and CY with LES model.

The Figure 5.24 represents hemodynamic factor values as well as WSS visualizations with regard to CY and CY with LES models in terms of whole geometry and aneurysm sac area of  $U - ICA$ . WSS has been visualized at peak systole. As seen from the WSS visualizations in the Figure 5.24, in terms of whole geometry of  $U - ICA$ , CY with LES model has higher WSS particularly in the daughter vessels. When considering aneurysm sac region, it could be seen that WSS has been observed significantly higher for the CY with LES model as seen from the WSS visualizations.

When considering the values of the hemodynamic factors, area-averaged WSS at peak systole has been observed almost the same for CY and CY with LES models. However, the WSS values for both CY and CY with LES model, aneurysm sac areas are approximately 2 Pa higher than the overall whole geometries which provides the insight that the parent vessel has significantly lower WSS values and aneurysm sac region has higher WSS values for both CY and CY with LES models within  $U - ICA$  geometry. This behavior also could be seen clearly from the values of TAWSS in the Figure 5.24.

Aneurysm sac region of  $U - ICA$  geometry has not only high WSS values but also has high SWSSG and TASWSSG values. The area-averaged SWSSG values at peak systole have been observed higher in terms of CY with LES model for both whole geometry and aneurysm sac area. When considering whole geometry and aneurysm sac area, as seen from the Figure 5.24, aneurysm sac area has significantly higher values for both CY and CY with LES models. Since high SWSSG values might be associated with endothelial dysfunction and vascular remodeling, aneurysm sac area



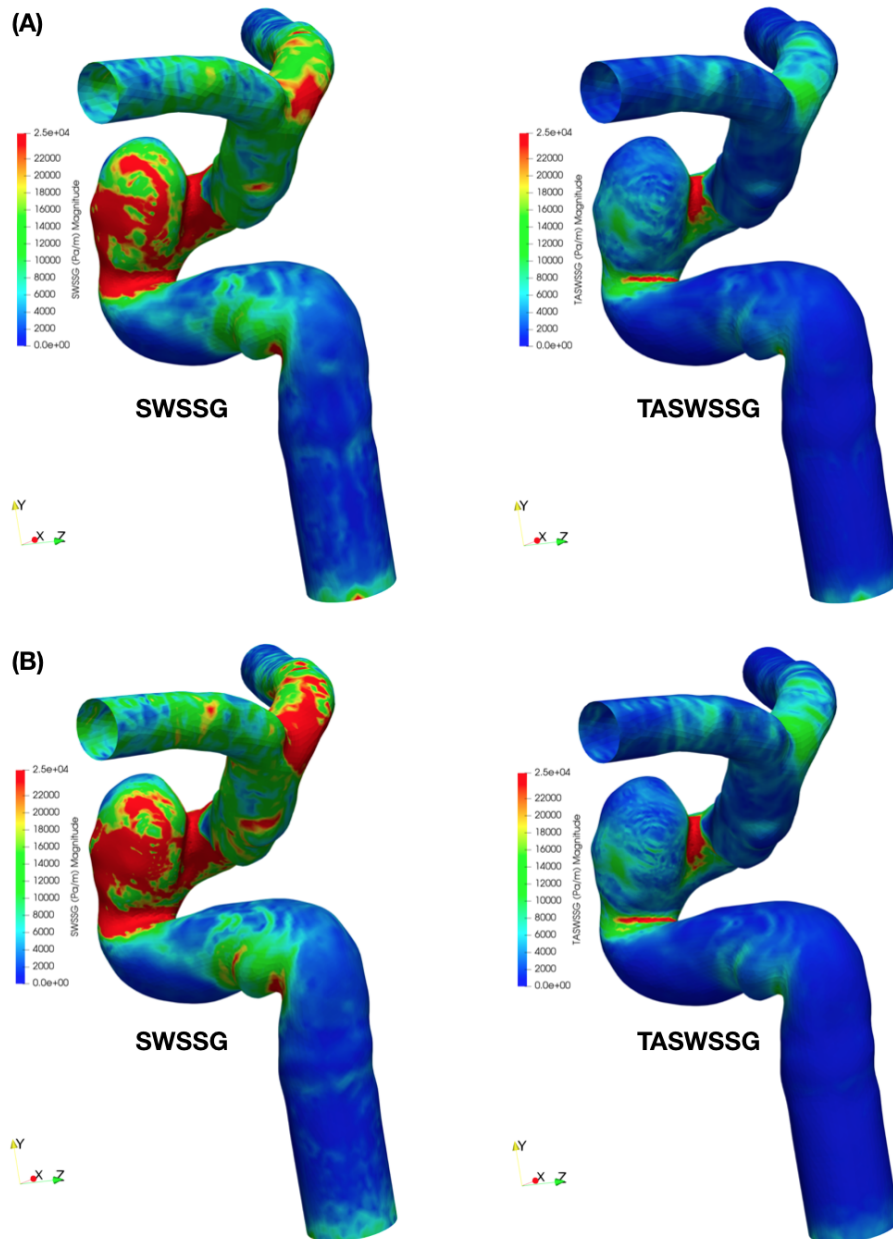
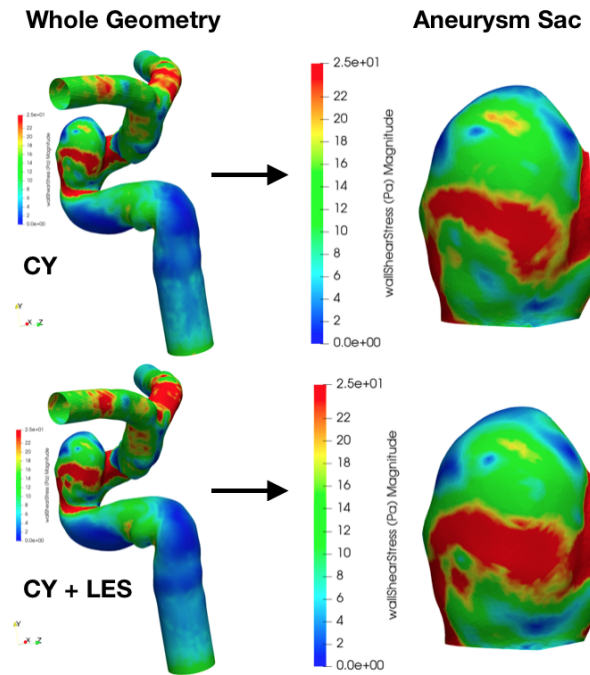


**Figure 5.23** : SWSSG and TASWSSG visualizations for the last cardiac cycle within  $U - ICA$  model. (A) indicates non-Newtonian shear-thinning Carreau-Yasuda flow model (CY) while (B) indicates CY with LES turbulence effects. SWSSG has been visualized at peak systolic time, TASWSSG has been visualized as time-averaged.



Hemodynamic Parameters	Carreau-Yasuda Model (CY)		CY with LES Turbulence Model (CY+LES)	
	Whole Geometry	Aneurysm Sac	Whole Geometry	Aneurysm Sac
WSS (at peak systole)	11,473 Pa	13,384 Pa	11,685 Pa	13,465 Pa
TAWSS	4,002 Pa	4,302 Pa	3,985 Pa	4,256 Pa
SWSSG (at peak systole)	13599,381 Pa/m	20647,538 Pa/m	14715,528 Pa/m	21878,242 Pa/m
TASWSSG	3970,855 Pa/m	5554,742 Pa/m	4023,627 Pa/m	5447,095 Pa/m
OSI	0,021	0,039	0,023	0,044
OSI (maximum)	0,435	0,435	0,472	0,457
OSI (minimum)	0	0,0003	0	0,0003

**Figure 5.24** : The figure represents the values of hemodynamic factors and WSS visualizations for whole geometry and aneurysm sac area within  $U - ICA$  model. CY indicates Carreau-Yasuda and LES indicates Large Eddy Simulation. WSS has been visualized at peak systole.

of  $U - ICA$  geometry might have high risk of rupture. Also it could be seen that TASWSSG values regarding to whole geometry and aneurysm sac areas provide an insight that parent vessel has significantly lower SWSSG values than aneurysm sac area.

As seen from the Figure 5.24, mean OSI values are higher for the CY with LES model within both whole geometry and aneurysm sac area. When considering whole geometry and aneurysm sac area for  $U - ICA$  geometry, mean OSI values are higher within aneurysm sac region. Since high OSI values are associated with vascular remodeling and aneurysm rupture, aneurysm sac region might have a critical zone in terms of high rupture risk area within  $U - ICA$  geometry. When considering maximum OSI values, for CY model, the maximum OSI value could be observed within aneurysm sac area, however, for CY with LES model has not only the higher values of maximum OSI but also has higher OSI value within the region other than the aneurysm sac area. From these results, it has been observed that CY with LES model has effect the WSS direction and consequently OSI values increase under the turbulence effects. High rupture risk has been observed within  $U - ICA$  geometry, particularly for CY with LES turbulence blood flow model case.

Hemodynamic parameters in terms of mean WSS, mean OSI and maximum OSI for  $U - ICA$  geometry have been observed within the ranges of the corresponding ranges of the values of the study including over 1600 ruptured and unruptured patient-specific cerebral aneurysm data, published recently by Detmer et al. [117].

Within the current study, lower WSS values have been observed in the ruptured cerebral aneurysm  $R - ICA$  than the unruptured cerebral aneurysm  $U - ICA$  (See Figure 5.41). From the literature, Shojima et al. [54] had been concluded that low WSS might be associated with the ruptured cerebral aneurysms. Xiang et al. [30], had been observed lower WSS and higher OSI in the ruptured cerebral aneurysms. Within this current study, lower WSS values have been observed for ruptured cerebral aneurysm  $R - ICA$  - similar with the literature - while higher OSI values have been observed for unruptured cerebral aneurysm  $U - ICA$  (see Figures 5.24 and 5.41). Within the literature, higher OSI values are usually associated with ruptured cerebral aneurysms, however, within the current study, the findings regarding to OSI are

opposite. Therefore, since high OSI values are strongly associated with the aneurysm rupture,  $U - ICA$  aneurysm might have a high risk of rupture.

#### **5.4 Numerical Simulation Results for R-ICA**

The ruptured cerebral aneurysm data localized in ICA has been investigated in order to examine the effects of hemodynamic factors such as WSS and OSI on the aneurysm. CFD simulations have been carried out during five cardiac cycles to ensure the stability and the last cardiac cycle has been analyzed and visualized.

WSS and pressure factors have been analyzed along the last cardiac cycle for the simulations of shear-thinning Carreau-Yasuda (CY) blood flow model and shear-thinning CY with LES blood flow model. The assessment requires to select one circular region and perform the analysis during the time within that region. Regarding to the WSS and pressure factors, they have been analyzed on the same regions, one circular area from the location of before aneurysm neck and the other circular area from after aneurysm neck. The circular regions have been selected with regards to the higher value regions of the factors.

The results obtained subsequent to the blood flow simulations for the non-Newtonian with Carreau-Yasuda (CY) viscosity model and CY with LES blood flow model have been investigated in terms of hemodynamic factors within  $R - ICA$ .

WSS and pressure have been observed along the last cardiac cycle on the same regions for both shear-thinning CY model and CY with LES turbulence blood flow model.

The Figure 5.25 infers that WSS values at the peak systolic time for shear-thinning CY model are relatively higher than the values for shear-thinning CY with LES turbulence blood flow model. After peak systolic time, the values go parallel with each other within  $R - ICA$  geometry for the region of before aneurysm neck.

As seen from the Figure 5.26, although the pressure values for shear-thinning CY model in the location before aneurysm neck are relatively higher than the values for CY with LES turbulence blood flow model at peak systole within  $R - ICA$  model, after peak systole, the values are almost the same.

Velocity profile during last cardiac cycle has been analyzed for both shear-thinning CY model and CY with LES turbulence flow model. In order to examine velocity

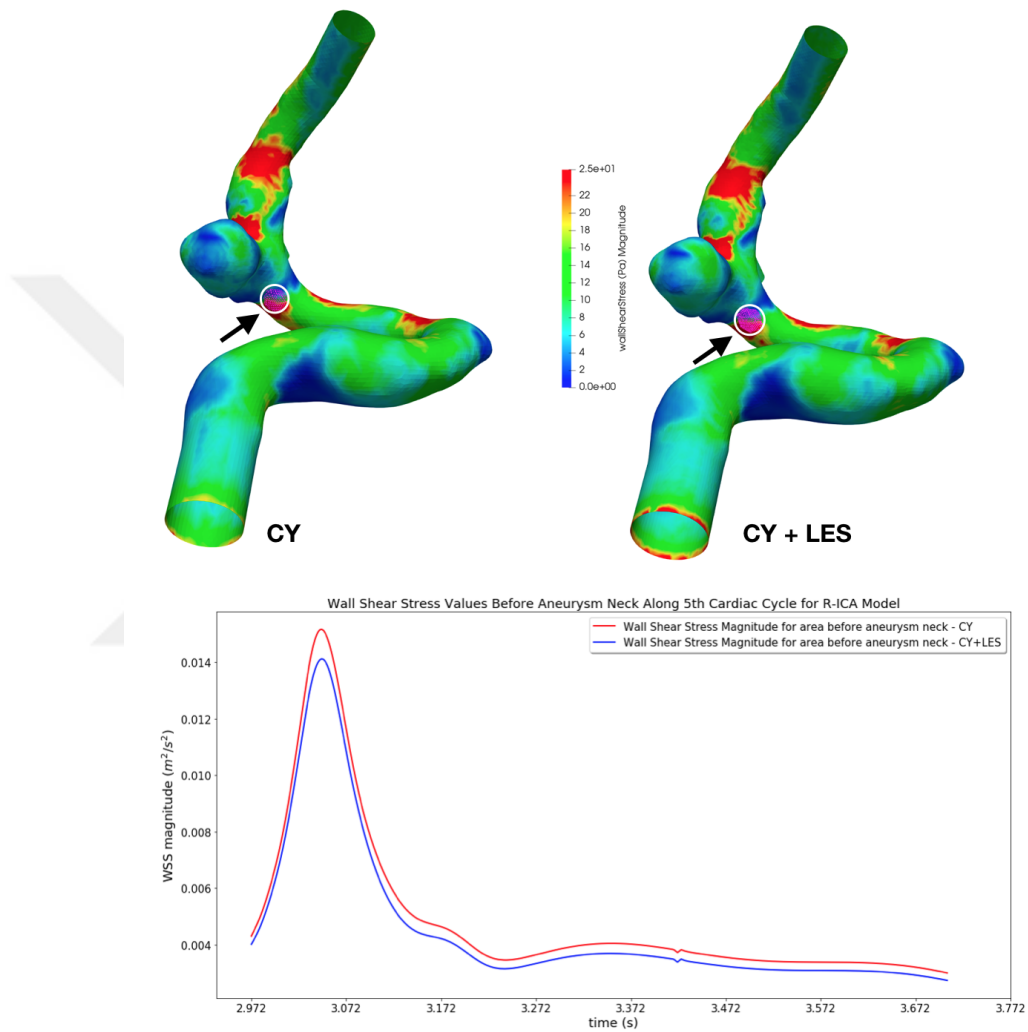


**Figure 5.25** : The white circles indicate where WSS behaviors have been observed before aneurysm neck area within *R – ICA* model (top). WSS plot indicates the comparison of CY model and CY with LES blood flow model for the indicated region (bottom).

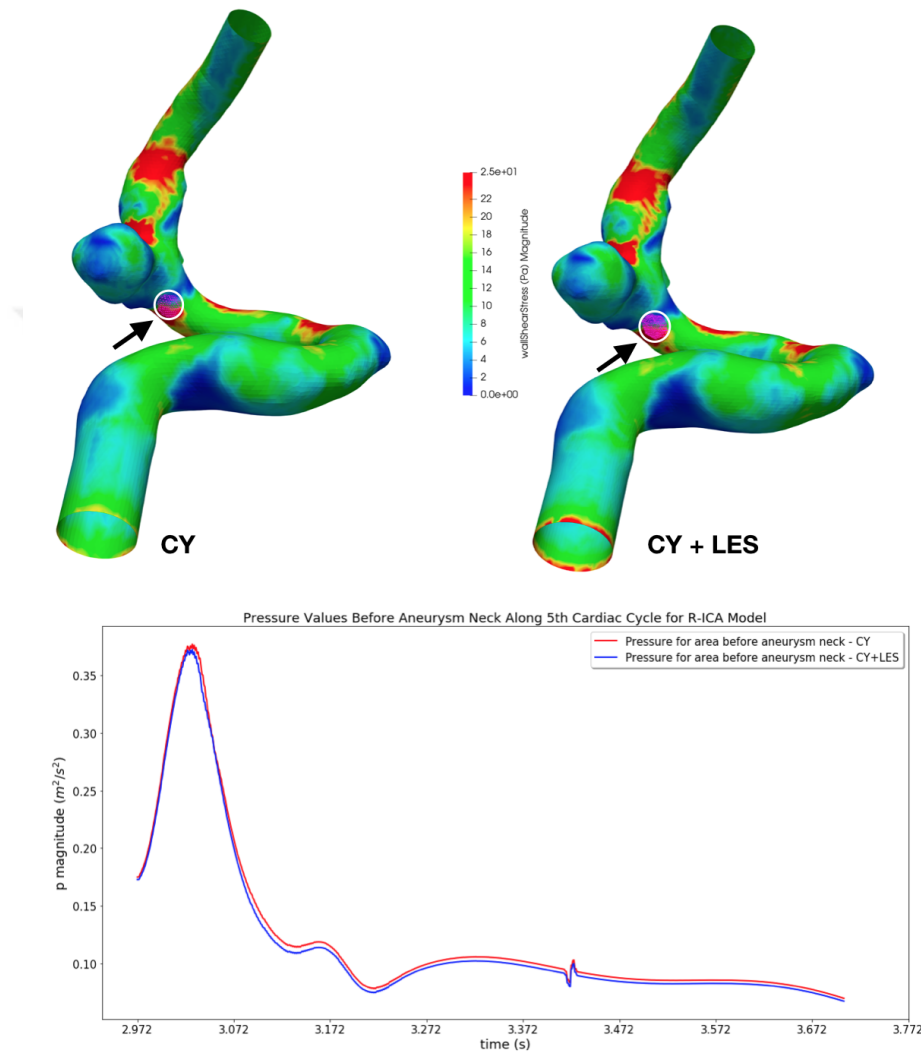


**Figure 5.26** : Pressure and WSS have been observed for the same regions. White circles indicate where pressure behaviors have been observed (top). The plot indicates pressure values during the last cardiac cycle for the area before aneurysm neck within *R – ICA* for shear-thinning CY model and CY with LES turbulence blood flow model (bottom).

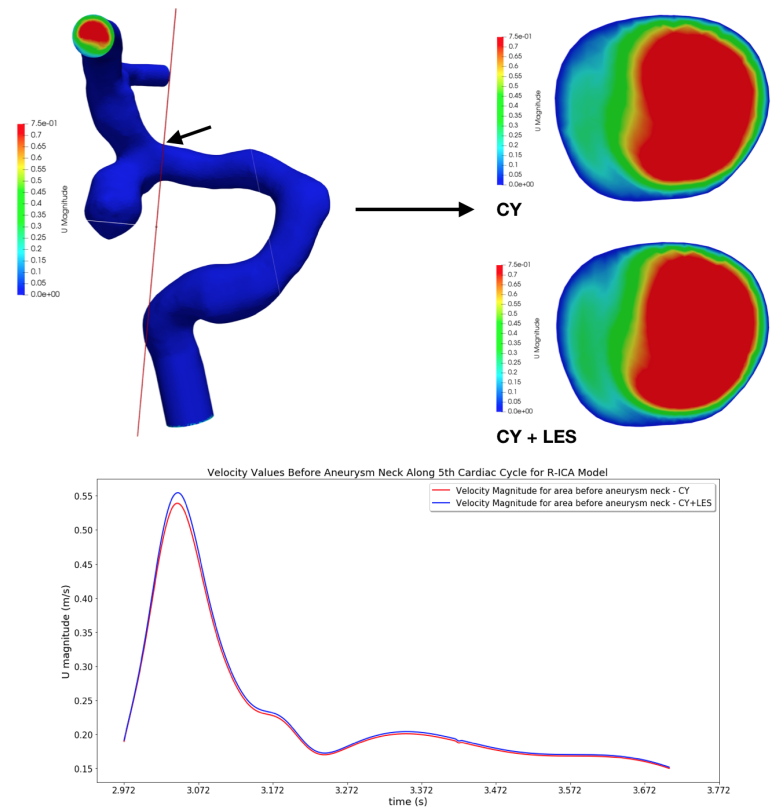


**Figure 5.27** : Velocity profile has been observed on the selected region (m/s) within *R – ICA* model during last cardiac cycle. One slice has been taken before aneurysm neck (top) and the plot indicates the velocity behavior for the whole slice within the *R – ICA* geometry for CY and CY with LES blood flow model (bottom).

behavior, one slice has been taken from the location of before aneurysm neck and the whole slice has been analyzed. The same process has been implemented to the location of after aneurysm neck. Velocity profile has been observed during the time on the selected regions. Moreover, the streamlines have been visualized in order to observe chaotic behavior of the flow within the aneurysm, particularly in the sac area, for both shear-thinning CY model and CY with turbulence flow model within *R – ICA* geometry.

As seen from the Figure 5.27, the velocity behavior is exactly the same on the slice before aneurysm neck area for shear-thinning CY model and shear-thinning CY with LES turbulence blood flow model within *R – ICA* geometry.

WSS values have been analyzed also for the aneurysm sac area within *R – ICA* geometry for both shear-thinning CY model and shear-thinning CY with LES turbulence blood flow model.

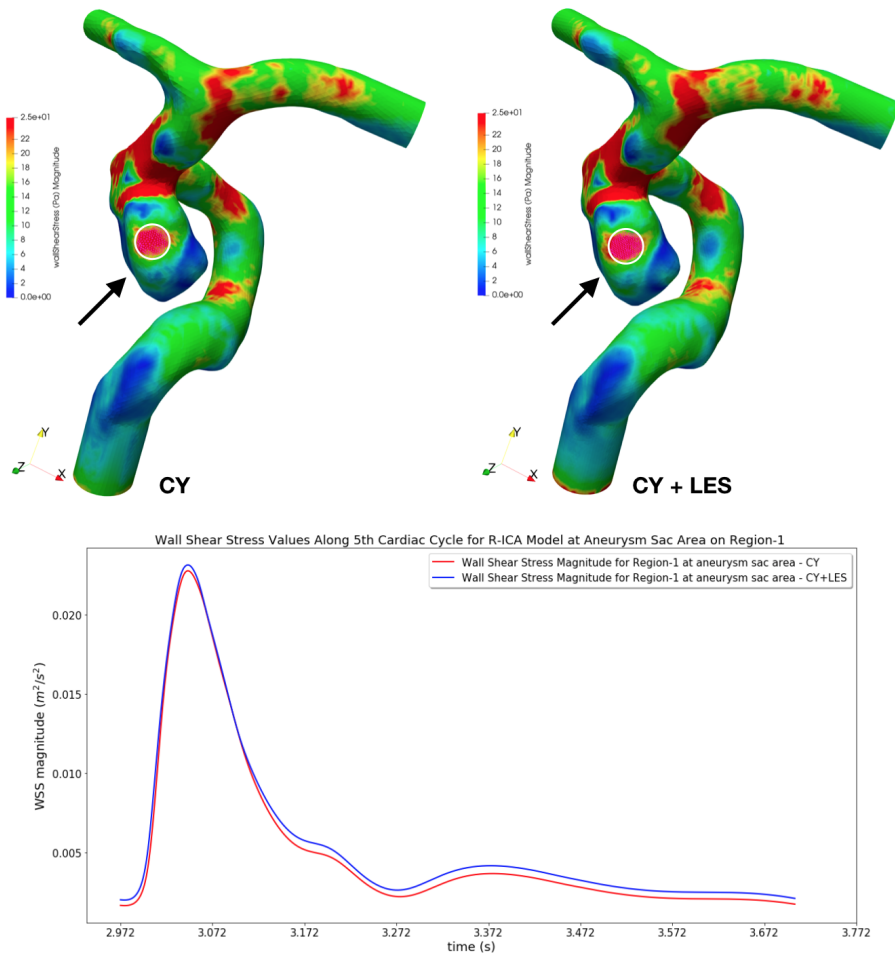


**Figure 5.28** : The white circle indicates where WSS behavior has been observed on the aneurysm sac area for region-1 within *R – ICA* model (top). WSS plot indicates the comparison of CY model and CY with LES blood flow model for the indicated region (bottom).



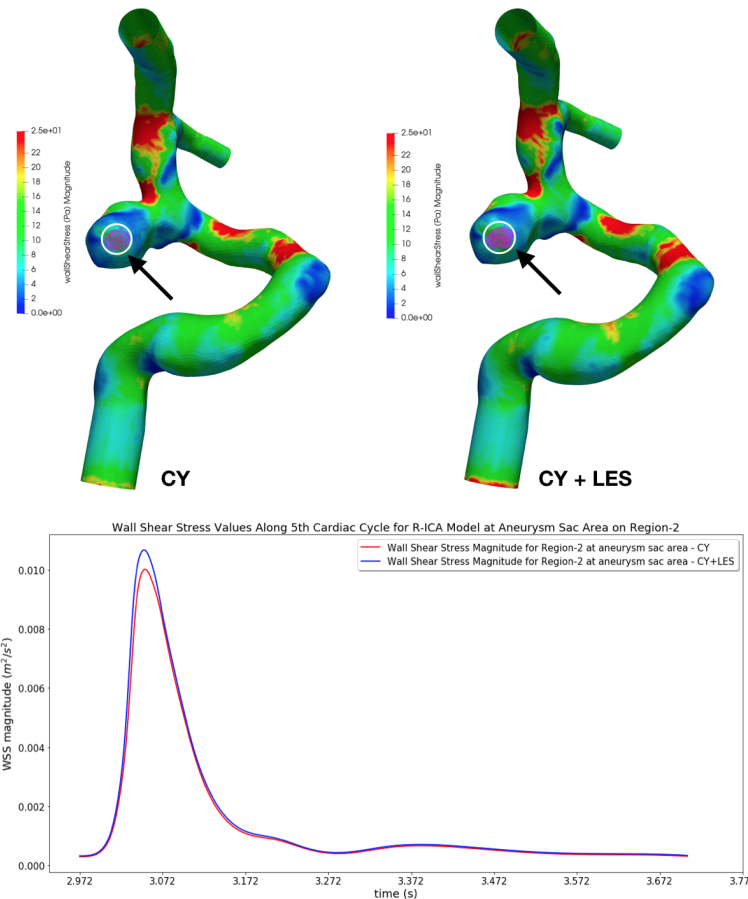


**Figure 5.29 :** The white circles indicate where WSS behaviors have been observed on the aneurysm sac area for region-2 within *R – ICA* model (top). WSS plot indicates the comparison of CY model and CY with LES turbulence blood flow model for the indicated region (bottom).

Figure 5.28 indicates selected region on the aneurysm sac area and WSS plot during the last cardiac cycle for the indicated region. The values in terms of WSS with regard to CY and CY with LES turbulence blood flow models go parallel with each other within *R – ICA* geometry.

Within the Figure 5.29, the circle indicates the selected region for the aneurysm sac area. The WSS values have been observed with regard to shear-thinning CY and shear-thinning CY with LES turbulence blood flow models during the last cardiac cycle within *R – ICA* model. The WSS values with regard to CY with LES blood flow model are relatively higher than shear-thinning CY blood flow model. However, both plots go parallel with each other during the cardiac cycle.

In the aneurysm sac area, pressure behavior has been observed for the exactly same region where WSS behavior has been observed.

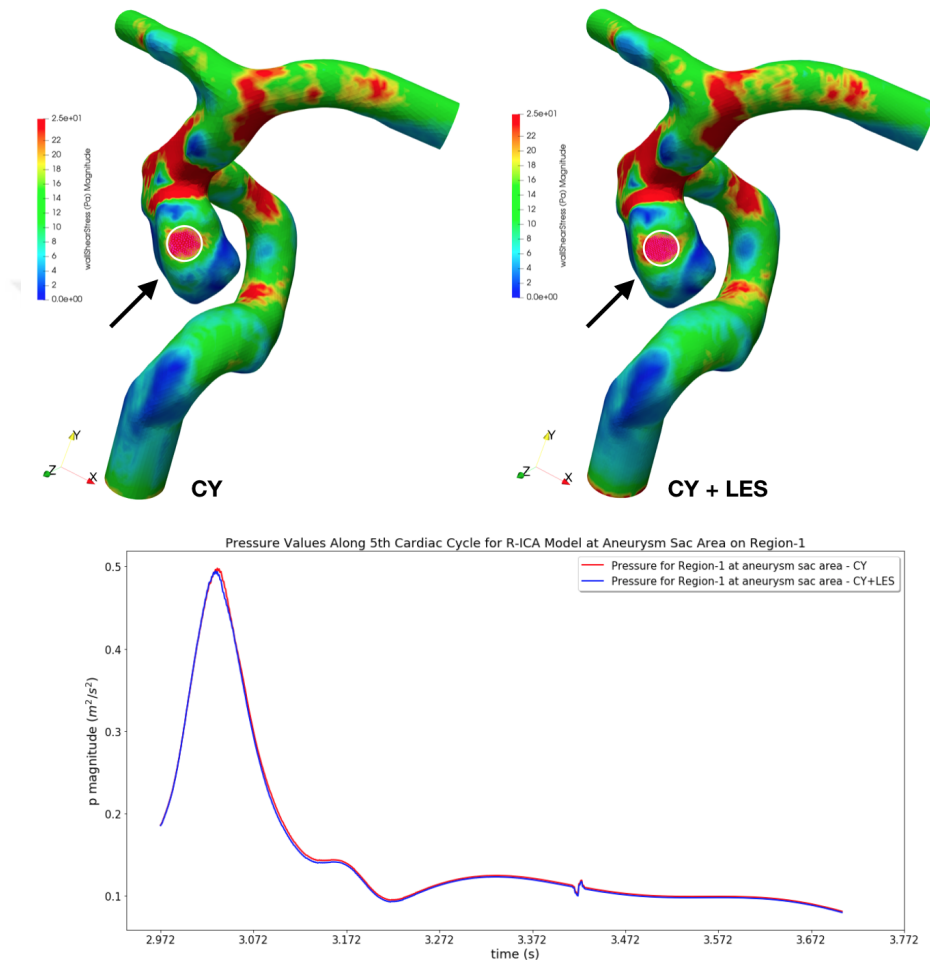


**Figure 5.30** : Pressure and WSS have been observed for the same regions. White circles indicate where pressure behaviors have been observed (top). The plot indicates pressure values during the last cardiac cycle in the aneurysm sac area for region-1 within *R – ICA* geometry for shear-thinning CY model and CY with LES turbulence blood flow model (bottom).

As seen in the Figure 5.30, the values in terms of pressure with regard to CY and CY with LES turbulence blood flow models are almost the same for the region-1 on the aneurysm sac area within  $R - ICA$  geometry.

As seen from the Figure 5.31, pressure values on the aneurysm sac area for region-2 within  $R - ICA$  geometry are the same for CY and CY with LES turbulence blood flow models.

Within aneurysm sac area, also the velocity behavior has been observed for shear-thinning CY blood flow model and shear-thinning CY with LES turbulence blood flow model on two slices within  $R - ICA$  geometry.

The Figure 5.32 indicates first slice on the aneurysm sac area within  $R - ICA$  model. Although the velocity values for CY with LES turbulence model are relatively higher at peak systole than the values for CY blood flow model, the plots go parallel with each other after peak systole.

The Figure 5.33 indicates second selected slice on the aneurysm sac area within  $R - ICA$  model and the velocity analysis for that slice with regard to CY and CY with LES turbulence blood flow model. The velocity behavior exhibits approximately same as the plot in the Figure 5.32.

The WSS, pressure and velocity behaviors have been observed for the area after aneurysm neck within  $R - ICA$  geometry for both CY and CY with LES turbulence blood flow models.

Figure 5.34 indicates WSS analysis with regard to CY and CY with LES turbulence blood flow models for the region after aneurysm neck within  $R - ICA$  geometry. The WSS values for CY model have been observed higher than the values of CY with LES model for the selected region of after aneurysm neck within  $R - ICA$  geometry.

In spite of the pressure values at peak systole have been observed relatively higher for the shear-thinning CY blood flow model, the values for both cases during the last cardiac cycle are almost the same (See Figure 5.35).

As seen from the Figure 5.36, within the slice after aneurysm neck area, the values in terms of velocity regarding CY and CY with LES blood flow model are exactly the same within  $R - ICA$  geometry.

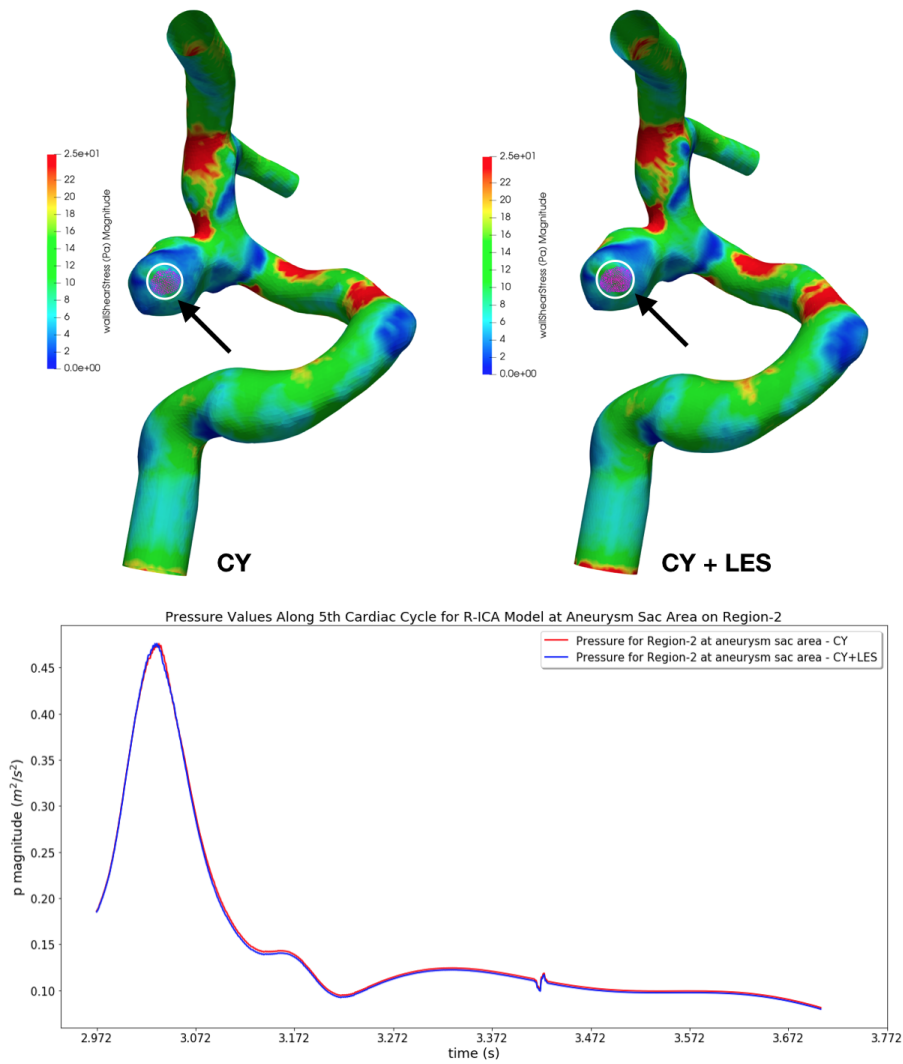


**Figure 5.31** : Pressure and WSS have been observed for the same regions. White circles indicate where pressure behaviors have been observed (top). The plot indicates pressure values during the last cardiac cycle in the aneurysm sac area for region-2 within *R – ICA* geometry for shear-thinning CY model and CY with LES turbulence blood flow model (bottom).

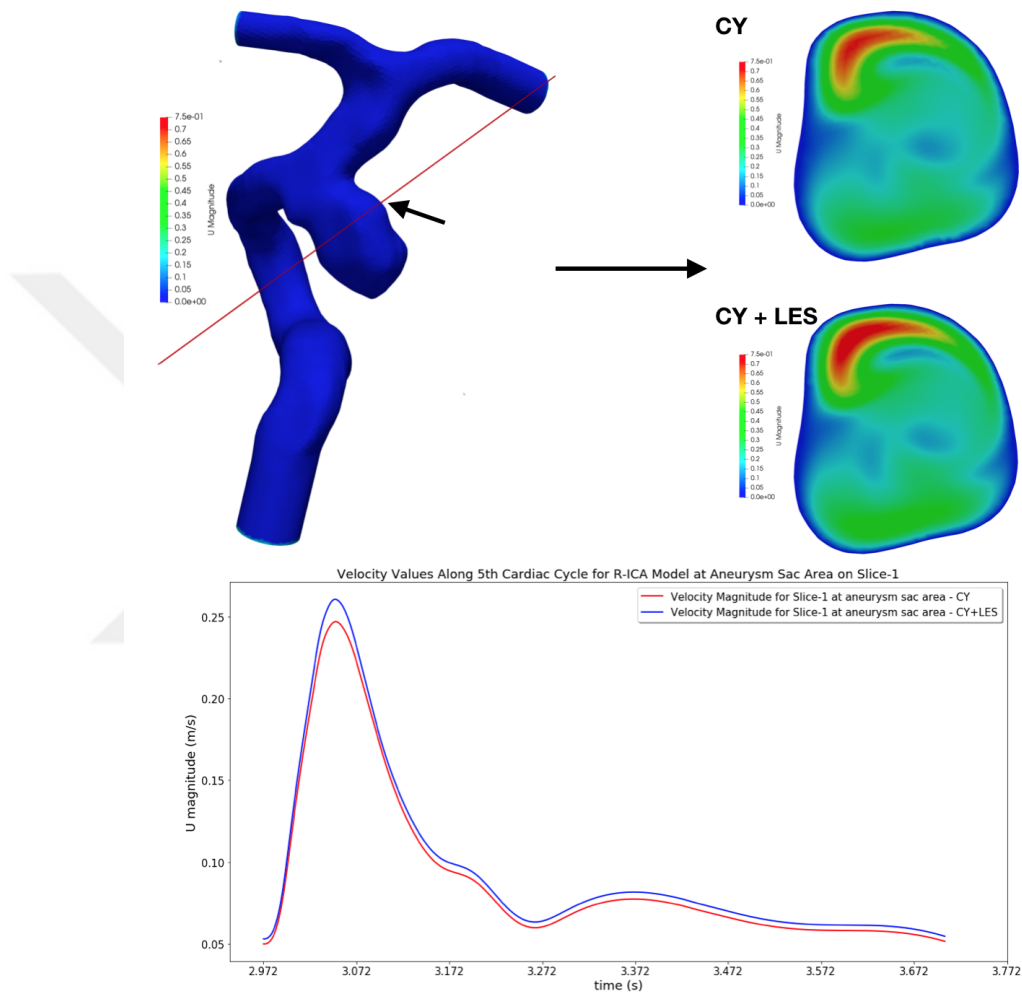


**Figure 5.32** : Velocity profile has been observed on the selected zone within *R – ICA* model during last cardiac cycle. One slice has been taken from aneurysm sac area as slice-1 (top) and the plot indicates the velocity behavior for the whole slice within the *R – ICA* geometry for *CY* and *CY* with *LES* blood flow model (bottom).

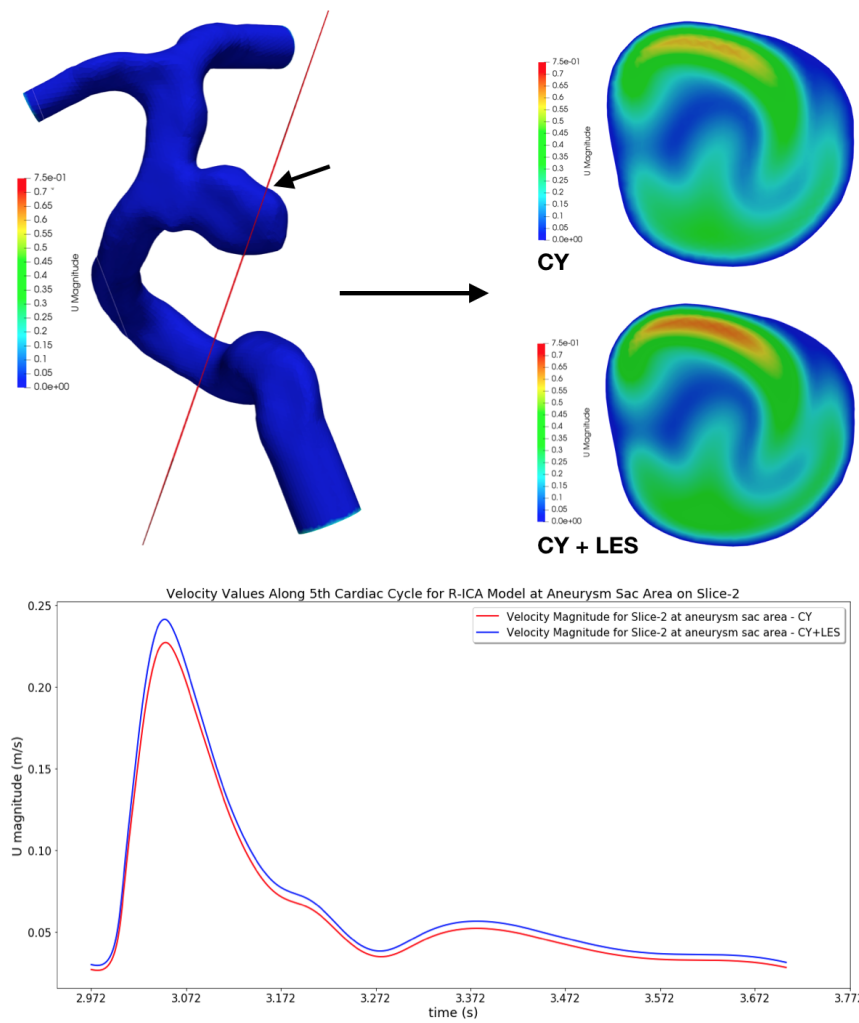


**Figure 5.33 :** Velocity profile has been observed on the selected zone within *R – ICA* model during last cardiac cycle. One slice has been taken from aneurysm sac area as slice-2 (top) and the plot indicates the velocity behavior for the whole slice within the *R – ICA* geometry for CY and CY with LES blood flow model (bottom).

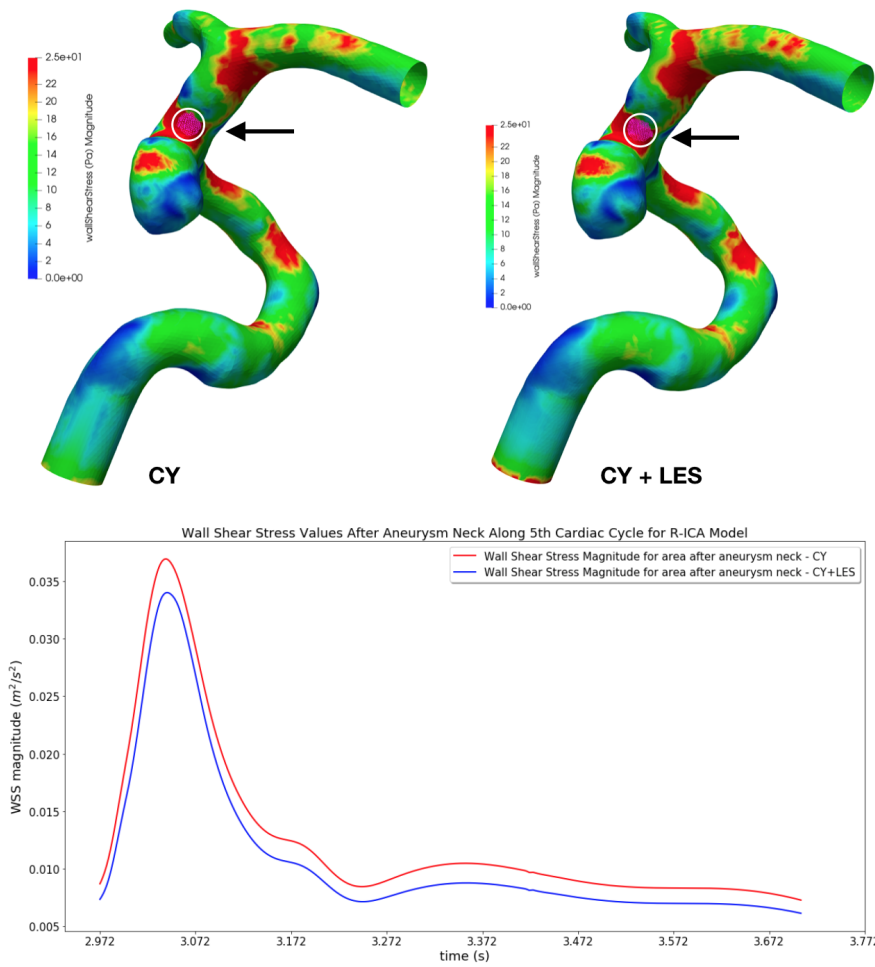


**Figure 5.34** : WSS behavior has been observed on the selected zone after aneurysm neck within *R – ICA* model during last cardiac cycle (top) and the plot indicates the WSS behavior for the selected area within the *R – ICA* geometry for CY and CY with LES blood flow model (bottom).

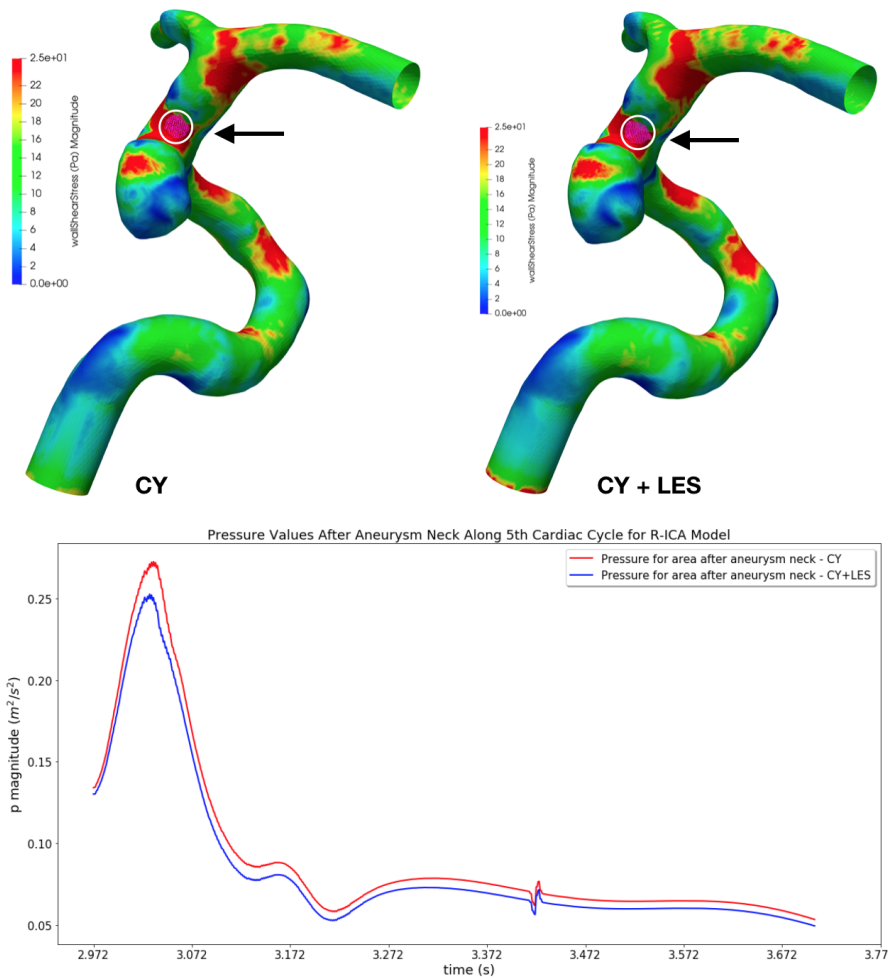


**Figure 5.35** : Pressure behavior has been observed on the selected zone after aneurysm neck within *R – ICA* model during last cardiac cycle (top) and the plot indicates the pressure behavior for the selected area within the *R – ICA* geometry for CY and CY with LES blood flow model (bottom).



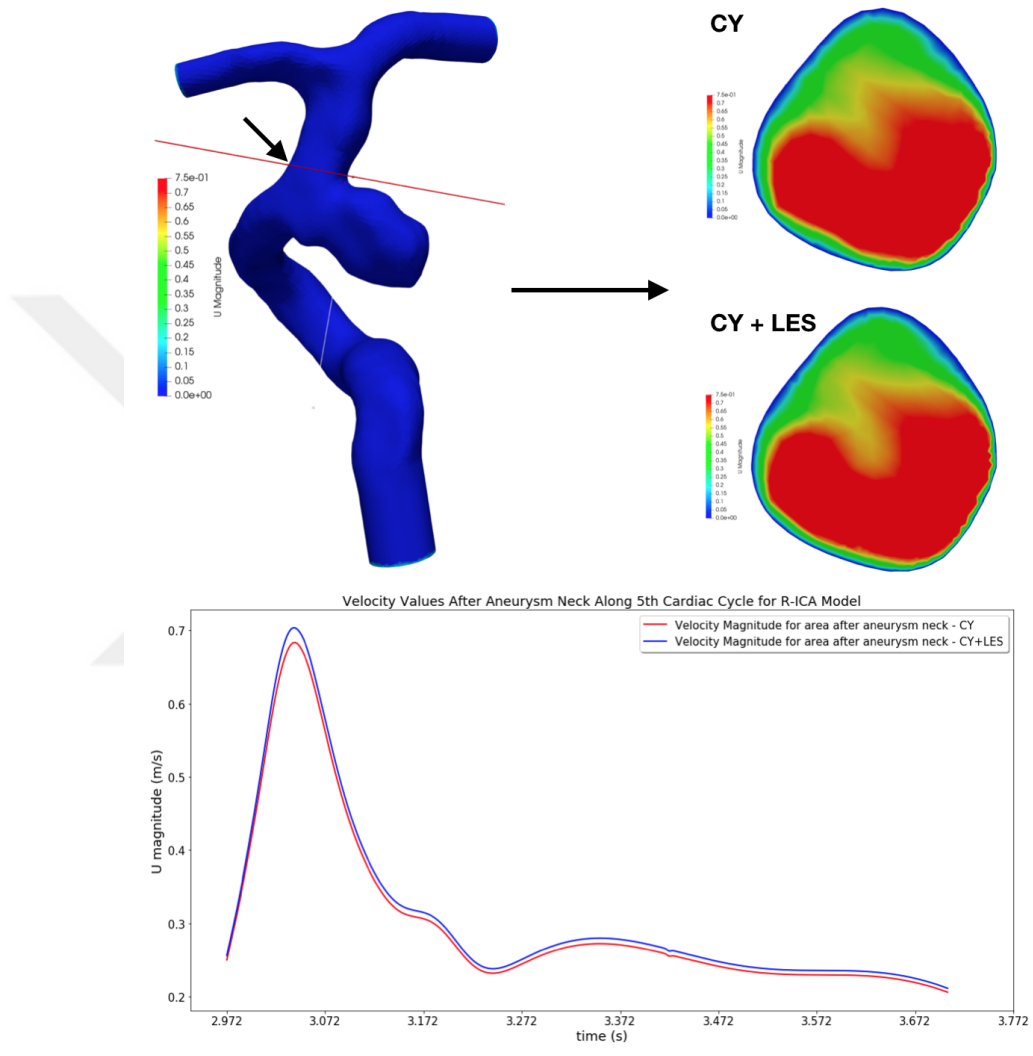


**Figure 5.36 :** Velocity profile has been observed on the selected zone within *R – ICA* model during last cardiac cycle. One slice has been taken after aneurysm sac area (top) and the plot indicates the velocity behavior for the whole slice within the *R – ICA* geometry for CY and CY with LES blood flow model (bottom).

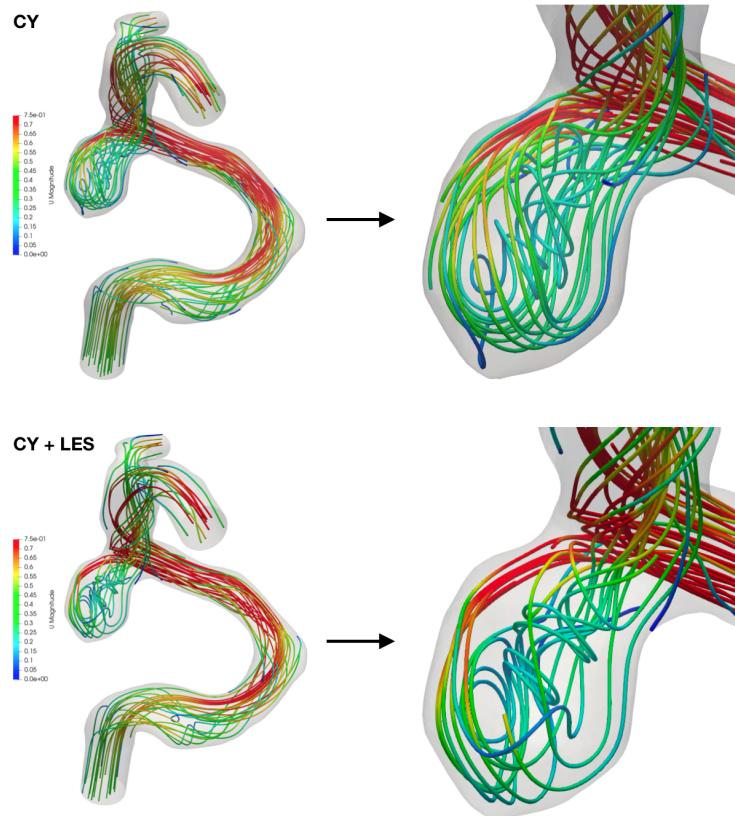


**Figure 5.37** : Velocity (m/s) streamlines at peak systolic time of the last cardiac cycle within  $R - ICA$  model. First row, CY indicates shear-thinning Carreau-Yasuda model while second row, CY + LES indicates shear-thinning CY with LES turbulence flow model.

Regarding to the velocity profile within ruptured patient-specific cerebral aneurysm model at peak systolic time in the last cardiac cycle, the streamlines and velocity vector fields have been visualized for both shear-thinning and turbulence flow models by using ParaView [101] software (See Figures 5.37 and 5.38). As seen from the Figure 5.37, in the both shear-thinning and turbulence flow models, the velocity profile exhibits smoothly in the inlet and when the velocity comes across the curvature region, the streamlines demonstrate that the velocity tends to exhibit *transient* behavior for both shear-thinning model and turbulence flow model. The difference between the streamlines of shear-thinning model and turbulence flow model shows itself most particularly in the aneurysm sac area. Higher velocity values could be observed in the aneurysm sac area for turbulence flow model on the other hand the streamlines could be observed more complex in the sac area for shear-thinning model. Notwithstanding, the streamlines demonstrate the chaotic and complex behavior of the blood flow within  $R - ICA$  model for both shear-thinning and turbulence flow models.

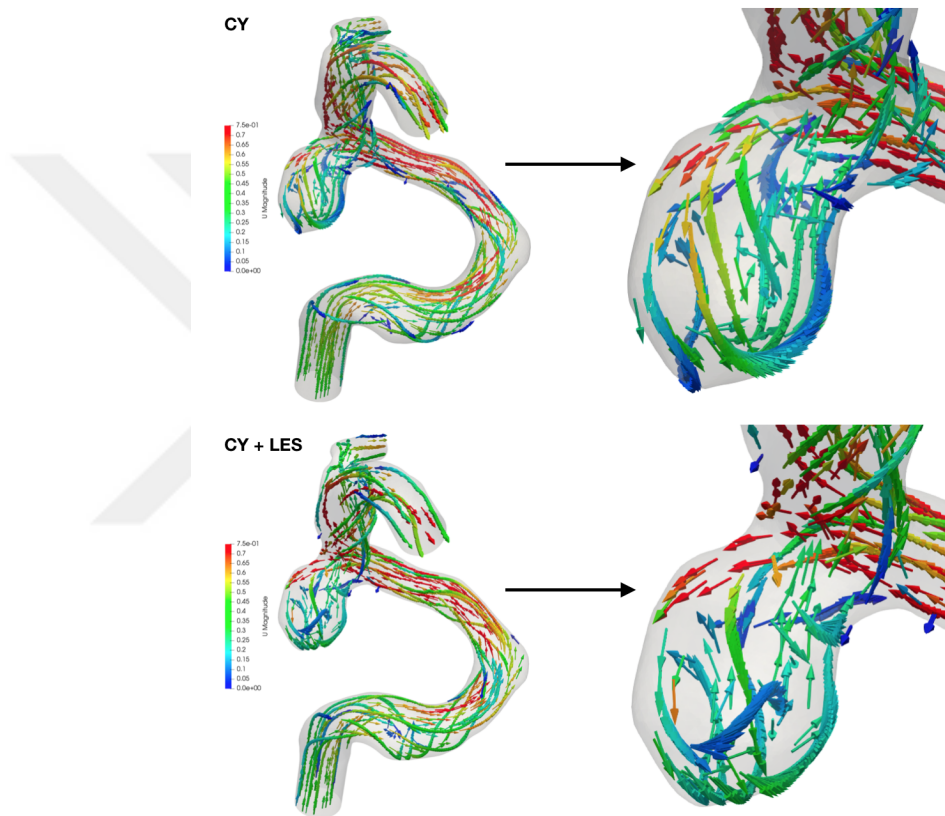


**Figure 5.38** : Velocity vector field at peak systole of the last cardiac cycle within  $R - ICA$  model. First row, CY indicates shear-thinning Carreau-Yasuda model while second row, CY + LES indicates Carreau-Yasuda with LES turbulence flow model.

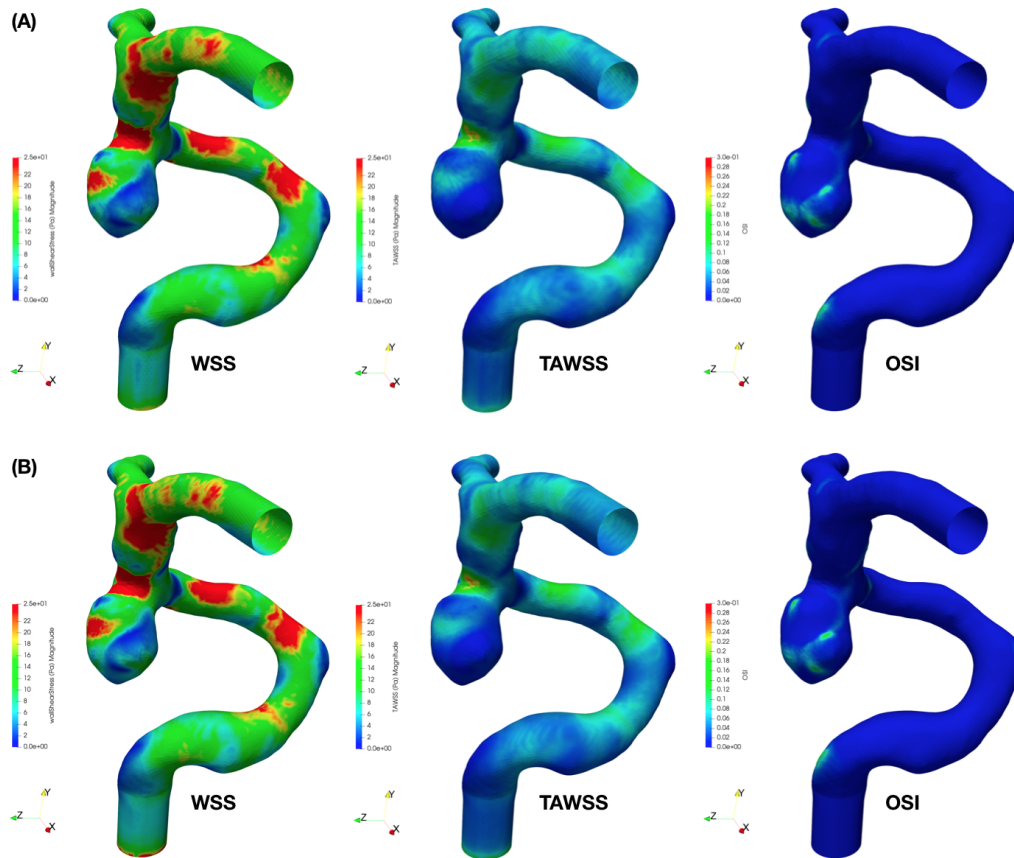


**Figure 5.39** : From left to right, WSS, TAWSS and OSI visualizations for the last cardiac cycle within  $R - ICA$  model. WSS has been visualized at peak systolic time, TAWSS has been visualized as time-averaged. First row (A) indicates shear-thinning CY model while second row (B) indicates shear-thinning CY with LES turbulence flow model.

Subsequent to the comparisons between shear-thinning CY model and shear-thinning CY with LES turbulence blood flow model regarding to the hemodynamic factors within  $R - ICA$  geometry, the hemodynamic factors such as WSS, OSI, SWSSG have been visualized, analyzed and compared for both simulation models.

As seen from the Figure 5.39, the visualizations between shear-thinning model and turbulence flow model have been observed almost the same in terms of WSS and WSS-related parameters which are TAWSS and OSI.

Figure 5.40 indicates SWSSG and TASWSSG visualizations for CY model and CY with LES model within  $R - ICA$  geometry. SWSSG has been visualized at peak systole and TASWSSG has been visualized as time-averaged. As seen from this figure, SWSSG has been observed relatively higher for CY with LES model, particularly after

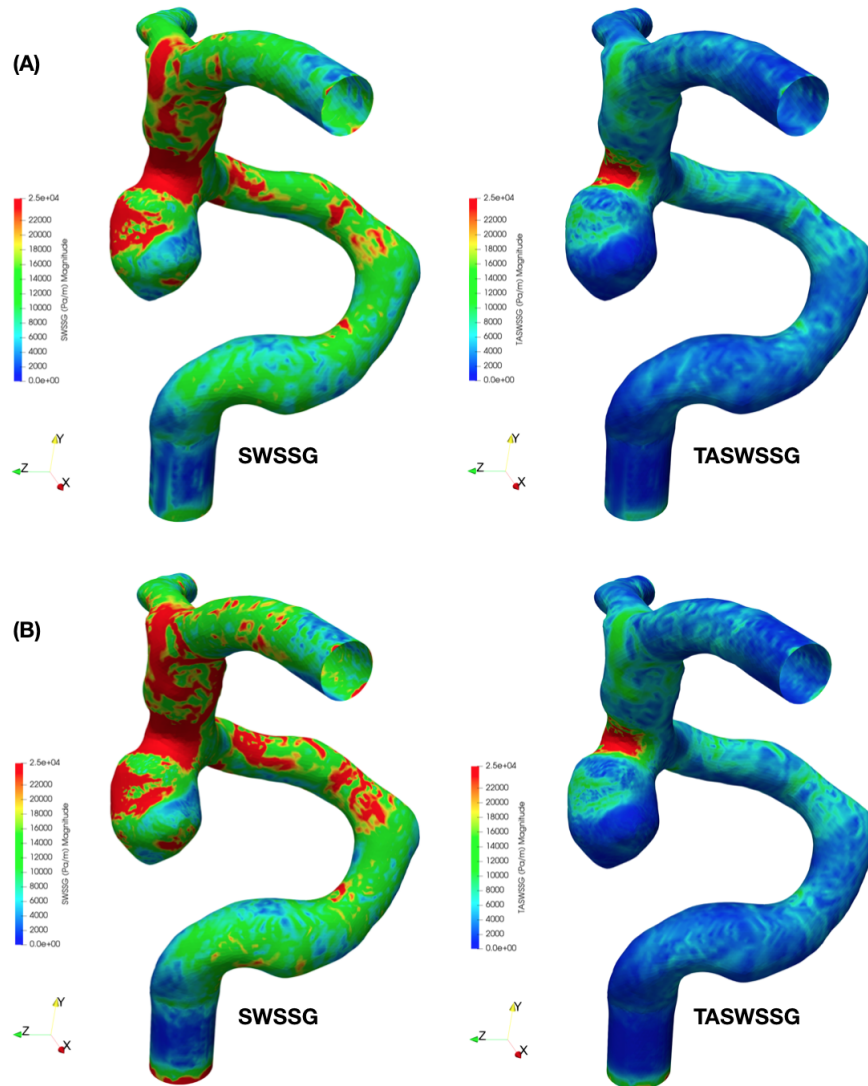
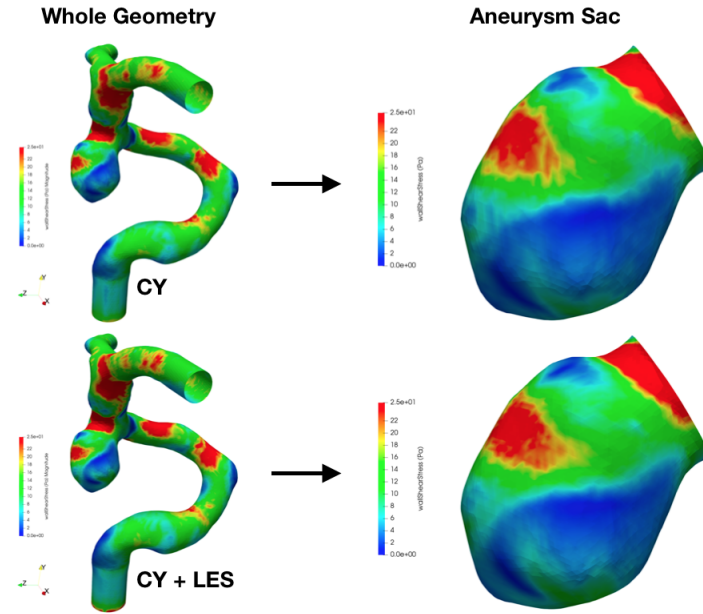


**Figure 5.40** : SWSSG and TASWSSG visualizations within  $R - ICA$  model. SWSSG has been visualized at peak systole. First row, (A) indicates shear-thinning Carreau-Yasuda (CY) model while second row, (B) indicates shear-thinning Carreau-Yasuda (CY) with LES turbulence flow model.



Hemodynamic Parameters	Carreau-Yasuda Model (CY)		CY with LES Turbulence Model (CY + LES)	
	Whole Geometry	Aneurysm Sac	Whole Geometry	Aneurysm Sac
WSS (at peak systole)	11,221 Pa	8,032 Pa	11,262 Pa	8,472 Pa
TAWSS	3,890 Pa	2,233 Pa	3,838 Pa	2,286 Pa
SWSSG (at peak systole)	15277,106 Pa/m	17065,382 Pa/m	16716,869 Pa/m	18181,411 Pa/m
TASWSSG	4645,415 Pa/m	4527,092 Pa/m	4772,124 Pa/m	4555,471 Pa/m
OSI	0,010	0,021	0,011	0,021
OSI (maximum)	0,475	0,435	0,454	0,454
OSI (minimum)	0	0,00002	0	0,00002

**Figure 5.41** : The figure represents the values of hemodynamic factors and WSS visualizations for whole geometry and aneurysm sac area within  $R - ICA$  model. CY indicates Carreau-Yasuda and LES indicates Large Eddy Simulation. WSS has been visualized at peak systole.

aneurysm neck area through bifurcation region. TASWSSG has been observed almost the same for both CY model and CY with LES model within  $R - ICA$  geometry.

The Figure 5.41 represents hemodynamic values and WSS visualizations at peak systole for both CY and CY with LES models in terms of whole geometry and aneurysm sac area of  $R - ICA$  geometry. It could be seen from the visualizations that there is no significant difference between CY model and CY with LES model for  $R - ICA$  geometry.

Considering the values of the hemodynamic factors, mean WSS, mean OSI and maximum OSI values are in the range of the recent study of Detmer et al. [117]. As

seen from the Figure 5.41, although area-averaged WSS values are relatively higher for CY with LES model, this difference could be negligible. In terms of area-averaged WSS values at peak systole for both CY and CY with LES models, there is a significant difference between the whole geometry and aneurysm sac area for  $R - ICA$  geometry. WSS has been observed higher in the whole aneurysm than aneurysm sac area. This could be provide an insight that within parent vessel, WSS values are significantly higher than the aneurysm sac area. As a result,  $R - ICA$  has a reverse situation from  $U - ICA$  in terms of WSS values. TAWSS provides the same outcome just as WSS. Within this study, lower WSS has been observed for ruptured cerebral aneurysm like in the studies of Shojima et al. [54] and Xiang et al. [30].

Area-averaged SWSSG at peak systole and TASWSSG have been observed higher for the CY with LES model within  $R - ICA$  geometry. When comparing the whole geometry and aneurysm sac area of  $R - ICA$ , it could be seen that aneurysm sac area has higher SWSSG values than whole geometry while considering TASWSSG the whole geometry of  $R - ICA$  has higher values than aneurysm sac region. Moreover, within the whole geometry of  $R - ICA$  for both CY and CY with LES models, SWSSG values have been observed higher than the corresponding region and values of  $U - ICA$  geometry (See Figures 5.24 and 5.41). Since low WSS and high SWSSG are associated with disturbed flow according to DePaola et al. [108], it might be interpreted that,  $R - ICA$  has more disturbed flow regions than  $U - ICA$ . In terms of TASWSSG, whole geometry has higher values than aneurysm sac regions within  $R - ICA$  geometry for both CY and CY with LES models.

Mean OSI values of  $R - ICA$  geometry are almost the same for CY and CY with LES models. Considering the whole geometry and aneurysm sac area of  $R - ICA$ , OSI values are approximately 2 times higher within the aneurysm sac area for both CY and CY with LES models. This might make the aneurysm sac area a critical region than parent vessel within  $R - ICA$ . When comparing unruptured cerebral aneurysm  $U - ICA$  and ruptured cerebral aneurysm  $R - ICA$ , mean OSI values are approximately 2 times higher within unruptured cerebral aneurysm  $U - ICA$ . In a majority of studies, higher OSI values are associated with ruptured cerebral aneurysms, however, within this current study, higher OSI values have been observed for unruptured cerebral aneurysm with a rate of 2 times. This result might provide an insight that the unruptured cerebral

aneurysm  $U - ICA$  used within this study might have a high risk of rupture since it has 2 times higher OSI values than ruptured cerebral aneurysm  $R - ICA$ . When considering maximum OSI values, for CY model, maximum OSI value has been observed within the region other than the aneurysm sac area while for CY with LES model, maximum OSI value has been observed within aneurysm sac area (See Figure 5.41).





## 6. DISCUSSIONS AND CONCLUSIONS

It has been demonstrated by the researches in terms of cerebral aneurysms that the assessment based on CFD and hemodynamic factors play a fundamental role to investigate cerebral aneurysm phases which are initiation, growth and rupture, respectively. However, there are still contradictory studies with regards to the rupture risk examinations of the cerebral aneurysms under hemodynamic factors and these factors are not completely understood. For this purpose, within this study, the rupture status of the patient-specific cerebral aneurysms have been examined with regards to hemodynamic factors such as WSS, OSI, TAWSS, SWSSG and TASWSSG by means of CFD.

Within this thesis, the rupture status of one ruptured which belongs to a female patient aged 26 and one unruptured which belongs to a female patient aged 48, patient-specific cerebral aneurysm data have been investigated in terms of hemodynamic factors by using CFD in order to observe the similarities and differences of the rupture status.

Within the both ruptured and unruptured cerebral aneurysm data, the streamlines exhibit smoothly in the inlet area and tend to exhibit transient behavior within the curvature regions. The streamlines behave chaotic and exhibit turbulent nature when the flow arrives in the aneurysm sac area.

The simulation results demonstrated that within the patient specific cerebral aneurysm data, particularly in the aneurysm sac, with the increasing Reynolds numbers especially at the peak systole, the mild turbulence effects have been observed.

Within the current study, the simulation results in terms of WSS values have been observed lower for aneurysm sac area than the parent vessel within the ruptured cerebral aneurysm model, and higher WSS for aneurysm sac area than the parent vessel within the unruptured cerebral aneurysm model, shared the similarity of the significant studies in the literature, e.g. Shojima et al. [54].

The WSS vectors exhibit different directions under the turbulence effects with the turbulence blood flow model, and as a consequence, OSI values increase. High OSI values effect endothelial cells and the vascular wall re-modeling. Within the current study, higher OSI values have been observed for the unruptured cerebral aneurysm  $U - ICA$  than  $R - ICA$  with a rate of two times. In a majority of the studies, higher OSI values are observed within ruptured cerebral aneurysms. Since high OSI values are associated with the ruptured cerebral aneurysms, the unruptured cerebral aneurysm  $U - ICA$  used in this study might have a high risk of rupture. However, in order to examine rupture status within cerebral aneurysms, there is a strong need for further series of analysis by researchers around the world.

According to DePaola et al. [108], low WSS and high SWSSG are associated with disturbed flow. Within this current study, since ruptured cerebral aneurysm  $R - ICA$  has low WSS and high SWSSG values,  $R - ICA$  might have more disturbed flow regions than unruptured cerebral aneurysm  $U - ICA$ .

High SWSSG values have been observed for both unruptured cerebral aneurysm  $U - ICA$  and ruptured cerebral aneurysm  $R - ICA$ . Since high SWSSG is associated with endothelial dysfunction and vascular remodeling, the abnormal values effect these cerebral arteries and aneurysms.

There are a couple of limitations in this study. Within this thesis, only one ruptured and one unruptured cerebral aneurysms have been analyzed in terms of hemodynamic factors by means of CFD. In order to have more reliable interpretations, more ruptured and unruptured patient-specific cerebral aneurysm data could be used for further analyses.

The information with regards to the flow rates and velocities of the patient-specific geometries are not available in the *Aneurisk repository* [99]. Without information of patient-specific measurements, Womersley inlet profile from the literature studies has been implemented for both geometry models. This condition is one of the major limitation for the researchers who study CFD-based cerebral aneurysms.

Large Eddy Simulation (LES) is significantly accurate method comparing to RANS method for turbulence models. Within this study, although there are difference between non-Newtonian Carreau-Yasuda (CY) model and CY with LES turbulence model,

the results are close to each other between these cases. This could arise from the requirements of finer grids for LES models. Due to the lack of the computational resource, within this study, approximately 1,000,000 grids have been used for LES models. As a consequence, no significant difference has been observed between non-Newtonian CY and non-Newtonian CY with LES turbulence model cases. It could be perceivable LES effects significantly when finer grids used.

The blood vessels are living organs. They react to the stimuli comes from the inside or outside of the body. Particularly, under abnormal hemodynamic conditions, vascular walls tend to re-model their structures. In order to investigate blood flow within patient-specific cerebral aneurysms in terms of hemodynamic factors, there is a strong need for fluid-structure interaction. By implementing FSI modeling, both vascular wall structure and blood flow could be observed together and as a consequence, FSI might aid the studies to avoid misleading results. However, the majority of the studies have not been taken into account FSI and modeled the vascular walls as rigid. Also, within this thesis, FSI has not been taken into account due to the lack of vascular wall thickness information. Nevertheless, there is a strong need for FSI in order to have more realistic simulations.



## REFERENCES

- [1] **Rinkel, G.J., Van Gijn, J. et al.** (1998). Prevalence and risk of rupture of intracranial aneurysms, *Stroke*.
- [2] **Brisman, J.L., Song, J.K. and Newell, D.W.** (2006). Cerebral aneurysms, *New England Journal of Medicine*, 355(9), 928–939.
- [3] **Vlak, M.H., Algra, A., Brandenburg, R. and Rinkel, G.J.** (2011). Prevalence of unruptured intracranial aneurysms, with emphasis on sex, age, comorbidity, country, and time period: a systematic review and meta-analysis, *The Lancet Neurology*, 10(7), 626–636.
- [4] **Schievink, W.I.** (1997). Intracranial aneurysms, *New England Journal of Medicine*, 336(1), 28–40.
- [5] **Evju, Ø., Valen-Sendstad, K. and Mardal, K.A.** (2013). A study of wall shear stress in 12 aneurysms with respect to different viscosity models and flow conditions, *Journal of biomechanics*, 46(16), 2802–2808.
- [6] **Nieuwkamp, D.J., Setz, L.E., Algra, A., Linn, F.H., de Rooij, N.K. and Rinkel, G.J.** (2009). Changes in case fatality of aneurysmal subarachnoid haemorrhage over time, according to age, sex, and region: a meta-analysis, *The Lancet Neurology*, 8(7), 635–642.
- [7] **Hop, J.W., Rinkel, G.J., Algra, A. and van Gijn, J.** (1997). Case-fatality rates and functional outcome after subarachnoid hemorrhage: a systematic review, *Stroke*, 28(3), 660–664.
- [8] **Cebral, J.R., Castro, M.A., Burgess, J.E., Pergolizzi, R.S., Sheridan, M.J. and Putman, C.M.** (2005). Characterization of cerebral aneurysms for assessing risk of rupture by using patient-specific computational hemodynamics models, *American Journal of Neuroradiology*, 26(10), 2550–2559.
- [9] **Lemonick, D.M.** (2010). Subarachnoid hemorrhage: state of the art (ery), *Am J Clin Med*, 7, 62–85.
- [10] **Linn, F., Rinkel, G., Algra, A. and Van Gijn, J.** (1996). Incidence of subarachnoid hemorrhage: role of region, year, and rate of computed tomography: a meta-analysis, *Stroke*, 27(4), 625–629.
- [11] **Le Roux, A.A. and Wallace, M.C.** (2010). Outcome and cost of aneurysmal subarachnoid hemorrhage, *Neurosurgery Clinics*, 21(2), 235–246.

- [12] **Kaminogo, M., Yonekura, M. and Shibata, S.** (2003). Incidence and outcome of multiple intracranial aneurysms in a defined population, *Stroke*, *34*(1), 16–21.
- [13] **Wiebers, D.O., Torner, J.C. and Meissner, I.** (1992). Impact of unruptured intracranial aneurysms on public health in the United States., *Stroke*, *23*(10), 1416–1419.
- [14] **Berg, P. and Beuing, O.** (2018). Multiple intracranial aneurysms: a direct hemodynamic comparison between ruptured and unruptured vessel malformations, *International journal of computer assisted radiology and surgery*, *13*(1), 83–93.
- [15] **Van Gijn, J., Kerr, R.S. and Rinkel, G.J.** (2007). Subarachnoid haemorrhage, *The Lancet*, *369*(9558), 306–318.
- [16] **Stehbens, W.E.** (1972). *Pathology of the cerebral blood vessels*, CV Mosby.
- [17] **Lasheras, J.C.** (2007). The biomechanics of arterial aneurysms, *Annu. Rev. Fluid Mech.*, *39*, 293–319.
- [18] **Weir, B.** (2002). Unruptured intracranial aneurysms: a review, *Journal of neurosurgery*, *96*(1), 3–42.
- [19] **Meng, H., Tutino, V., Xiang, J. and Siddiqui, A.** (2013). High WSS or low WSS? Complex interactions of hemodynamics with intracranial aneurysm initiation, growth, and rupture: toward a unifying hypothesis, *American Journal of Neuroradiology*.
- [20] **Sforza, D.M., Putman, C.M. and Cebral, J.R.** (2012). Computational fluid dynamics in brain aneurysms, *International journal for numerical methods in biomedical engineering*, *28*(6-7), 801–808.
- [21] **Munarriz, P.M., Gómez, P.A., Paredes, I., Castaño-Leon, A.M., Cepeda, S. and Lagares, A.** (2016). Basic principles of hemodynamics and cerebral aneurysms, *World neurosurgery*, *88*, 311–319.
- [22] **Ghods, S., Esfahanian, V. and Ghods, S.** (2014). Modeling requirements for computer simulation of cerebral aneurysm, *Journal of Computational Medicine*, *2014*.
- [23] **Isaksen, J., Egge, A., Waterloo, K., Romner, B. and Ingebrigtsen, T.** (2002). Risk factors for aneurysmal subarachnoid haemorrhage: the Tromsø study, *Journal of Neurology, Neurosurgery & Psychiatry*, *73*(2), 185–187.
- [24] **Penn, D.L., Komotar, R.J. and Connolly, E.S.** (2011). Hemodynamic mechanisms underlying cerebral aneurysm pathogenesis, *Journal of Clinical Neuroscience*, *18*(11), 1435–1438.
- [25] **Cebral, J.R. and Raschi, M.** (2013). Suggested connections between risk factors of intracranial aneurysms: a review, *Annals of biomedical engineering*, *41*(7), 1366–1383.

- [26] **Greving, J.P., Wermer, M.J., Brown Jr, R.D., Morita, A., Juvela, S., Yonekura, M., Ishibashi, T., Torner, J.C., Nakayama, T., Rinkel, G.J. et al.** (2014). Development of the PHASES score for prediction of risk of rupture of intracranial aneurysms: a pooled analysis of six prospective cohort studies, *The Lancet Neurology*, 13(1), 59–66.
- [27] **Lee, C. and Qia, Y.** (2014). Prediction of Aneurysm Rupture Based on Computational Fluid Dynamics-A Short Review, *JSM Neurosurg Spine*, 2(6), 1043.
- [28] **Østergaard, J.R. and Høg, E.** (1985). Incidence of multiple intracranial aneurysms: influence of arterial hypertension and gender, *Journal of neurosurgery*, 63(1), 49–55.
- [29] **Cebral, J.R., Mut, F., Weir, J. and Putman, C.M.** (2011). Association of hemodynamic characteristics and cerebral aneurysm rupture, *American Journal of Neuroradiology*, 32(2), 264–270.
- [30] **Xiang, J., Natarajan, S.K., Tremmel, M., Ma, D., Mocco, J., Hopkins, L.N., Siddiqui, A.H., Levy, E.I. and Meng, H.** (2011). Hemodynamic–morphologic discriminants for intracranial aneurysm rupture, *Stroke*, 42(1), 144–152.
- [31] **Qian, Y., Takao, H., Umezu, M. and Murayama, Y.** (2011). Risk analysis of unruptured aneurysms using computational fluid dynamics technology: preliminary results, *American Journal of Neuroradiology*.
- [32] **Hashimoto, T., Meng, H. and Young, W.L.** (2006). Intracranial aneurysms: links among inflammation, hemodynamics and vascular remodeling, *Neurological research*, 28(4), 372–380.
- [33] **Takao, H., Murayama, Y., Otsuka, S., Qian, Y., Mohamed, A., Masuda, S., Yamamoto, M. and Abe, T.** (2012). Hemodynamic differences between unruptured and ruptured intracranial aneurysms during observation, *Stroke*, 43(5), 1436–1439.
- [34] **Xiang, J., Tutino, V., Snyder, K. and Meng, H.** (2013). CFD: computational fluid dynamics or confounding factor dissemination? The role of hemodynamics in intracranial aneurysm rupture risk assessment, *American Journal of Neuroradiology*.
- [35] **Steinman, D.A., Milner, J.S., Norley, C.J., Lownie, S.P. and Holdsworth, D.W.** (2003). Image-based computational simulation of flow dynamics in a giant intracranial aneurysm, *American Journal of Neuroradiology*, 24(4), 559–566.
- [36] **Cebral, J.R., Hernández, M. and Frangi, A.F.** (2003). Computational analysis of blood flow dynamics in cerebral aneurysms from CTA and 3D rotational angiography image data, *International congress on computational bioengineering*, volume 1, pp.191–198.

- [37] **Lu, G., Huang, L., Zhang, X., Wang, S., Hong, Y., Hu, Z. and Geng, D.** (2011). Influence of hemodynamic factors on rupture of intracranial aneurysms: patient-specific 3D mirror aneurysms model computational fluid dynamics simulation, *American Journal of Neuroradiology*, 32(7), 1255–1261.
- [38] **Foutrakis, G.N., Burgreen, G., Yonas, H. and Sclabassi, R.J.** (1996). Construction of 3-D arterial volume meshes from magnetic resonance angiography, *Neurological research*, 18(4), 354–360.
- [39] **Qiu, T., Jin, G., Xing, H. and Lu, H.** (2017). Association between hemodynamics, morphology, and rupture risk of intracranial aneurysms: a computational fluid modeling study, *Neurological Sciences*, 38(6), 1009–1018.
- [40] **Chung, B. and Cebal, J.R.** (2015). CFD for evaluation and treatment planning of aneurysms: review of proposed clinical uses and their challenges, *Annals of biomedical engineering*, 43(1), 122–138.
- [41] **Cebal, J.R. and Meng, H.**, (2012), Counterpoint: realizing the clinical utility of computational fluid dynamics—closing the gap.
- [42] **Ujiie, H., Tachi, H., Hiramatsu, O., Hazel, A.L., Matsumoto, T., Ogasawara, Y., Nakajima, H., Hori, T., Takakura, K. and Kajiya, F.** (1999). Effects of size and shape (aspect ratio) on the hemodynamics of saccular aneurysms: a possible index for surgical treatment of intracranial aneurysms, *Neurosurgery*, 45(1), 119–130.
- [43] **Satoh, T., Onoda, K. and Tsuchimoto, S.** (2003). Visualization of intraaneurysmal flow patterns with transluminal flow images of 3D MR angiograms in conjunction with aneurysmal configurations, *American Journal of Neuroradiology*, 24(7), 1436–1445.
- [44] **Womersley, J.R.** (1955). Method for the calculation of velocity, rate of flow and viscous drag in arteries when the pressure gradient is known, *The Journal of physiology*, 127(3), 553–563.
- [45] **McDonald, D.** (1955). The relation of pulsatile pressure to flow in arteries, *The Journal of physiology*, 127(3), 533–552.
- [46] **Womersley, J.** (1954). Flow in the larger arteries and its relation to the oscillating pressure., *The Journal of physiology*, 124(2), 31.
- [47] **McDonald, D.** (1952). The velocity of blood flow in the rabbit aorta studied with high-speed cinematography, *The Journal of physiology*, 118(3), 328–339.
- [48] **Dintenfass, L.** (1963). Blood rheology in cardio-vascular diseases, *Nature*, 199(4895), 813.
- [49] **Merrill, E.** (1969). Rheology of blood, *Physiological reviews*, 49(4), 863–888.
- [50] **Thurston, G.B.** (1979). Rheological parameters for the viscosity viscoelasticity and thixotropy of blood, *Biorheology*, 16(3), 149–162.



- [51] **Austin, G.** (1971). Biomathematical model of aneurysm of the circle of Willis, I: the Duffing equation and some approximate solutions, *Mathematical Biosciences*, 11(1-2), 163–172.
- [52] **Cronin, J.** (1974). Mathematical model of aneurysm of the circle of Willis: II. A qualitative analysis of the equation of Austin, *Mathematical Biosciences*, 22, 237–275.
- [53] **Perktold, K., Peter, R. and Resch, M.** (1989). Pulsatile non-Newtonian blood flow simulation through a bifurcation with an aneurysm, *Biorheology*, 26(6), 1011–1030.
- [54] **Shojima, M., Oshima, M., Takagi, K., Torii, R., Hayakawa, M., Katada, K., Morita, A. and Kirino, T.** (2004). Magnitude and role of wall shear stress on cerebral aneurysm: computational fluid dynamic study of 20 middle cerebral artery aneurysms, *Stroke*, 35(11), 2500–2505.
- [55] **Malek, A.M., Alper, S.L. and Izumo, S.** (1999). Hemodynamic shear stress and its role in atherosclerosis, *Jama*, 282(21), 2035–2042.
- [56] **Ku, D.** (1985). Pulsatile flow and atherosclerosis in the human carotid bifurcation: positive correlation between plaque location and low and oscillating shear stress, *Arteriosclerosis*, 5, 541–567.
- [57] **Kojima, M., Irie, K., Ikeda, S., Fukuda, T., Arai, F., Hirose, Y. and Negoro, M.** (2012). The hemodynamic study for growth factor evaluation of rupture cerebral aneurysm followed up for five years, *Journal of Biomedical Science and Engineering*, 5(12), 884.
- [58] **Miura, Y., Ishida, F., Umeda, Y., Tanemura, H., Suzuki, H., Matsushima, S., Shimosaka, S. and Taki, W.** (2013). Low wall shear stress is independently associated with the rupture status of middle cerebral artery aneurysms, *Stroke*, 44(2), 519–521.
- [59] **Cebral, J.R., Mut, F., Weir, J. and Putman, C.** (2011). Quantitative characterization of the hemodynamic environment in ruptured and unruptured brain aneurysms, *American Journal of Neuroradiology*, 32(1), 145–151.
- [60] **Castro, M., Putman, C., Radaelli, A., Frangi, A. and Cebral, J.** (2009). Hemodynamics and rupture of terminal cerebral aneurysms, *Academic radiology*, 16(10), 1201–1207.
- [61] **Castro, M.A., Putman, C.M., Sheridan, M. and Cebral, J.** (2009). Hemodynamic patterns of anterior communicating artery aneurysms: a possible association with rupture, *American journal of neuroradiology*, 30(2), 297–302.
- [62] **Chien, A., Tateshima, S., Sayre, J., Castro, M., Cebral, J. and Viñuela, F.** (2009). Patient-specific hemodynamic analysis of small internal carotid artery-ophthalmic artery aneurysms, *Surgical neurology*, 72(5), 444–450.

- [63] **VMTK - the Vascular Modelling Toolkit**, <http://www.vmtk.org/>, date retrieved: 15.08.2018.
- [64] **Castro, M.A., Putman, C.M. and Cebal, J.R.** (2006). Patient-specific computational modeling of cerebral aneurysms with multiple avenues of flow from 3D rotational angiography images, *Academic radiology*, 13(7), 811–821.
- [65] **Valen-Sendstad, K., Piccinelli, M., KrishnankuttyRema, R. and Steinman, D.A.** (2015). Estimation of inlet flow rates for image-based aneurysm CFD models: where and how to begin?, *Annals of biomedical engineering*, 43(6), 1422–1431.
- [66] **Rahman, M., Ogilvy, C.S., Zipfel, G.J., Derdeyn, C.P., Siddiqui, A.H., Bulsara, K.R., Kim, L.J., Riina, H.A., Mocco, J. and Hoh, B.L.** (2011). Unruptured cerebral aneurysms do not shrink when they rupture: multicenter collaborative aneurysm study group, *Neurosurgery*, 68(1), 155–161.
- [67] **Campo-Deaño, L., Oliveira, M.S. and Pinho, F.T.** (2015). A review of computational hemodynamics in middle cerebral aneurysms and rheological models for blood flow, *Applied Mechanics Reviews*, 67(3), 030801.
- [68] **Valencia, A., Zarate, A., Galvez, M. and Badilla, L.** (2006). Non-Newtonian blood flow dynamics in a right internal carotid artery with a saccular aneurysm, *International Journal for Numerical Methods in Fluids*, 50(6), 751–764.
- [69] **Torii, R., Oshima, M., Kobayashi, T., Takagi, K. and Tezduyar, T.E.** (2008). Fluid–structure interaction modeling of a patient-specific cerebral aneurysm: influence of structural modeling, *Computational Mechanics*, 43(1), 151.
- [70] **Doddasomayajula, R., Chung, B.J., Mut, F., Jimenez, C.M., Hamzei-Sichani, F., Putman, C.M. and Cebal, J.R.** (2017). Hemodynamic Characteristics of Ruptured and Unruptured Multiple Aneurysms at Mirror and Ipsilateral Locations, *American Journal of Neuroradiology*.
- [71] **Anand, M. and Rajagopal, K.** (2004). A shear-thinning viscoelastic fluid model for describing the flow of blood, *Int. J. Cardiovasc. Med. Sci*, 4(2), 59–68.
- [72] **Formaggia, L., Quarteroni, A. and Veneziani, A.** (2010). *Cardiovascular Mathematics: Modeling and simulation of the circulatory system*, volume 1, Springer Science & Business Media.
- [73] **Secomb, T.W.** (2016). Hemodynamics, *Comprehensive Physiology*, 6(2), 975.
- [74] **Ku, D.N.** (1997). Blood flow in arteries, *Annual review of fluid mechanics*, 29(1), 399–434.
- [75] **Iaizzo, P.A.** (2009). *Handbook of cardiac anatomy, physiology, and devices*, Springer Science & Business Media.

- [76] **Fahraeus, R. and Lindqvist, T.** (1931). The viscosity of the blood in narrow capillary tubes, *American Journal of Physiology-Legacy Content*, 96(3), 562–568.
- [77] **Toksvang, L.N. and Berg, R.M.** (2013). Using a classic paper by Robin Fåhraeus and Torsten Lindqvist to teach basic hemorheology, *Advances in physiology education*, 37(2), 129–133.
- [78] **Pries, A.R. and Secomb, T.W.**, (2008). Blood flow in microvascular networks, *Microcirculation*, Elsevier, pp.3–36.
- [79] **Chien, S., Usami, S., Taylor, H.M., Lundberg, J.L. and Gregersen, M.I.** (1966). Effects of hematocrit and plasma proteins on human blood rheology at low shear rates., *Journal of Applied Physiology*, 21(1), 81–87.
- [80] **Thurston, G.B.** (1972). Viscoelasticity of human blood, *Biophysical journal*, 12(9), 1205–1217.
- [81] **Blood Vessels**, <https://healthjade.com/blood-vessels/>, date retrieved: 11.10.2018.
- [82] **Foutrakis, G.N., Yonas, H. and Sclabassi, R.J.** (1999). Saccular aneurysm formation in curved and bifurcating arteries, *American Journal of Neuroradiology*, 20(7), 1309–1317.
- [83] **Nixon, A.M., Gunel, M. and Sumpio, B.E.** (2010). The critical role of hemodynamics in the development of cerebral vascular disease: a review, *Journal of neurosurgery*, 112(6), 1240–1253.
- [84] **Chhabra, R.P. and Richardson, J.F.** (1999). *Non-Newtonian Flow: Fundamentals and Engineering Applications*, Elsevier.
- [85] **Bernabeu, M.O., Nash, R.W., Groen, D., Carver, H.B., Hetherington, J., Krüger, T. and Coveney, P.V.** (2013). Impact of blood rheology on wall shear stress in a model of the middle cerebral artery, *Interface Focus*, 3(2), 20120094.
- [86] **Cho, Y.I. and Kensey, K.R.** (1991). Effects of the non-Newtonian viscosity of blood on flows in a diseased arterial vessel. Part 1: Steady flows, *Biorheology*, 28(3-4), 241–262.
- [87] **Gijsen, F.J., van de Vosse, F.N. and Janssen, J.** (1999). The influence of the non-Newtonian properties of blood on the flow in large arteries: steady flow in a carotid bifurcation model, *Journal of biomechanics*, 32(6), 601–608.
- [88] **Valencia, A., Morales, H., Rivera, R., Bravo, E. and Galvez, M.** (2008). Blood flow dynamics in patient-specific cerebral aneurysm models: the relationship between wall shear stress and aneurysm area index, *Medical engineering & physics*, 30(3), 329–340.
- [89] **Molla, M.M. and Paul, M.** (2012). LES of non-Newtonian physiological blood flow in a model of arterial stenosis, *Medical engineering & physics*, 34(8), 1079–1087.

- [90] **Chen, J., Lu, X.Y. and Wang, W.** (2006). Non-Newtonian effects of blood flow on hemodynamics in distal vascular graft anastomoses, *Journal of Biomechanics*, 39(11), 1983–1995.
- [91] **Bernsdorf, J. and Wang, D.** (2009). Non-Newtonian blood flow simulation in cerebral aneurysms, *Computers & Mathematics with Applications*, 58(5), 1024–1029.
- [92] **Box, F.M., van der Geest, R.J., Rutten, M.C. and Reiber, J.H.** (2005). The influence of flow, vessel diameter, and non-newtonian blood viscosity on the wall shear stress in a carotid bifurcation model for unsteady flow, *Investigative radiology*, 40(5), 277–294.
- [93] **Reynolds, O.** (1883). XXIX. An experimental investigation of the circumstances which determine whether the motion of water shall be direct or sinuous, and of the law of resistance in parallel channels, *Philosophical Transactions of the Royal Society of London*, 174, 935–982.
- [94] **Young, D.F., Munson, B.R., Okiishi, T.H. and Huebsch, W.W.** (2010). *A brief introduction to fluid mechanics*, John Wiley & Sons.
- [95] **Roach, M.R., Scott, S. and Ferguson, G.G.** (1972). The hemodynamic importance of the geometry of bifurcations in the circle of Willis (glass model studies), *Stroke*, 3(3), 255–267.
- [96] **OpenFOAM - Open-source Field Operation And Manipulation**, <https://openfoam.org/>, date retrieved: 24.09.2018.
- [97] **Leonard, A.**, (1975). Energy cascade in large-eddy simulations of turbulent fluid flows, *Advances in geophysics*, volume 18, Elsevier, pp.237–248.
- [98] **Kajishima, T. and Taira, K.** (2016). *Computational fluid dynamics: incompressible turbulent flows*, Springer.
- [99] **Aneurisk-Team**, (2012), AneuriskWeb project website, <http://ecm2.mathcs.emory.edu/aneuriskweb>, Web Site, <http://ecm2.mathcs.emory.edu/aneuriskweb>.
- [100] **Netgen/NGSolve**, <https://ngsolve.org>, date retrieved: 26.09.2018.
- [101] **ParaView**, <https://www.paraview.org>, date retrieved: 30.09.2018.
- [102] **Wang, Z., Kolega, J., Hoi, Y., Gao, L., Swartz, D.D., Levy, E.I., Mocco, J. and Meng, H.** (2009). Molecular alterations associated with aneurysmal remodeling are localized in the high hemodynamic stress region of a created carotid bifurcation, *Neurosurgery*, 65(1), 169–178.
- [103] **Chen, Z., Yu, H., Shi, Y., Zhu, M., Wang, Y., Hu, X., Zhang, Y., Chang, Y., Xu, M. and Gao, W.** (2017). Vascular remodelling relates to an elevated oscillatory shear index and relative residence time in spontaneously hypertensive rats, *Scientific Reports*, 7(1), 2007.

- [104] **Knight, J., Olgac, U., Saur, S.C., Poulikakos, D., Marshall Jr, W., Cattin, P.C., Alkadhi, H. and Kurtcuoglu, V.** (2010). Choosing the optimal wall shear parameter for the prediction of plaque location—a patient-specific computational study in human right coronary arteries, *Atherosclerosis*, 211(2), 445–450.
- [105] **Shimogonya, Y., Ishikawa, T., Imai, Y., Matsuki, N. and Yamaguchi, T.** (2009). Can temporal fluctuation in spatial wall shear stress gradient initiate a cerebral aneurysm? A proposed novel hemodynamic index, the gradient oscillatory number (GON), *Journal of biomechanics*, 42(4), 550–554.
- [106] **Watton, P.N., Raberger, N.B., Holzapfel, G.A. and Ventikos, Y.** (2009). Coupling the hemodynamic environment to the evolution of cerebral aneurysms: computational framework and numerical examples, *Journal of biomechanical engineering*, 131(10), 101003.
- [107] **Tanoue, T., Tateshima, S., Villablanca, J., Viñuela, F. and Tanishita, K.** (2011). Wall shear stress distribution inside growing cerebral aneurysm, *American Journal of Neuroradiology*, 32(9), 1732–1737.
- [108] **DePaola, N., Gimbrone Jr, M.A., Davies, P.F. and Dewey Jr, C.F.** (1992). Vascular endothelium responds to fluid shear stress gradients., *Arteriosclerosis and thrombosis: a journal of vascular biology*, 12(11), 1254–1257.
- [109] **Roache, P.J.** (1994). Perspective: a method for uniform reporting of grid refinement studies, *Journal of Fluids Engineering*, 116(3), 405–413.
- [110] **Celik, I.B., Ghia, U., Roache, P.J. et al.** (2008). Procedure for estimation and reporting of uncertainty due to discretization in {CFD} applications, *Journal of fluids {Engineering-Transactions} of the {ASME}*, 130(7).
- [111] **Roache, P.J.** (1997). Quantification of uncertainty in computational fluid dynamics, *Annual review of fluid Mechanics*, 29(1), 123–160.
- [112] **Hodis, S., Uthamaraj, S., Smith, A.L., Dennis, K.D., Kallmes, D.F. and Dragomir-Daescu, D.** (2012). Grid convergence errors in hemodynamic solution of patient-specific cerebral aneurysms, *Journal of biomechanics*, 45(16), 2907–2913.
- [113] **Piskin, S., Aribas, E. and Celebi, M.S.** (2010). A 3D human carotid artery simulation using realistic geometry and experimental input data, *5th European conference on computational fluid dynamics, ECCOMAS CFD*.
- [114] **CFD Direct From the Cloud: Run on AWS EC2**, [https://cfdirect/cloud/aws/](https://cfdirect.cloud/aws/), date retrieved: 29.09.2018.
- [115] **Amazon Elastic Compute Cloud (Amazon EC2)**, <https://aws.amazon.com/ec2/>, date retrieved: 29.09.2018.
- [116] **UHeM - National Center for High Performance Computing (TURKEY)**, <http://www.uhem.itu.edu.tr>, date retrieved: 20.10.2018.

- [117] **Detmer, F.J., Chung, B.J., Mut, F., Slawski, M., Hamzei-Sichani, F., Putman, C., Jiménez, C. and Cebal, J.R.** (2018). Development and internal validation of an aneurysm rupture probability model based on patient characteristics and aneurysm location, morphology, and hemodynamics, *International journal of computer assisted radiology and surgery*, 13(11), 1767–1779.



## CURRICULUM VITAE



**Name Surname:** G. Merve Narinses

**Place and Date of Birth:** Istanbul TURKEY, 1987

**Address:** Heverlee, BELGIUM

**E-Mail:** narinses@itu.edu.tr

### EDUCATION:

- **B.Sc.:** 2012, Akdeniz University, Faculty of Science, Biology
- **M.Sc.:** 2018, Istanbul Technical University, Informatics Institute, Computational Science And Engineering
- **International Scholar:** 2017, Katholieke Universiteit Leuven, Faculty of Science (Leuven), Neuroscience

### PROFESSIONAL EXPERIENCE AND REWARDS:

- Junior Researcher at imec (BELGIUM)
- International Scholar at NERF - Empowered by imec, KU Leuven and VIB (BELGIUM)
- Scholarship from Katholieke Universiteit Leuven (BELGIUM)